

2



**AD-A273 925**



NRL/MR/7533--93-7213

# Development and Testing of the Coupled Ocean/Atmosphere Mesoscale Prediction System (COAMPS)

RICHARD M. HODUR

*Prediction Systems Branch  
Marine Meteorology Division*

**S** DTIC  
ELECTE  
DEC 20 1993  
**A**

November 1993

**93-30660**



**93 12 17054**

Approved for public release; distribution unlimited.

# REPORT DOCUMENTATION PAGE

Form Approved  
OMB No. 0704-0188

Public reporting burden for this collection of information is estimated to average 1 hour per response, including the time for reviewing instructions, searching existing data sources, gathering and maintaining the data needed, and completing and reviewing the collection of information. Send comments regarding this burden or any other aspect of this collection of information, including suggestions for reducing this burden, to Washington Headquarters Services, Directorate for Information Operations and Reports, 1215 Jefferson Davis Highway, Suite 1204, Arlington, VA 22202-4302, and to the Office of Management and Budget, Paperwork Reduction Project (0704-0188), Washington, DC 20503.

1. Agency Use Only (Leave blank).	2. Report Date. November 1993	3. Report Type and Dates Covered. Final	
4. Title and Subtitle. Development and Testing of the Coupled Ocean/Atmosphere Mesoscale Prediction System (COAMPS)		5. Funding Numbers. PE 0602435N PN R035E71 AN DN153155	
6. Author(s). Richard M. Hodur		8. Performing Organization Report Number. NRL/MR/7533--93-7213	
7. Performing Organization Name(s) and Address(es). Naval Research Laboratory Marine Meteorology Division Monterey, CA 93943-5502			
9. Sponsoring/Monitoring Agency Name(s) and Address(es). Office of Naval Research Arlington, VA 22217-5660		10. Sponsoring/Monitoring Agency Report Number.	
11. Supplementary Notes.			
12a. Distribution/Availability Statement.  Approved for public release; distribution unlimited.		12b. Distribution Code.	
13. Abstract (Maximum 200 words). A three-dimensional coupled ocean/atmosphere mesoscale prediction system (COAMPS) has been developed, consisting of a nonhydrostatic atmospheric model and a hydrostatic ocean model. The models can be integrated simultaneously so that the surface fluxes of heat, momentum, and moisture are exchanged across the air-water interface every time step. Optionally, either the atmospheric model or the ocean model can be used as a stand-alone system. Two idealized simulations of a hurricane are performed. In the first simulation, only the atmospheric model is used, assuming a fixed sea surface temperature. A realistic hurricane structure with spiral bands develops. Evidence is found of concentric eye walls interacting to modify the intensification of the hurricane. In the second simulation, the ocean model is run simultaneously with the atmospheric model. After 84 hours, the sea surface temperature decreases more than 80C within the radius of maximum winds. While this has a large impact on the intensity of the system (i.e., the strength of the maximum winds), there is little change in the overall structure of the system as measured by the tangential velocities outside the radius of maximum winds.			
14. Subject Terms. COAMPS                      Atmospheric model Mesoscale prediction      Ocean model		15. Number of Pages. 84	
		16. Price Code.	
17. Security Classification of Report. UNCLASSIFIED	18. Security Classification of This Page. UNCLASSIFIED	19. Security Classification of Abstract. UNCLASSIFIED	20. Limitation of Abstract. Same as report

## CONTENTS

1. Introduction .....	1
2. Atmospheric Model .....	4
3. Ocean Model .....	15
4. Model Tests and Results .....	22
5. Conclusion .....	69
Acknowledgments .....	72
References .....	73

Accession For	
NTIS GRA&I	<input checked="" type="checkbox"/>
DTIC TAB	<input type="checkbox"/>
Unannounced	<input type="checkbox"/>
Justification	
By .....	
Distribution /	
Availability Codes	
Dist	Available and/or Special
A-1	

**DTIC QUALITY INSPECTED 1**

# DEVELOPMENT AND TESTING OF THE COUPLED OCEAN/ATMOSPHERE MESOSCALE PREDICTION SYSTEM (COAMPS)

## 1. Introduction

U. S. Navy operations require a very detailed specification of the environment. The most recent example of this was exhibited in Operation Desert Storm. The weapons that are used in operations such as this are affected by moisture, temperature, aerosols, etc. To determine these parameters, the Navy currently relies on the Navy Operational Global Atmospheric Prediction System (NOGAPS) (Hogan and Rosmond, 1991) and the Navy Operational Regional Atmospheric Prediction System (NORAPS) (Hodur, 1987). Both NOGAPS and NORAPS are hydrostatic atmospheric models using horizontal resolutions in the range of 40-150 km. For operations such as Desert Storm, the Navy needs higher temporal and spatial resolution than either NOGAPS or NORAPS currently provides. Therefore, the Navy must look to develop models capable of predicting scales of motion at and below the meso- $\beta$  scale, which will require grid spacings of 20 km or less.

The prediction of atmospheric motions of meso- $\beta$  and smaller scale implies that the hydrostatic approximation may be invalid at times, particularly for convection and smaller-scale topographic features where the vertical wavelength is a significant fraction of the horizontal wavelength. The concept of using the nonhydrostatic form of the equations as a prediction tool started with the work of Ogura and Charney (1962) and Ogura and Phillips (1962). However, it wasn't until the 1970's that numerical models based on the nonhydrostatic equations were developed. Several of these models were used to study convective processes (Miller and Pearce, 1974; Schlesinger, 1975; Clark, 1977; Klemp and Wilhelmson, 1978; Clark, 1979; Tripoli and Cotton, 1982) while others studied mountain flows (Durrant and Klemp, 1983; Schumann, 1987; Xue and Thorpe, 1991). The British Meteorological Office developed a nonhydrostatic model for operational use (Tapp and White, 1976; Carpenter, 1979) and Tripoli (1992a) has recently developed a nonhydrostatic

model to study scale interaction.

One of the problems in dealing with the nonhydrostatic equations is that they allow for rapidly propagating sound waves, thereby limiting the time step of the model. The anelastic approximation (Ogura and Phillips, 1962) eliminates the sound waves, but necessitates the solution of a three-dimensional elliptic equation every time step for pressure or geopotential, which can be computationally expensive (Tapp and White, 1976; Miller, 1974; Clark, 1977; Xue and Thorpe, 1991). Klemp and Wilhelmson (1978) used the fully-compressible equations with a time-splitting method, which allowed for large time-steps to be taken for the slow modes and shorter time steps for the faster sound modes. This time-splitting technique, coupled with semi-implicit differencing in the vertical, made the computational expense of integrating the compressible form of the nonhydrostatic equations competitive with the anelastic form. The quasi-compressible approximation (Chorin, 1967), which artificially slows down the sound waves, is an alternative method to allow for larger time steps in the fully-compressible equations (Droegemeier and Wilhelmson, 1987).

The recent advances made in mesoscale modeling coupled with the products needed by the Navy suggest a redefinition of "regional" modeling. It is now apparent that global models, currently capable of resolutions in the 50-100 km range, can handle synoptic-scale systems quite well (Hogan and Rosmond, 1991). This is the range in which regional models, such as NORAPS, have served over the past decade. However, due to the history of armed conflicts in the vicinity of coastal areas and the pace of computer technology, we will hereafter refer to "regional", or "limited-area" modeling, as the development of a data assimilation system for the analysis and forecast of meso- $\beta$  and meso- $\gamma$  scales of motion in coastal areas. This coastal data assimilation system should allow for nonhydrostatic processes,

detailed topographic flows, and explicit treatment of precipitation processes, and be fully coupled with the lower boundary, with detailed description and/or coupled forecasts of surface parameters such as the sea-surface temperature (SST), ground wetness and ground temperature. This system must take into account new data sources such as Doppler and profiler winds as well as newly emerging computer technology such as parallel computer architecture.

To serve the Navy's future mesoscale modeling needs, the Naval Research Laboratory (NRL) is developing the Coupled Ocean/Atmosphere Mesoscale Prediction System (COAMPS). COAMPS features a nonhydrostatic atmospheric model coupled to a hydrostatic ocean model. Initially, COAMPS is intended to serve as a community research model for studying various mesoscale phenomena such as arctic leads, convection, lake-effect snowstorms and tropical cyclones. Some of these phenomena, such as tropical cyclones, exchange a great deal of energy with the ocean. This process is represented within COAMPS. It is expected that the study of a variety of mesoscale phenomena will add to the utility of COAMPS as it transitions to operational use over the next few years. In fact, many of the features of the COAMPS forecast models will eventually transition into the NORAPS forecast model in our coastal data assimilation system.

The purpose of this paper is to describe the current structure of COAMPS and to show results from an experiment that demonstrates the effect of ocean changes on the structure of a tropical cyclone. In section 2 we describe the nonhydrostatic atmospheric model. In section 3 we describe the hydrostatic ocean model. The tropical cyclone experiments with COAMPS are described in section 4. A summary and conclusions are given in section 5.

## 2. Atmospheric Model

### a. Dynamics

The adiabatic equations are developed in a manner similar to that used by Klemp and Wilhelmson (1978). Using the equation of state,

$$p = \rho R_d T_v \quad (1)$$

the definition of the virtual temperature,

$$T_v = T(1.0 + 0.608q_v) \quad (2)$$

and the Exner function,

$$\pi = \left( \frac{p}{p_{00}} \right)^{\frac{R_d}{C_p}} \quad (3)$$

the primitive equations can be rewritten as:

$$\frac{\partial u}{\partial t} + C_p \bar{\theta}_v \frac{\partial \pi'}{\partial x} + K_D \frac{\partial D_3}{\partial x} = -u \frac{\partial u}{\partial x} - v \frac{\partial u}{\partial y} - w \frac{\partial u}{\partial z} + fv + D_u + K_B \nabla^4 u \quad (4)$$

$$\frac{\partial v}{\partial t} + C_p \bar{\theta}_v \frac{\partial \pi'}{\partial y} + K_D \frac{\partial D_3}{\partial y} = -u \frac{\partial v}{\partial x} - v \frac{\partial v}{\partial y} - w \frac{\partial v}{\partial z} - fu + D_v + K_B \nabla^4 v \quad (5)$$

$$\begin{aligned} \frac{\partial w}{\partial t} + C_p \bar{\theta}_v \frac{\partial \pi'}{\partial z} + K_D \frac{\partial D_3}{\partial z} = & -u \frac{\partial w}{\partial x} - v \frac{\partial w}{\partial y} - w \frac{\partial w}{\partial z} + D_w + K_B \nabla^4 w \\ & + g \left[ \frac{\theta'}{\bar{\theta}} + 0.608(q_v - \bar{q}_v) - q_c - q_r - q_i - q_s \right] \quad (6) \end{aligned}$$

$$\frac{\partial \pi'}{\partial t} + \frac{\bar{c}^2}{C_p \bar{\rho} \bar{\theta}_v^2} [D_3] = 0 \quad (7)$$

$$\frac{\partial \theta}{\partial t} = -u \frac{\partial \theta}{\partial x} - v \frac{\partial \theta}{\partial y} - w \frac{\partial \theta}{\partial z} + D_\theta + K_B \nabla^4 \theta \quad (8)$$

where  $D_3$  is the three-dimensional divergence,

$$D_3 = \frac{\partial(\bar{\rho} \bar{\theta}_v u)}{\partial x} + \frac{\partial(\bar{\rho} \bar{\theta}_v v)}{\partial y} + \frac{\partial(\bar{\rho} \bar{\theta}_v w)}{\partial z} \quad (9)$$

$p$  is the pressure,  $\rho$  the density,  $R_d$  the gas constant for dry air,  $T$  is the temperature,  $q_v$ ,  $q_c$ ,  $q_r$ ,  $q_i$  and  $q_s$  are the mixing ratios of water vapor, cloud droplets, raindrops, ice crystals and snowflakes, respectively,  $p_{00}$  is a constant reference pressure,  $C_p$  is the specific heat at constant pressure for the atmosphere,  $u$ ,  $v$  and  $w$  are the wind components in the x-, y- and z-directions, respectively,  $f$  is the Coriolis parameter and  $g$  is the acceleration due to gravity. The terms  $D_u$ ,  $D_v$ ,  $D_w$  and  $D_\theta$  represent subgrid scale mixing. The terms involving  $K_D$  represent divergence damping that control the amplification of sound waves (Skamarock and Klemp 1992) where  $K_D$  is the diffusion coefficient.  $K_B$  is a coefficient for fourth-order diffusion used to control numerical noise when the equations are solved on a discrete grid. The speed of sound for the mean state,  $\bar{c}$ , is defined as:

$$\bar{c} = \left( \frac{C_p R_d \bar{\pi} \bar{\theta}_v}{C_v} \right)^{\frac{1}{2}} \quad (10)$$

where  $C_v$  is the specific heat at constant volume for the atmosphere. In eqs (4) - (8), the variables  $\pi$  and  $\theta$  have been decomposed as:

$$(\ ) = (\bar{\ }) + (\ )' \quad (11)$$

where the overbar denotes the initial mean state, which is a function of  $z$  only, and the prime denotes deviations from this mean. The mean state follows the hydrostatic relationship,

$$\frac{\partial \bar{\pi}}{\partial z} = -\frac{g}{C_p \bar{\theta}_v}. \quad (12)$$

The equations are solved on a staggered, scheme C grid (Arakawa and Lamb, 1974). On this grid, the  $u$ -components are one-half grid interval between the mass points in the x-direction and the  $v$ -components are one-half grid interval between the mass points in the y-direction. The  $w$ -component is staggered in a similar manner with respect to the mass variables. All derivatives are computed to second-order

accuracy except the horizontal diffusion, which uses approximations of fourth-order accuracy to damp only the shortest wavelengths. High-frequency time oscillations are controlled using the Robert (1966) time filter using a smoothing parameter of 0.2.

*b. Subgrid Scale Mixing*

COAMPS has been designed to use horizontal grid spacing ranging from an upper limit of about 20 km for meso- $\beta$  scale applications down to the order of 1 m for Large Eddy Simulation (LES) applications. At the higher resolutions, in which the horizontal and vertical grid spacings are typically the same, the subgrid scale mixing terms must represent the 3-dimensional turbulence and be based on the volume-averaging method (Wyngaard 1982). At the coarser resolutions, in which the horizontal grid spacing can be an order of magnitude or more greater than the vertical grid spacing, the horizontal and vertical subgrid scale mixing terms must be treated separately and be based on the ensemble-averaging method. In the following sub-sections we describe first, the volume-averaging method for LES applications; second, the ensemble-averaged parameterization for meso- $\beta$  applications and; third, the background diffusion used to suppress numerically generated noise.

1) LES APPLICATIONS

The subgrid scale turbulence terms,  $D_\alpha$ , for any variable  $\alpha$ , are represented as:

$$D_\alpha = \frac{\partial(\overline{\alpha'u'})}{\partial x} + \frac{\partial(\overline{\alpha'v'})}{\partial y} + \frac{\partial(\overline{\alpha'w'})}{\partial z} \quad (13)$$

The fluxes  $\overline{\alpha'u'}$ ,  $\overline{\alpha'v'}$  and  $\overline{\alpha'w'}$  must be determined to close the system of equations. The fluxes are written in terms of a coefficient of eddy viscosity,  $K$ , and the known

grid point variables. The momentum fluxes become,

$$\overline{u'_i u'_j} = -K_m \left( \frac{\partial u_i}{\partial x_j} + \frac{\partial u_j}{\partial x_i} \right) + \frac{2}{3} \delta_{ij} e \quad (14)$$

and for the remaining scalar variables,

$$\overline{u'_i \alpha'} = -K_h \frac{\partial \alpha}{\partial x_i} \quad (15)$$

where  $K_m$  and  $K_h$  are the eddy mixing coefficients for momentum and heat, respectively, and are defined as:

$$K_m = S_m l e^{1/2} \quad (16)$$

and

$$K_h = S_h l e^{1/2} \quad (17)$$

$e$  is the subgrid scale turbulent kinetic energy (tke) following Deardorff (1980) and  $\alpha$  represents  $\theta, q_v, q_c, q_r, q_i, q_s$ . The coefficient  $S_m$  is set to a constant value of 0.1, and

$$S_h = \left( 1 + \frac{2l}{\Delta s} \right) S_m \quad (18)$$

and,

$$\Delta s = (\Delta x \Delta y \Delta z)^{1/3} \quad (19)$$

where  $\Delta x$ ,  $\Delta y$  and  $\Delta z$  are the grid spacings in the x-, y- and z-directions. The mixing length,  $l$ , is computed as,

$$l = 0.76 e^{1/2} \left( \frac{g}{\theta} \frac{\partial \theta}{\partial z} \right)^{-1/2} \quad (20)$$

for unsaturated air when  $\frac{\partial \theta}{\partial z} > 0$ ,

$$l = 0.76 e^{1/2} \left( \frac{g}{\theta} \frac{\partial \theta_e}{\partial z} \right)^{-1/2} \quad (21)$$

for saturated air when  $\frac{\partial \theta_s}{\partial z} > 0$  and

$$l = \Delta s \quad (22)$$

otherwise.

The turbulent kinetic energy,  $e$ , is predicted in a manner similar to that described by Deardorff (1980). Here,

$$\frac{\partial e}{\partial t} = -u \frac{\partial e}{\partial x} - v \frac{\partial e}{\partial y} - w \frac{\partial e}{\partial z} + BP + SP + D_e + K_B \nabla^4 e - \epsilon \quad (23)$$

where  $BP$  is the buoyancy production term,  $SP$  is the shear production term,  $\epsilon$  is the dissipation rate and all the other variables are as described previously. The buoyancy production is defined as:

$$BP = -\frac{gK_h}{\theta} \frac{\partial \theta_v}{\partial z} \quad (24)$$

for nonsaturated points and

$$BP = -\frac{gK_h}{\theta} \frac{\partial \theta_e}{\partial z} \quad (25)$$

for saturated points. The shear production is defined as:

$$\begin{aligned} SP = & K_m \left[ \left( \frac{\partial u}{\partial x} \right)^2 + \left( \frac{\partial v}{\partial y} \right)^2 + \left( \frac{\partial w}{\partial z} \right)^2 \right. \\ & + \left( \frac{\partial v}{\partial x} + \frac{\partial u}{\partial y} \right)^2 + \left( \frac{\partial w}{\partial x} + \frac{\partial u}{\partial z} \right)^2 + \left. \left( \frac{\partial w}{\partial y} + \frac{\partial v}{\partial z} \right)^2 \right] \\ & - \frac{2}{3} e \left( \frac{\partial u}{\partial x} + \frac{\partial v}{\partial y} + \frac{\partial w}{\partial z} \right) \end{aligned} \quad (26)$$

and the dissipation rate is defined as:

$$\epsilon = \frac{C_\epsilon e^{\frac{3}{2}}}{l} \quad (27)$$

where

$$C_\epsilon = 0.19 + \frac{0.51l}{\Delta s} \quad (28)$$

## 2) MESO- $\beta$ APPLICATIONS

For meso- $\beta$  applications, we apply eddy viscosity closure separately for the horizontal and vertical mixing terms. This means that we have four separate eddy mixing coefficients, one for mixing scalar variables in the horizontal,  $K_{hH}$ , one for mixing momentum in the horizontal,  $K_{mH}$ , one for mixing scalar variables in the vertical,  $K_{hV}$  and one for mixing momentum in the vertical,  $K_{mV}$ . The eddy mixing coefficients in the vertical are as defined in the previous section:

$$K_{hV} = S_h l_V e^{1/2} \quad (29)$$

and

$$K_{mV} = S_m l_V e^{1/2} \quad (30)$$

with the exception that  $l_V$ , represents the *vertical* mixing length, defined as:

$$l_V = \frac{kz}{1 + \frac{kz}{l_0}} \quad (31)$$

where  $k$  is the von Karman constant (0.4),  $z$  is the height above the surface and  $l_0$  is a specified constant. The prediction of  $e$  is performed using (23) except that the shear production term ( $SP$ ) is simplified as:

$$SP = K_{mV} \left[ \left( \frac{\partial u}{\partial z} \right)^2 + \left( \frac{\partial v}{\partial z} \right)^2 + \left( \frac{\partial w}{\partial z} \right)^2 \right] \quad (32)$$

In the horizontal, the eddy mixing coefficients are based on the deformation of the horizontal velocity field (Smagorinsky 1963),

$$K_{mH} = \frac{0.14 l_H^2}{\sqrt{2}} \left[ \left( \frac{\partial u}{\partial y} + \frac{\partial v}{\partial x} \right)^2 + \left( \frac{\partial u}{\partial x} - \frac{\partial v}{\partial y} \right)^2 \right]^{1/2} \quad (33)$$

and

$$K_{hH} = 3K_{mH} \quad (34)$$

where the horizontal mixing length,  $l_H$  is defined as:

$$l_H = (\Delta x \Delta y)^{1/2} \quad (35)$$

### 3) BACKGROUND DIFFUSION

The solution of continuous equations on a discrete grid inevitably leads to the generation of spurious gravity waves due to truncation errors, boundary reflections, etc. To prevent these small sources of energy from growing and contaminating the forecasts, we have included a background fourth-order diffusion to all prognostic variables except for  $\pi'$ . The form of this operator, for any variable  $\alpha$ , is  $K_B \nabla^2(\nabla^2 \alpha)$ , which allows us to compute  $\nabla^2 \alpha$  first, use this on the grid rows/columns immediately adjacent to the boundaries and then compute  $\nabla^2(\nabla^2 \alpha)$  for the remaining interior points. The coefficient is chosen such that the ratio  $(K_B \Delta t_a)/(\Delta x \Delta y) = 0.025$  for the second-order points and  $(K_B \Delta t_a)/(\Delta x^2 \Delta y^2) = -0.0025$  for the fourth-order points, where  $\Delta t_a$  is the time step of the model. These values for the coefficient have been empirically determined so that they produce a light smoothing of the shortest wavelengths during the forecasts with minimal effect on the larger wavelengths.

#### *c. Moist Physics*

Due to the grid-spacing used in COAMPS ( $\leq 20$  km), we use explicit treatment of the moist physics, rather than parameterizing the effects of convection. The microphysical processes leading to conversion between water vapor, cloud droplets, etc. are as described in Rutledge and Hobbs (1983) and therefore, will not be presented here. The inclusion of this moist physics package necessitates equations for water vapor ( $q_v$ ), cloud droplets ( $q_c$ ), raindrops ( $q_r$ ), ice crystals ( $q_i$ ) and snowflakes ( $q_s$ ) in addition to adding a latent heating term ( $Q_\theta$ ) to the thermodynamic equa-

tion. The thermodynamic and moisture equations become:

$$\frac{\partial \theta}{\partial t} = -u \frac{\partial \theta}{\partial x} - v \frac{\partial \theta}{\partial y} - w \frac{\partial \theta}{\partial z} + \frac{Q_\theta}{\bar{\rho}} + D_\theta + K_B \nabla^4 \theta \quad (36)$$

$$\frac{\partial q_v}{\partial t} = -u \frac{\partial q_v}{\partial x} - v \frac{\partial q_v}{\partial y} - w \frac{\partial q_v}{\partial z} + \frac{S_v}{\bar{\rho}} + D_{q_v} + K_B \nabla^4 q_v \quad (37)$$

$$\frac{\partial q_c}{\partial t} = -u \frac{\partial q_c}{\partial x} - v \frac{\partial q_c}{\partial y} - w \frac{\partial q_c}{\partial z} + \frac{S_c}{\bar{\rho}} + D_{q_c} + K_B \nabla^4 q_c \quad (38)$$

$$\frac{\partial q_r}{\partial t} = -u \frac{\partial q_r}{\partial x} - v \frac{\partial q_r}{\partial y} - (w + V_r) \frac{\partial q_r}{\partial z} + \frac{S_r}{\bar{\rho}} + D_{q_r} + K_B \nabla^4 q_r \quad (39)$$

$$\frac{\partial q_i}{\partial t} = -u \frac{\partial q_i}{\partial x} - v \frac{\partial q_i}{\partial y} - w \frac{\partial q_i}{\partial z} + \frac{S_i}{\bar{\rho}} + D_{q_i} + K_B \nabla^4 q_i \quad (40)$$

$$\frac{\partial q_s}{\partial t} = -u \frac{\partial q_s}{\partial x} - v \frac{\partial q_s}{\partial y} - (w + V_s) \frac{\partial q_s}{\partial z} + \frac{S_s}{\bar{\rho}} + D_{q_s} + K_B \nabla^4 q_s \quad (41)$$

where the terms  $S_v$ ,  $S_c$ ,  $S_r$ ,  $S_i$  and  $S_s$  represent sources and sinks of  $q_v$ ,  $q_c$ ,  $q_r$ ,  $q_i$  and  $q_s$ , respectively,  $Q_\theta$  represents sources and sinks of heat and  $V_r$  and  $V_s$  are the terminal velocities of raindrops and snowflakes, respectively.

#### d. Time-splitting

The complete set of prognostic equations for the COAMPS atmospheric model are (4)-(7), (23) and (36)-(41). Solving these fully-compressible, nonhydrostatic equations with an explicit time step is computationally expensive because of the speed of the sound waves. However, it is possible to isolate the terms that govern the sound waves in the dynamical equations (i.e., the left-hand-sides of (4)-(7)). Therefore, a short time step can be used for the left-hand-side terms while a longer time step, based on the advective speed, can be used for the right-hand-side terms. Note that the shorter time steps are not necessary for the thermodynamic, moisture and  $e$  equations.

The time-splitting technique used here follows that introduced by Klemp and Wilhelmson (1978). For a small time step,  $\Delta\tau_a$  and a large time step  $\Delta t_a$ , (4)-(7) are integrated as:

$$\begin{aligned}
u^{t-\Delta t_a+n\Delta\tau_a} &= u^{t-\Delta t_a+(n-1)\Delta\tau_a} \\
&\quad -\Delta\tau_a \left[ C_p \bar{\theta}_v \left( \frac{\partial \pi'}{\partial x} \right)^{(t-\Delta t_a+(n-1)\Delta\tau_a)} \right. \\
&\quad \left. + K_D \left( \frac{\partial D_3}{\partial x} \right)^{(t-\Delta t_a+(n-1)\Delta\tau_a)} \right. \\
&\quad \left. + RHS_u^t \right]
\end{aligned} \tag{42}$$

$$\begin{aligned}
v^{t-\Delta t_a+n\Delta\tau_a} &= v^{t-\Delta t_a+(n-1)\Delta\tau_a} \\
&\quad -\Delta\tau_a \left[ C_p \bar{\theta}_v \left( \frac{\partial \pi'}{\partial y} \right)^{(t-\Delta t_a+(n-1)\Delta\tau_a)} \right. \\
&\quad \left. + K_D \frac{\partial D_3}{\partial y} \right. \\
&\quad \left. + RHS_v^t \right]
\end{aligned} \tag{43}$$

$$\begin{aligned}
w^{t-\Delta t_a+n\Delta\tau_a} &= w^{t-\Delta t_a+(n-1)\Delta\tau_a} \\
&\quad -\Delta\tau_a \left[ C_p \bar{\theta}_v \left( \frac{\partial \pi'}{\partial z} \right)^{(t-\Delta t_a+(n-1)\Delta\tau_a)} \right. \\
&\quad \left. + K_D \frac{\partial D_3}{\partial z} \right. \\
&\quad \left. + RHS_w^t \right]
\end{aligned} \tag{44}$$

$$\begin{aligned}
(\pi')^{t-\Delta t_a+n\Delta\tau_a} &= (\pi')^{t-\Delta t_a+(n-1)\Delta\tau_a} \\
&\quad - \frac{\bar{c}^2 \Delta\tau_a}{C_p \bar{\rho} \bar{\theta}_v^2} (D_3)^{t-\Delta t_a+n\Delta\tau_a}
\end{aligned} \tag{45}$$

where  $RHS_u$ ,  $RHS_v$  and  $RHS_w$  are the right-hand-side terms in (4), (5) and (6), respectively. The diffusion coefficient  $K_D$  is chosen such that the ratio  $K_D \Delta\tau_a / \Delta x_i = 0.015$ .

e. *Boundary Conditions*

COAMPS requires the use of lateral as well as upper and lower boundary conditions. The lateral boundary conditions can be fixed, periodic, or radiation type similar to that proposed by Orlanski (1976). When using the radiation boundary conditions, all boundary values are set to their initial values at inflow points. At outflow boundary points, the normal velocity,  $v_n$ , is computed using upstream differencing as:

$$\frac{\partial v_n}{\partial t} = -(v_n + c_*) \frac{\partial v_n}{\partial n} \quad (46)$$

where  $v_n$  represents the velocity normal to the boundary and  $c_*$  is some estimate of the fastest moving gravity wave directed out of the domain. In COAMPS,  $c_*$  can either be specified or computed following the method described by Miller and Thorpe (1981). All other variables, other than  $v_n$ , are linearly extrapolated to the boundary on outflow. It should be noted that outflow points are determined by the sign of  $(v_n + c_*)$ . The upper and lower boundaries require specification of the vertical velocity and the fluxes. Currently, we set  $w = 0$  at both the upper and lower boundaries.

The lower boundary condition on the vertical mixing terms are:

$$-(\overline{u'w'}) = u_*^2 \frac{u}{|V|} \quad (47)$$

$$-(\overline{v'w'}) = u_*^2 \frac{v}{|V|} \quad (48)$$

$$-(\overline{w'\theta'}) = u_* \theta_* \quad (49)$$

$$-(\overline{w'q'_v}) = u_* q_* \quad (50)$$

where  $u_*$ ,  $\theta_*$  and  $q_{v*}$  are velocity, potential temperature and mixing ratio scale values and  $|V| = (u^2 + v^2)^{1/2}$  at the first grid height above the surface. We use the

Louis et al. (1982) surface flux parameterization to compute  $u_*$ ,  $\theta_*$  and  $q_{v*}$ . At the upper boundary, the normal gradient of the vertical mixing terms is assumed to vanish to prevent the development of unrealistic tendencies.

### 3. Ocean Model

#### a. Dynamics

The selection of the ocean model for COAMPS was determined by the type of experiments we anticipate performing. For the simulation of a tropical cyclone, Pudov et al. (1978), Hopkins (1982), Brooks (1983) and Shay and Elsberry (1987) all demonstrated that the oceanic response to a tropical cyclone can extend below the thermocline, hundreds of meters below the surface. Also, proper simulation of the response of the ocean mixed layer to a passing tropical cyclone is necessary. The ocean mixed layer exhibits deepening and strong mixing while the SST exhibits cooling due to the passage of a tropical cyclone (Fisher, 1958; Leiper, 1967; Price, 1981; Shay and Elsberry, 1987; Sanford et al., 1987; Brink, 1989). Therefore, we need a model capable of representing the deep (barotropic) response in the ocean as well as resolving the mixing processes within the mixed layer. We use the incompressible, hydrostatic equations similar to those described by Chang (1985) with two modifications. First, we extend the axisymmetric form of the equations to 3-dimensions. Second, we replace the predictive equation for the density ( $\rho$ ) with predictive equations for temperature ( $T$ ) and salinity ( $S$ ), and use the equation of state (Gill 1982) to diagnose the density from the temperature, salinity and pressure ( $p$ ). The equations become:

$$\frac{\partial \bar{u}}{\partial t} = \left[ -u \frac{\partial u}{\partial x} - v \frac{\partial u}{\partial y} - w \frac{\partial u}{\partial z} + fv + D_{ou} + K_B \nabla^4 u \right] - \frac{1}{\rho_0} \frac{\partial \bar{p}_r}{\partial x} \quad (51)$$

$$\frac{\partial u'}{\partial t} = \left[ -u \frac{\partial u}{\partial x} - v \frac{\partial u}{\partial y} - w \frac{\partial u}{\partial z} + fv + D_{ou} + K_B \nabla^4 u \right]' - \frac{1}{\rho_0} \frac{\partial p_r''}{\partial x} \quad (52)$$

$$\frac{\partial \bar{v}}{\partial t} = \left[ -u \frac{\partial v}{\partial x} - v \frac{\partial v}{\partial y} - w \frac{\partial v}{\partial z} - fu + D_{ov} + K_B \nabla^4 v \right] - \frac{1}{\rho_0} \frac{\partial \bar{p}_r}{\partial y} \quad (53)$$

$$\frac{\partial v'}{\partial t} = \left[ -u \frac{\partial v}{\partial x} - v \frac{\partial v}{\partial y} - w \frac{\partial v}{\partial z} - fu + D_{ou} + K_B \nabla^4 v \right]'' - \frac{1}{\rho_0} \frac{\partial p_r''}{\partial y} \quad (54)$$

$$\frac{\partial T}{\partial t} = -u \frac{\partial T}{\partial x} - v \frac{\partial T}{\partial y} - w \frac{\partial T}{\partial z} + D_{oT} + K_B \nabla^4 T \quad (55)$$

$$\frac{\partial S}{\partial t} = -u \frac{\partial S}{\partial x} - v \frac{\partial S}{\partial y} - w \frac{\partial S}{\partial z} + D_{oS} + K_B \nabla^4 S \quad (56)$$

$$\frac{\partial h}{\partial t} = -\frac{\partial(hu_s)}{\partial x} - \frac{\partial(hv_s)}{\partial y} - H \left( \frac{\partial u}{\partial x} + \frac{\partial v}{\partial y} \right) \quad (57)$$

$$\rho = f_\rho(T, S, p) \quad (58)$$

$$w(z) = \int_{-H}^z \left( \frac{\partial u}{\partial x} + \frac{\partial v}{\partial y} \right) dz \quad (59)$$

where all the variables are defined as above for the atmospheric model except that here,  $u$ ,  $v$  and  $w$  are ocean current speeds in the  $x$ -,  $y$ - and  $z$ -directions, the subscript  $s$  refers to the surface,  $D_{ou}$ ,  $D_{ov}$ ,  $D_{oT}$  and  $D_{oS}$  represent subgrid scale mixing of the  $u$ - and  $v$ -components and the temperature and salinity, respectively, and are defined below,  $H$  is the undisturbed mean height of the ocean,  $h$  is the deviation height from this mean, referred to as the free surface height,  $f_\rho$  symbolically represents the equation of state and  $p_r$  is the reference pressure, expressed as:

$$p_r(z) = p(z) - g\rho_0(H - z) \quad (60)$$

where  $\rho_0$  is the mean ocean density. The momentum equations have been decomposed into a vertical mean (barotropic mode) and the perturbation from this mean (baroclinic modes), expressed as,

$$(\ ) = (\bar{\ }) + (\ )'' \quad (61)$$

Therefore, the mean and perturbation reference pressures become:

$$\bar{p}_r = \frac{\bar{\rho}gh}{2} + g\overline{\rho''z} + \rho_s gh \quad (62)$$

and

$$p_r'' = p_r - \bar{p}_r \quad (63)$$

respectively, where  $\rho_s$  is the surface density.

The complete set of equations for the ocean model is comprised of (51)-(58), (62) and (63). As in the atmospheric model, the equations are solved on the staggered, scheme C grid. A similar staggering is used in the vertical with  $w$  defined at the interface between the layers and all other variables are defined at the middle of each layer. All derivatives are computed to second-order accuracy except the horizontal diffusion, which uses fourth-order accurate approximations to damp only the shortest wavelengths. High frequency time-oscillations are controlled using the Robert (1966) time filter using a smoothing parameter of 0.2.

*b. Subgrid Scale Mixing*

The subgrid scale mixing in the COAMPS ocean model is similar to that used in the FNOC Thermodynamical Ocean Prediction System (TOPS) (Clancy and Martin, 1979) and is based on the level-2 turbulence closure of Mellor and Yamada (1974). The mixing vertical terms are expressed as:

$$D_{ou} = \frac{\partial}{\partial z} (\overline{w'u'}) \quad (64)$$

$$D_{ov} = \frac{\partial}{\partial z} (\overline{w'v'}) \quad (65)$$

$$D_{oT} = \frac{\partial}{\partial z} (\overline{w'T'}) \quad (66)$$

$$D_{os} = \frac{\partial}{\partial z} (\overline{w'S'}) \quad (67)$$

where,

$$\overline{w'u'} = -lS_m q \frac{\partial u}{\partial z} = -K_{om} \frac{\partial u}{\partial z} \quad (68)$$

$$\overline{w'v'} = -lS_m q \frac{\partial v}{\partial z} = -K_{om} \frac{\partial v}{\partial z} \quad (69)$$

$$\overline{w'T'} = -lS_h q \frac{\partial T}{\partial z} = -K_{oh} \frac{\partial T}{\partial z} \quad (70)$$

$$\overline{w'S'} = -lS_h q \frac{\partial S}{\partial z} = -K_{oh} \frac{\partial S}{\partial z} \quad (71)$$

where  $l$  is the mixing length,  $S_h$  and  $S_m$  are constants computed as functions of the Richardson number,  $K_{oh}$  and  $K_{om}$  are the ocean eddy mixing coefficients and

$$q = (2e)^{1/2} \quad (72)$$

where  $e$  is the turbulent kinetic energy. The details for the calculations of  $S_h$  and  $S_m$  are presented in Mellor and Yamada (1974). The turbulent kinetic energy is computed assuming a balance between the shear production, the buoyancy production and the viscous dissipation,

$$lqS_m \left[ \left( \frac{\partial u}{\partial z} \right)^2 + \left( \frac{\partial v}{\partial z} \right)^2 \right] + lqS_h \left( \frac{g}{\rho} \frac{\partial \rho}{\partial z} \right) - \frac{q^3}{15l} = 0 \quad (73)$$

The mixing length,  $l$ , is expressed as:

$$l = \frac{kz}{1 + \frac{kz}{l_0}} \quad (74)$$

where  $k$  is the von Karman constant (0.4) and  $l_0$  is computed as:

$$l_0 = \frac{0.1 \int_{-H}^0 |z| q dz}{\int_{-H}^0 q dz} \quad (75)$$

where  $H$  is the depth of the ocean.

We use  $l_0$  from the previous time step when solving (73). Optionally, we could iterate each time step in the calculations of  $q$  and  $l$ , but experiments have shown that the solutions are not sensitive to this. Also, we compute the mixing terms (68) - (71) as adjustments at the end of each time step in an implicit formulation so that we are not constrained by the stability restrictions on  $K_{oh}$  and  $K_{om}$  necessary when using an explicit formulation of these terms. The horizontal mixing in the ocean model consists only of a background fourth-order diffusion, similar to that used in the atmospheric model described above.

### c. Time-splitting

One of the complicating factors in the numerical simulation of the ocean is the wide range of the phase speeds of the various modes within the ocean. Whereas the external (barotropic) mode is on the order of  $300 \text{ m s}^{-1}$ , the fastest internal mode is on the order of  $10 \text{ m s}^{-1}$  and the advective speeds rarely exceed  $1\text{-}2 \text{ m s}^{-1}$ . For efficiency, as with the atmospheric model, we use a time-splitting technique to reduce the number of computations. We solve for the barotropic mode with a small time step ( $\Delta\tau_0$ ) appropriate for the barotropic phase speed and a larger time step ( $\Delta t_0$ ) appropriate for the phase speed of the fastest internal mode, where  $\Delta t_0$  is an integer multiple of  $\Delta\tau_0$ . Only those equations that govern the barotropic mode are integrated with the smaller time step (i.e., (51), (53) and (57)). Also, the bracketed terms on the right-hand-side of (51) and (53) only need to be evaluated every large time step, saving additional computer time. The integration of  $\bar{u}$ ,  $\bar{v}$  and  $h$  are carried out using centered differencing in time and space, so that,

$$\begin{aligned}
 (\bar{u})^{t-\Delta t_0+(n+1)\Delta\tau_0} &= (\bar{u})^{t-\Delta t_0+(n-1)\Delta\tau_0} \\
 &\quad - 2\Delta\tau_0 \left[ B_u^t - \frac{1}{\rho_0} \left( \frac{\partial \bar{p}_r}{\partial x} \right)^{t-\Delta t_0+(n-1)\Delta\tau_0} \right] \quad (76)
 \end{aligned}$$

$$\begin{aligned}
(\bar{v})^{t-\Delta t_0+(n+1)\Delta\tau_0} &= (\bar{v})^{t-\Delta t_0+(n-1)\Delta\tau_0} \\
&\quad - 2\Delta\tau_0 \left[ B_v^t - \frac{1}{\rho_0} \left( \frac{\partial \bar{p}_r}{\partial y} \right)^{t-\Delta t_0+(n-1)\Delta\tau_0} \right] \quad (77)
\end{aligned}$$

$$\begin{aligned}
(h)^{t-\Delta t_0+(n+1)\Delta\tau_0} &= (h)^{t-\Delta t_0+(n-1)\Delta\tau_0} \\
&\quad - 2\Delta\tau_0 \left[ \frac{\partial(hu_s)}{\partial x} + \frac{\partial(hv_s)}{\partial y} \right]^{t-\Delta t_0+n\Delta\tau_0} \\
&\quad - 2\Delta\tau_0 H \left( \frac{\partial u}{\partial x} + \frac{\partial v}{\partial y} \right)^{t-\Delta t_0+n\Delta\tau_0} \quad (78)
\end{aligned}$$

where  $B_u$  and  $B_v$  are the barred and bracketed terms on the right-hand-side of (51) and (53), respectively.

#### d. Boundary Conditions

The lateral boundary conditions in the ocean model are similar to those used in the atmospheric model. We can use fixed, periodic or radiation type boundary conditions. When using the radiative boundary conditions, all boundary values are set to their initial values for inflow points. At outflow points, (46) is used to predict the normal velocity component while all other variables are linearly extrapolated to the boundary. The value of  $c_*$  is fixed at  $10 \text{ m s}^{-1}$ . We need only one boundary condition for the vertical velocity, since we allow for a free surface. We set  $w=0$  at the lower boundary and integration of the continuity equation (59) yields  $w$  at all other levels.

The upper boundary conditions on the vertical mixing terms are:

$$-(\overline{u'w'}) = \left( \frac{\rho_a}{\rho_o} \right) u_*^2 \frac{u}{|V|} \quad (79)$$

$$-(\overline{v'w'}) = \left( \frac{\rho_a}{\rho_o} \right) u_*^2 \frac{v}{|V|} \quad (80)$$

$$-(\overline{w'T'}) = - \left( \frac{\rho_a}{\rho_o C_{op}} \right) (C_p u_* T_* + L_v u_* q_*) \quad (81)$$

$$-(\overline{w'S'}) = \left(\frac{\rho_a}{\rho_o}\right)(u_*q_*S - P) \quad (82)$$

where  $u_*$ ,  $T_*$  and  $q_{v*}$  are the scale values of velocity, temperature and water vapor computed following Louis et al. (1982),  $\rho_a$  and  $\rho_o$  are the densities at the air-ocean interface of the atmosphere and ocean, respectively,  $C_{op}$  is the specific heat at constant pressure for the ocean and  $P$  is the precipitation rate at the surface. At the lower boundary, the normal gradient of the vertical mixing terms is assumed to vanish to prevent the development of unrealistic tendencies.

## 4. Model Tests and Results

### a. Background

The simulations reported here are based on data from Hurricane Gilbert, which moved from the Caribbean Sea into the Gulf of Mexico during the period of 8-19 September 1988. During its existence, Hurricane Gilbert established the record minimum pressure for a hurricane at 888 mb and attained a 700 mb wind speed of  $89 \text{ m s}^{-1}$  (Willoughby et al. 1989). Idealized initial conditions are used to construct homogeneous atmospheric and oceanic structures, typical of the environment near Gilbert, to demonstrate whether COAMPS can depict the development of the storm. In addition, features of Gilbert, such as concentric eye walls, as discussed by Black and Willoughby (1992) and the two-way interaction between Gilbert and the ocean are examined.

### b. Experiment 1: Uncoupled Simulation

The first experiment (EXP1) performed with COAMPS is an 84 h simulation of Hurricane Gilbert using a fixed sea surface temperature (SST). Therefore, only the atmospheric model grid was used in EXP1. The Cartesian grid consisted of 61 points in the east-west and north-south directions with a horizontal grid spacing of 10 km while 30 vertical levels were used with a constant spacing of 600 m. The speed of sound was arbitrarily set to  $100 \text{ m s}^{-1}$  in the model so that the large time step was 30 s and the small time step was 2.5 s. Radiative boundary conditions were used on the lateral boundaries with  $c_* = 30 \text{ m s}^{-1}$ . Since the ratio of the horizontal spacing to the vertical spacing is so large in this experiment, the meso-beta form of the subgrid scale mixing was employed. Rather than using (31) to compute the vertical mixing length, a value of  $l_V = 600 \text{ m}$  was chosen and modified for stable conditions based on (20) and (21). The vertical mixing length was further

constrained so that it was no less than 12 m.

The environmental data was chosen to try to simulate the rapid deepening associated with Hurricane Gilbert. A climatological SST of 302.36 K was obtained from the Generalized Digital Environmental Model (GDEM, Teague et. al., 1990) for the month of September at a position near where Gilbert attained it's maximum intensity (19.8°N, 83.9°W). The atmospheric temperature and moisture data was obtained from the Kingston, Jamaica sounding valid at 0000 UTC September 11 1988 (Fig. 1). In the mid- to upper-levels, the relative humidity was set to 0.05 per cent from 5500 m to 7100 m and to 0.005 per cent above 7100 m. A Rankine vortex, positioned at the center of the grid, was used to specify the initial wind field. Inside the radius of maximum winds ( $r_{max}$ ), the tangential velocity ( $v_{\theta}$ ) was computed as,

$$v_{\theta} = v_{max} \left( \frac{r}{r_{max}} \right) \left( 1 - \frac{r^2}{r_{in}^2} \right) \quad (83)$$

where  $v_{max}$  is the maximum tangential velocity (15 m s<sup>-1</sup>),  $r$  is the distance from the center of the storm and  $r_{max}$  is set to 90 km. Outside  $r_{max}$ ,

$$v_{\theta} = v_{max} \left( \frac{r}{r_{max}} \right)^x \left( 1 - \frac{r^2}{r_{in}^2} \right) \quad (84)$$

where  $x=0.6$  is an empirical constant and  $r_{in}$  is the radius of influence (240 km), beyond which  $v_{\theta}$  is set to zero. The vertical structure of the tangential wind is given by (83) and (84) below 10 km, and exponentially decreases to zero from 10 km to 13 km. For this simulation, no mean flow was used so that the entire initial wind field was comprised solely of the tangential wind from the Rankine vortex.

The initial pressure field was computed as follows. The divergence equation is formed from the horizontal equations of motion in which the time-tendencies, diffusion and turbulent mixing terms are set to zero. The elliptic equation for the

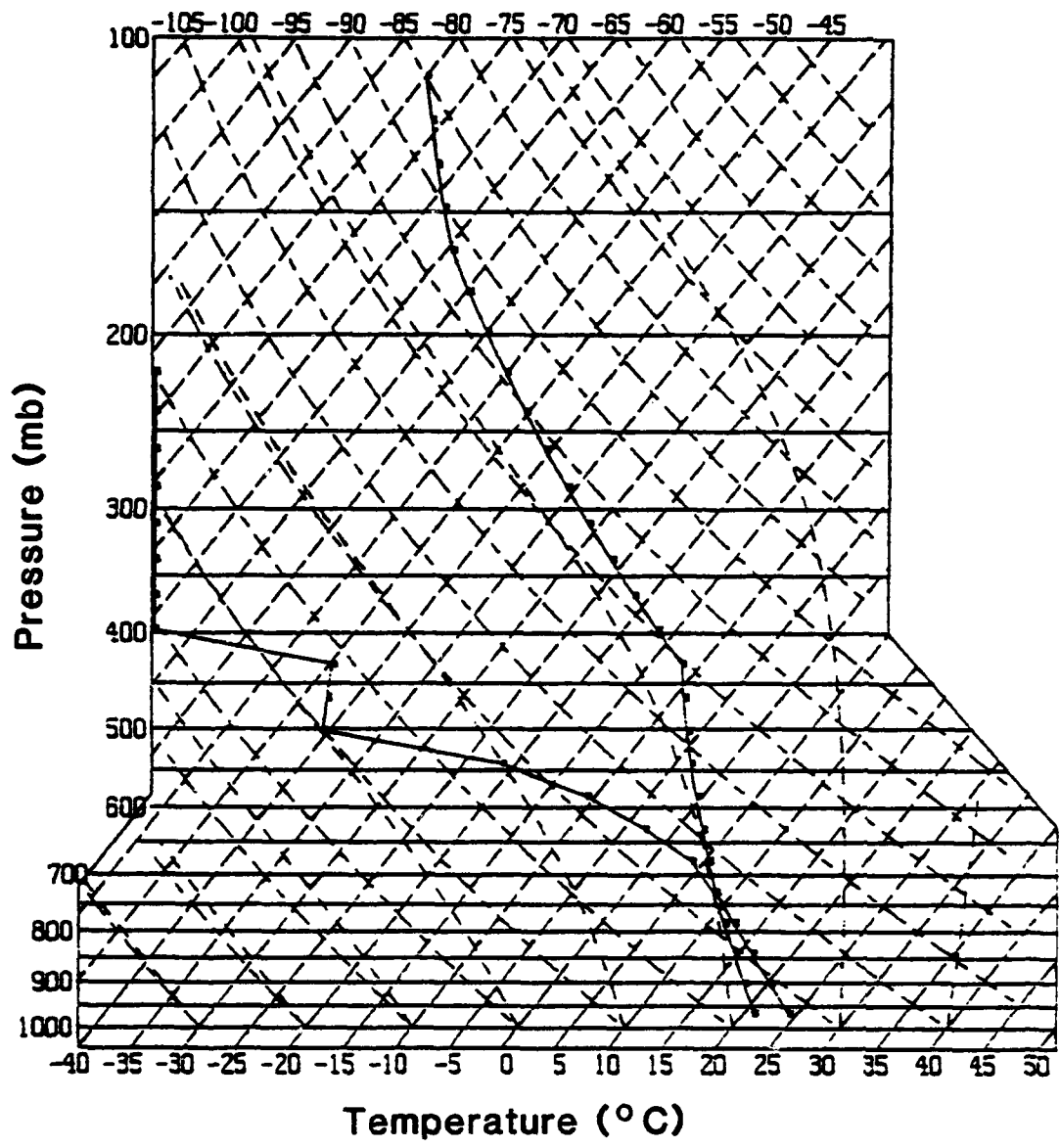


FIG. 1. Skew T-log  $p$  diagram with Kingston, Jamaica sounding for 0000 UTC 11 Sept 1988.

perturbation pressure becomes:

$$\nabla^2 \pi' = \frac{1}{C_p \bar{\theta}_v} \left[ \frac{\partial}{\partial x} \left( -u \frac{\partial u}{\partial x} - v \frac{\partial u}{\partial y} + f v \right) + \frac{\partial}{\partial y} \left( -u \frac{\partial v}{\partial x} - v \frac{\partial v}{\partial y} - f u \right) \right] \quad (85)$$

Eq. (85) is solved for each model level assuming that  $\pi' = 0$  on the lateral boundaries. After the  $\pi'$  fields are obtained, they are adjusted by subtracting the value of  $\pi'$  at the center of the grid for each level from all points on that level to insure that the data nearest the center of the grid remains as close to the original specified values as possible. The potential temperature field is then initialized using the vertical equation of motion (Eq. 6). By assuming that  $w$ , the time tendency of  $w$ , diffusion and turbulent mixing are zero, (6) can be written as:

$$\theta' = \frac{[C_p \bar{\theta}_v \frac{\partial \pi'}{\partial z}]}{[\frac{g}{\theta} - C_p (1 + q_v) \frac{\partial \pi'}{\partial z}]} \quad (86)$$

This leads to a maximum adjustment of the potential temperature of about  $-2^\circ\text{C}$  between 10-13 km above the surface and from 200 km from the center of the storm outward.

The initial conditions have been chosen so that the simulation could have the best chance of capturing the strong intensification associated with Gilbert. First, no environmental shear was included that may affect the vertical structure of the storm. Second, the SST associated with the position of maximum intensity of Gilbert was selected. Third, the SST was not allowed to vary in time as was observed (Shay et al., 1991) which could lead to a weakening of the system. This effect will be studied in the following section. Fourth, the model grid was set on an f-plane ( $17^\circ\text{N}$ ) with no mean wind so that the model storm stayed symmetrical and in the center of the grid to minimize effects of boundaries and asymmetries in the flow.

The 84 h COAMPS forecast minimum pressure and the maximum wind speeds for EXP1 and the observed minimum pressure for Gilbert are shown in Fig. 2.

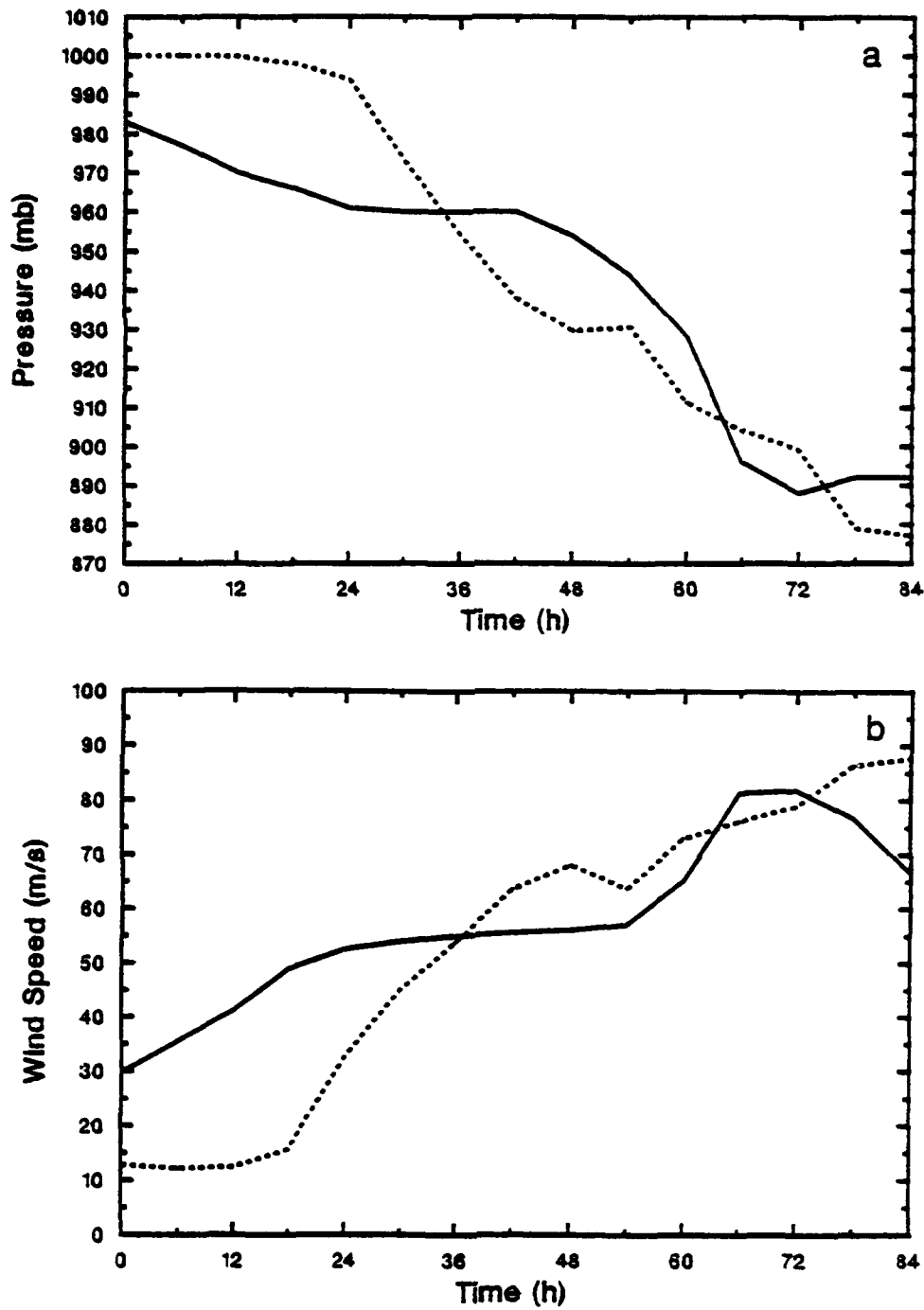


FIG. 2. a) Observed central pressure (mb) from 0000 UTC 11 Sept 1988 to 1200 UTC 14 Sept 1988 for Hurricane Gilbert (solid) and COAMPS central pressure forecast for EXP1 (dash). Values are plotted in 6 h increments. (b) As in (a) except for maximum wind speed ( $\text{m s}^{-1}$ ).

The initial time of the model simulation is taken to be 0000 UTC 11 September 1988 since this is the time of the sounding used for the initial conditions. At this time, Gilbert was observed to have a minimum pressure of approximately 983 mb. Over the next 36 h, Gilbert slowly deepened to about 960 mb, then remained at approximately this intensity for the next 12 h as it moved over the island of Jamaica. Gilbert deepened rapidly over the next 24 h to attain a record low pressure of 888 mb at 0000 UTC 14 September, corresponding to 72 h in the model simulation. At this time, Gilbert attained a maximum wind speed of approximately  $83 \text{ m s}^{-1}$ .

Two distinct stages of development of Gilbert in EXP1 can be seen from Fig. 2. In the first stage, defined as the first 24 h of the simulation, the central pressure remained nearly constant at 1000 mb. During this stage, the model storm developed low-level inflow in response to the surface friction and a warm, moist PBL due to the sensible and latent heat fluxes. In the second stage, defined as the last 60 h period from 24 h to 84 h of the simulation, the model storm exhibited rapid deepening from 1000 mb to the minimum of 874 mb at 81.5 hours. Although the pressure fell during this second stage, there were periods of pressure rises and quasi-steady state behavior imbedded within the general pattern of pressure falls. A description of these two stages of the model storm development follows.

During the first stage, the model storm developed inflow in the lowest levels through surface friction. This led to an initial spin-down of the storm circulation for approximately the first 12 h until the induced upward motion initiated convection. This convection formed near the radius of maximum winds, initially set at 90 km, but rapidly contracted inward. East-west cross-sections of the  $v$ -component (i.e., tangential wind) for 0 h, 12 h and 24 h in Fig. 3 show the initial decay of the circulation followed by a spin-up with the maximum tangential velocity over  $30 \text{ m s}^{-1}$  at 24 h only 40 km from the center of the circulation.

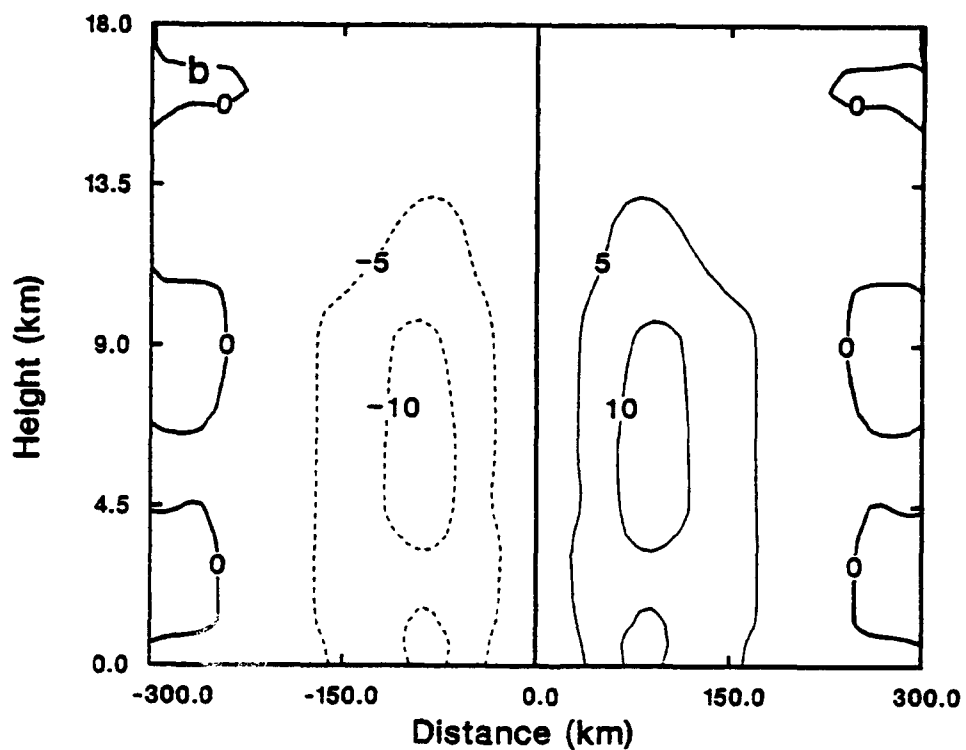
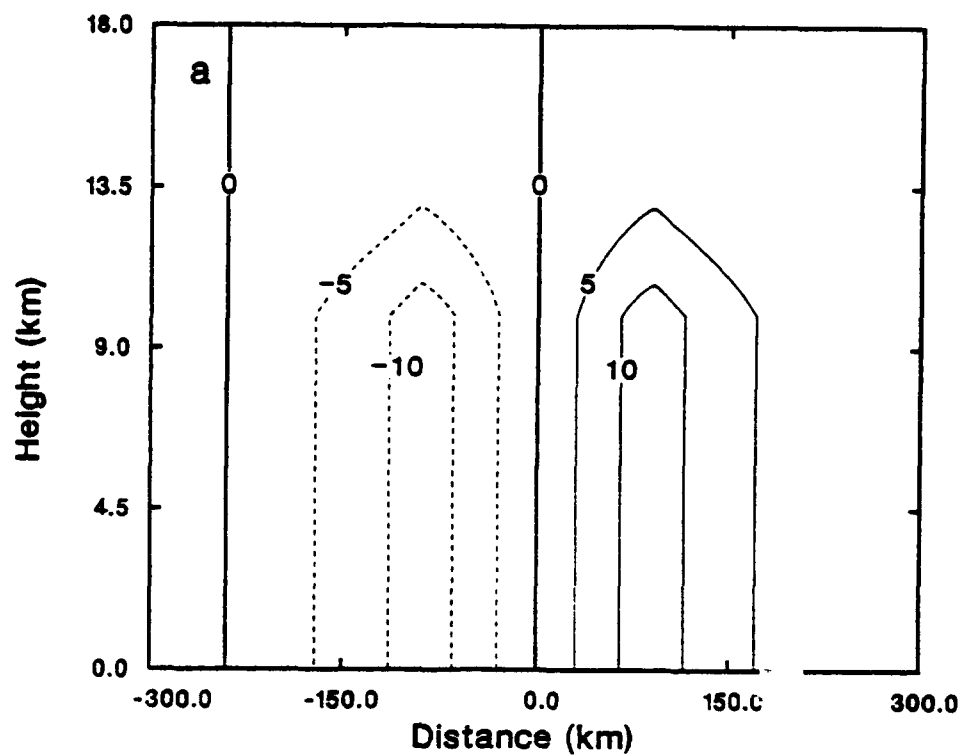


FIG. 3. East-west vertical cross-sections of the tangential velocity ( $\text{m s}^{-1}$ ) taken through the center of the grid for EXP1 for a) 0 h, b) 12h, and c) 24h. Contour interval is  $5 \text{ m s}^{-1}$ .

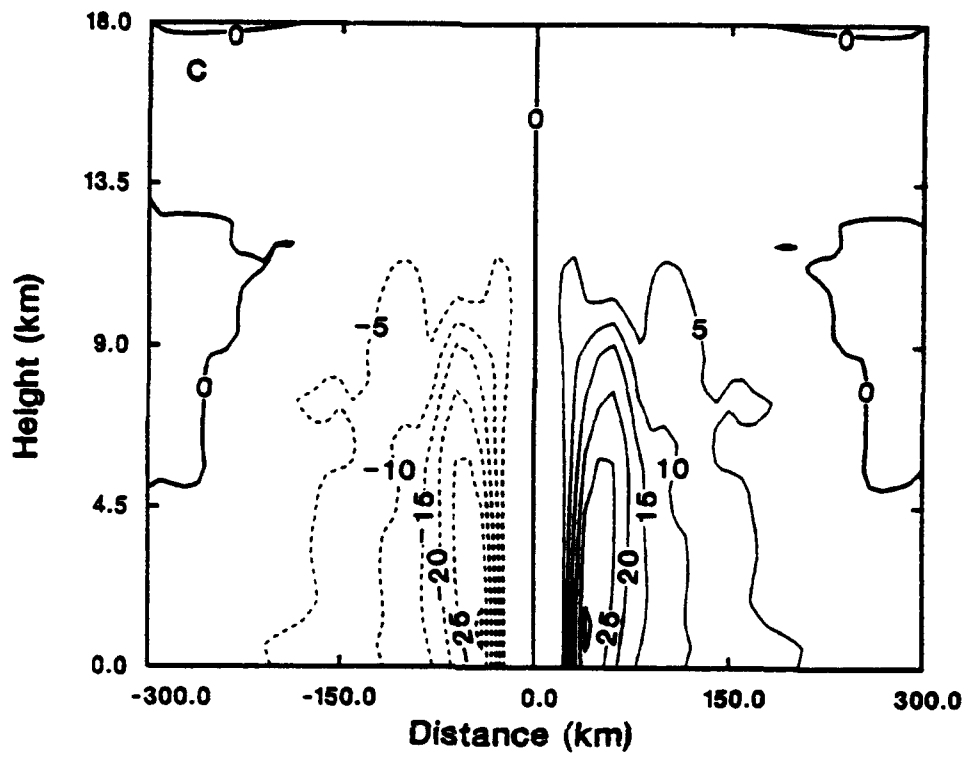


FIG. 3, continued.

The maximum wind speed in the model started increasing at 19 h of the simulation during which time the minimum pressure remained constant. The increase of the maximum wind prior to the central pressure fall is similar to that reported by Rosenthal (1977). The increase in wind speed occurs about 12 h after the first convective towers formed in the eye wall. However, it is only 2 hours after the development of ice crystals atop the eye wall convection. The added heat release due to the formation of the ice clouds appears to be a significant factor in causing the deepening of the system as also found by Tripoli (1992b).

The second stage of development of EXP1 was characterized by the rapid fall of the central pressure from approximately 1000 mb to 874 mb. During this period, the model storm developed many features that have been observed in tropical cyclones. Model generated radar reflectivities at 3300 m, computed following Rutledge and Hobbs (1983) formulation, for every 12 h from 24 h to 84 h (Fig. 4) illustrate the structure of the convection in the model storm. Strong convective cells (greater than 40 dBz) are evident in a ring surrounding the eye at a radius of 20-40 km. No precipitation is found in the eye. By 48 h, the appearance of spiral bands of convection at radii ranging from 50-200 km is noted. Within these bands, convective cells propagate inward with reflectivities often equal to cells within the eye wall. The pattern of 4 symmetric spiral bands is due to the use of an f-plane, no mean flow and the storm being located in the center of a square grid.

The cross-section of the vertical velocity at 84 h (Fig. 5) illustrates the upward motion associated with the eye wall convection. In general, the maximum upward motion within the eye wall varied in time from 2-6  $\text{m s}^{-1}$ . This was also found to be the case for the individual convective elements within the spiral bands. Downward motion within the eye exhibited a maximum of about -0.5  $\text{m s}^{-1}$  near 9 km with weaker subsidence extending nearly to the surface. The vertical motion associated

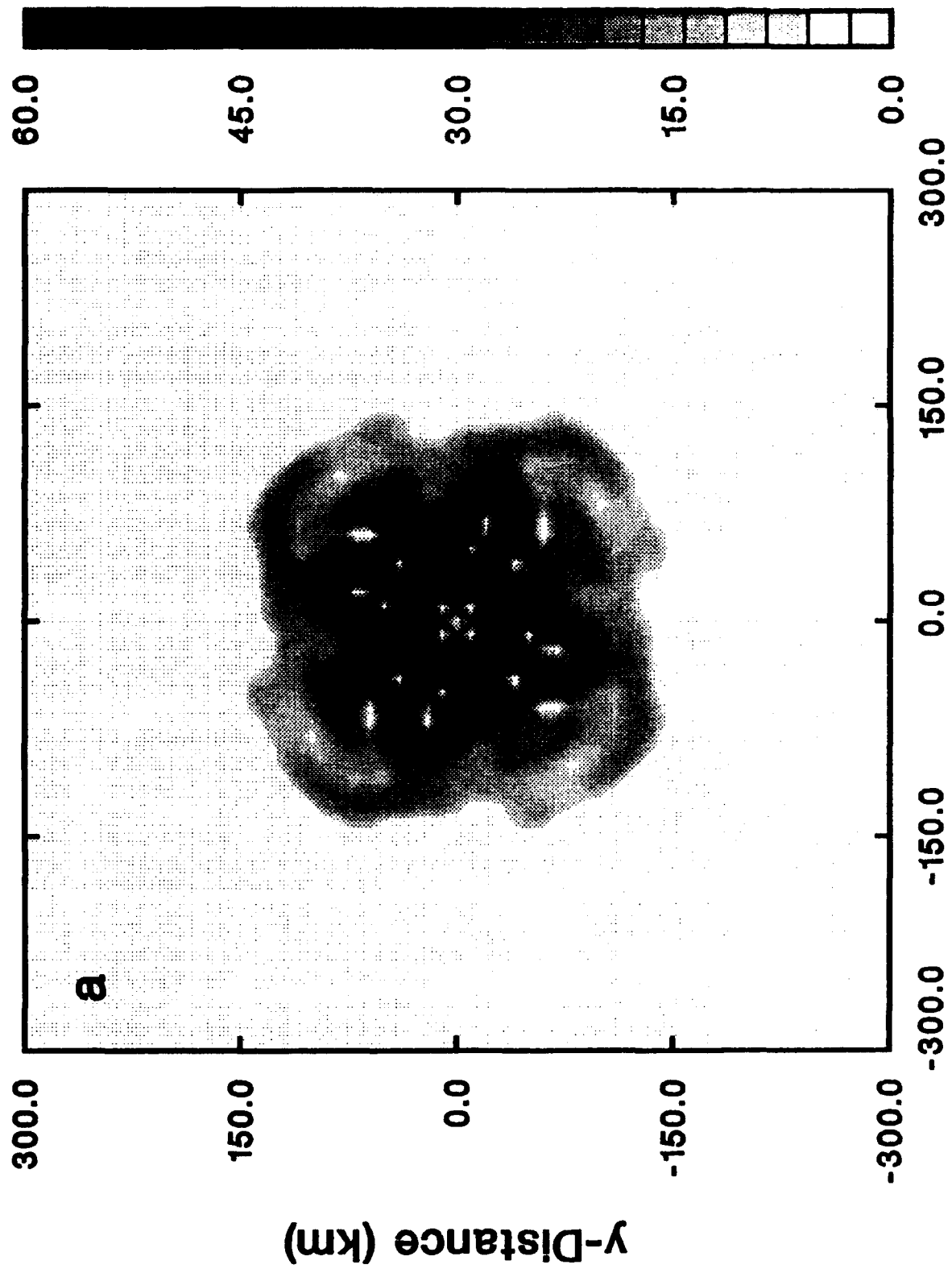


FIG. 4. Model generated radar reflectivities (dBz) at 3300 m for EXP1 at (a) 24 h, (b) 36 h, (c) 48 h, (d) 60 h, (e) 72h, and (f) 84 h.

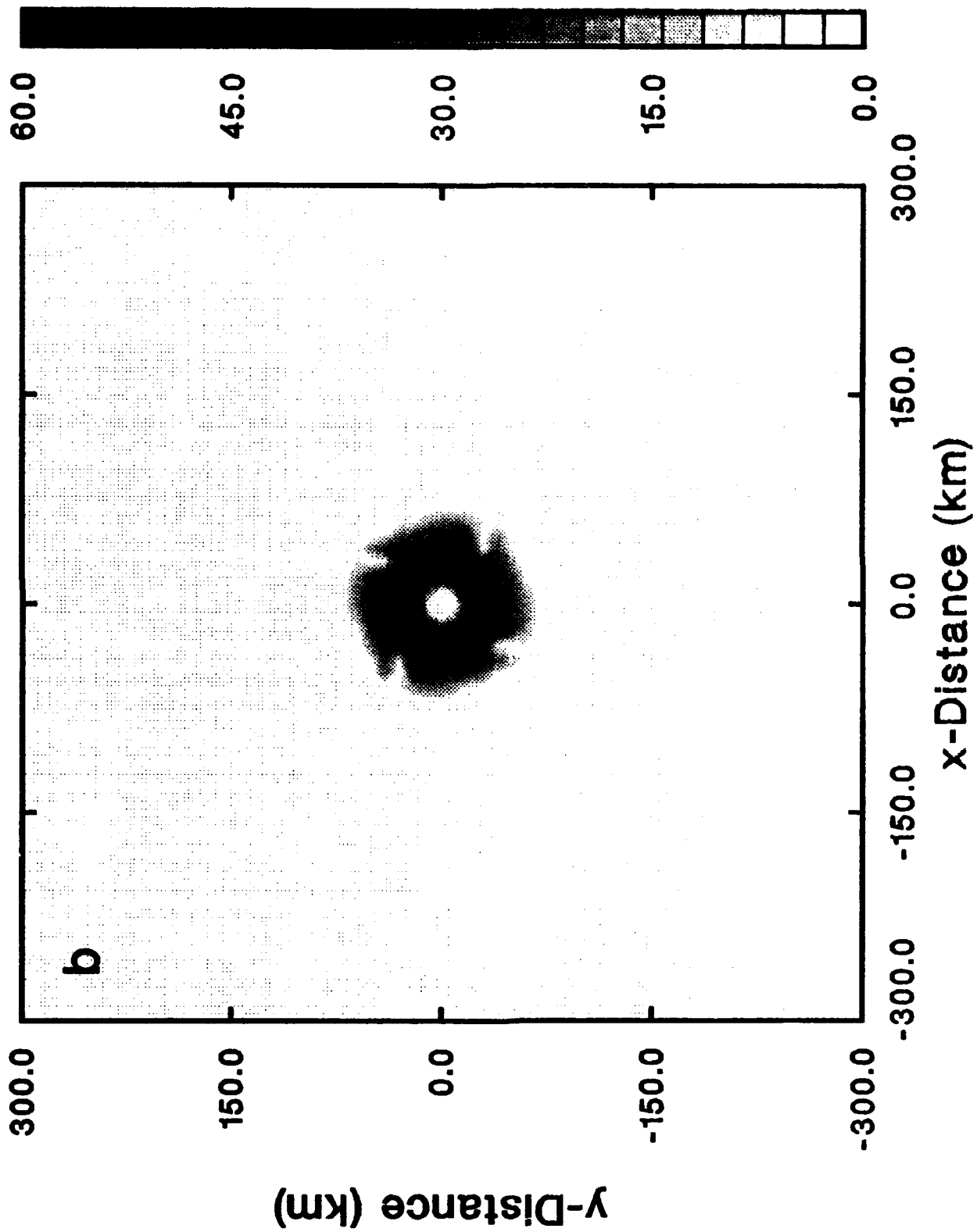


FIG. 4, continued.

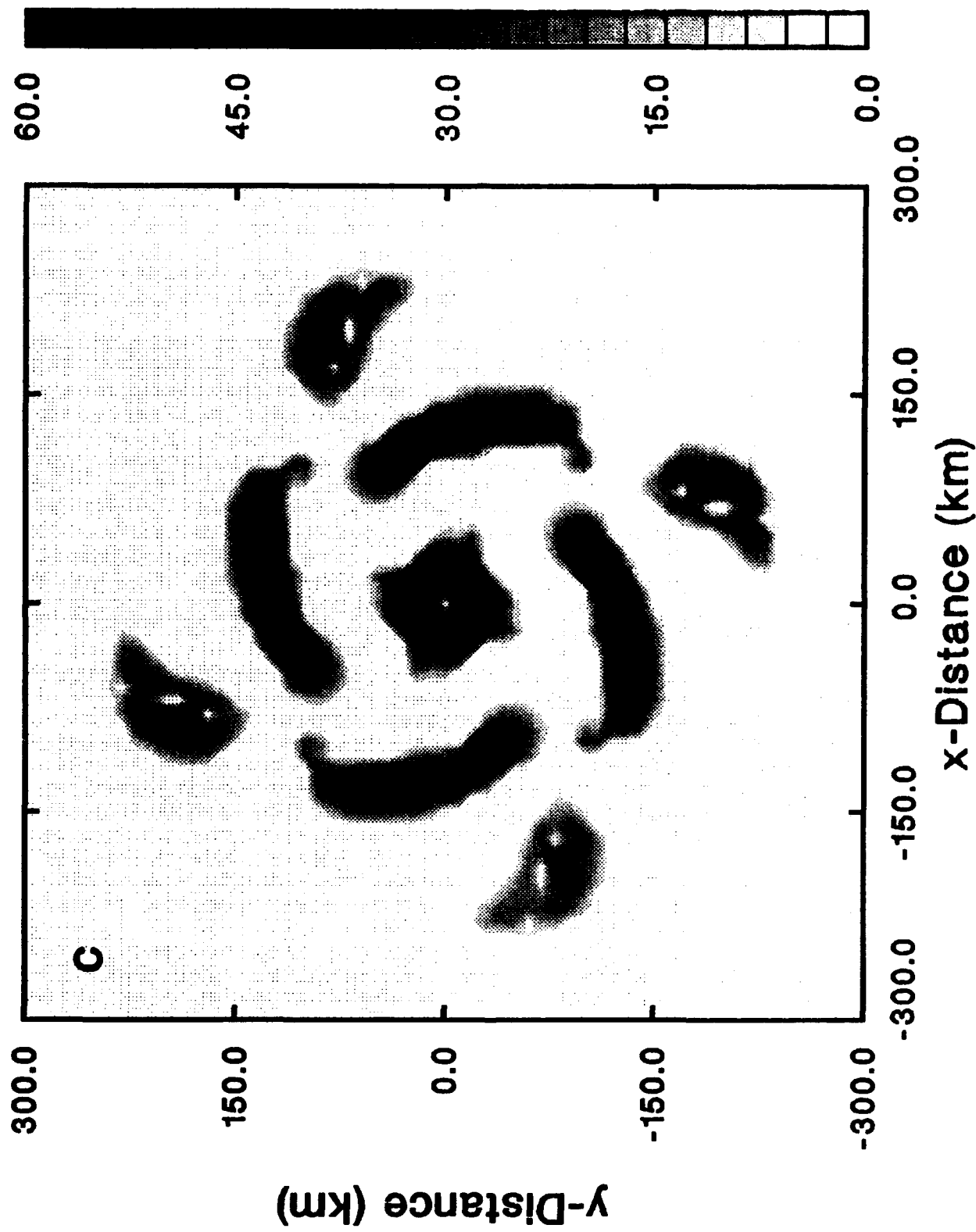


FIG. 4, continued.

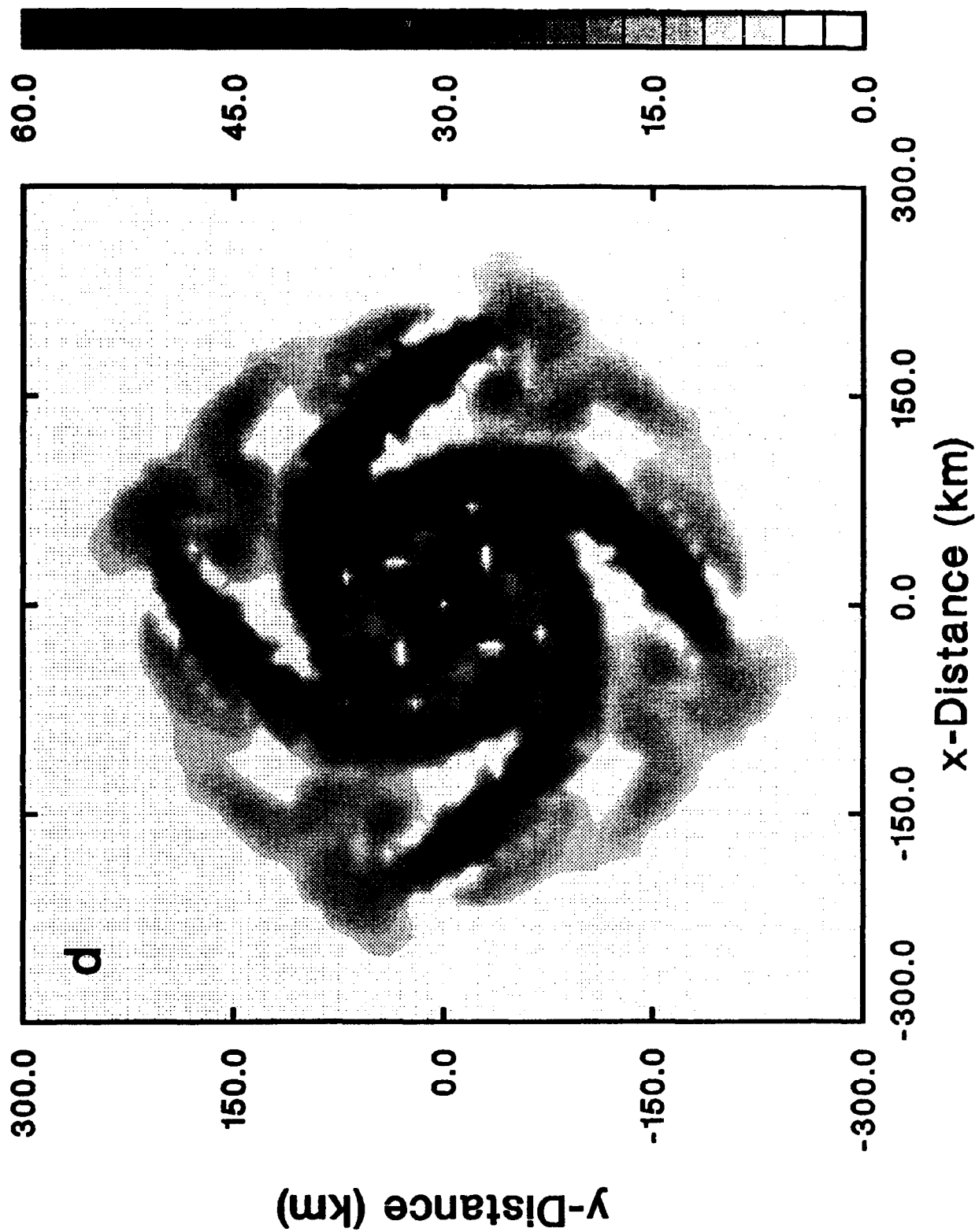


FIG. 4, continued.

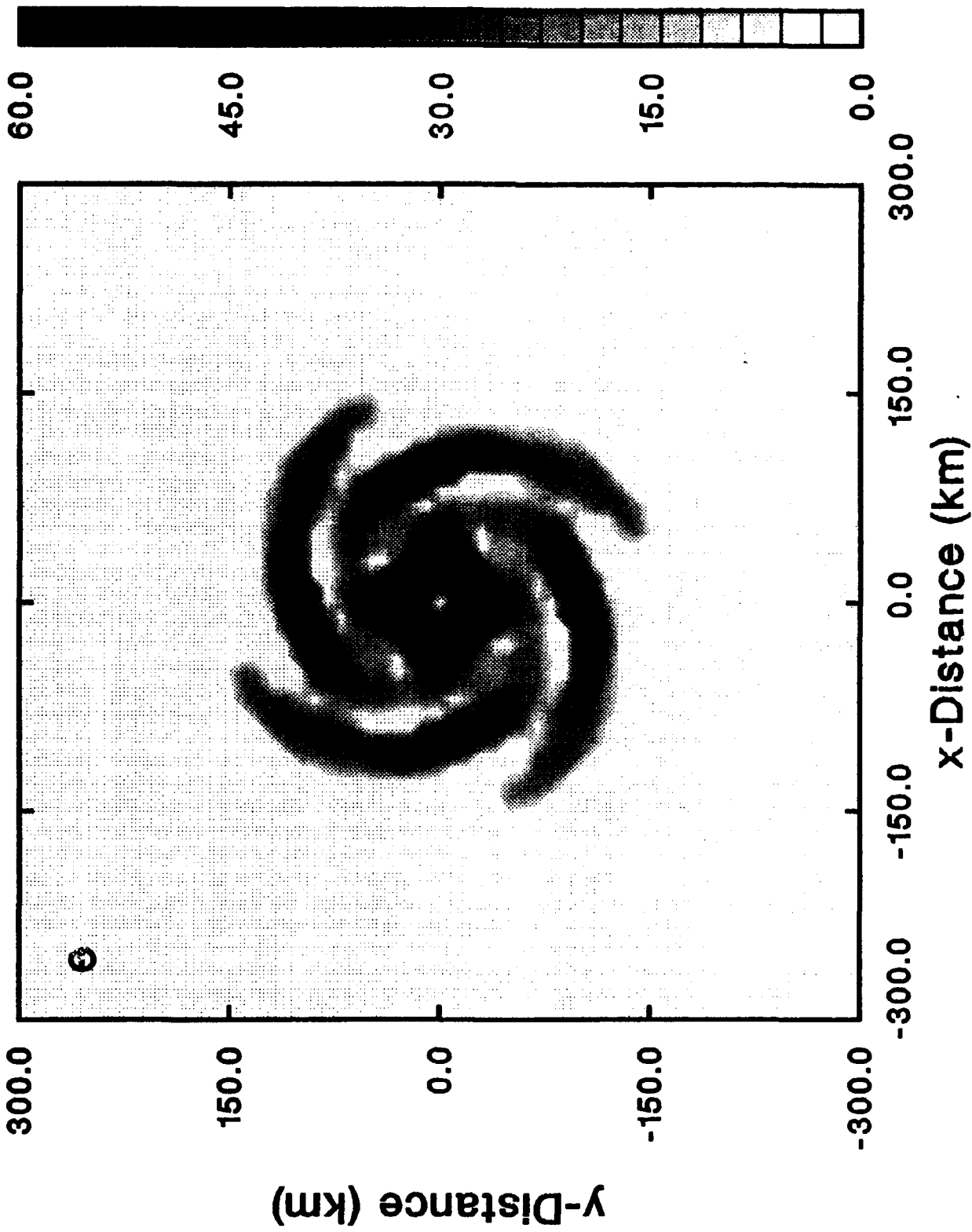


FIG. 4, continued.

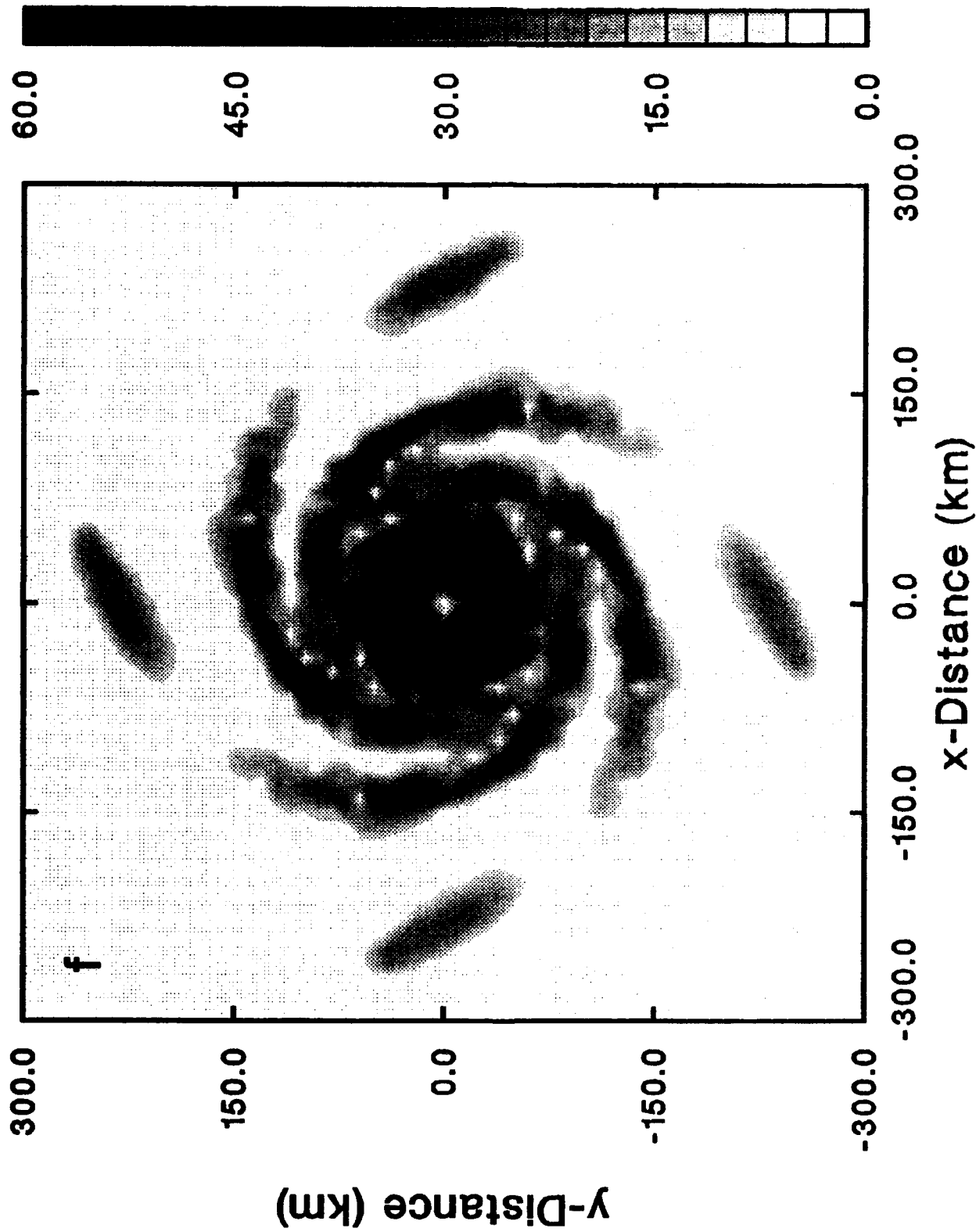


FIG. 4, continued.

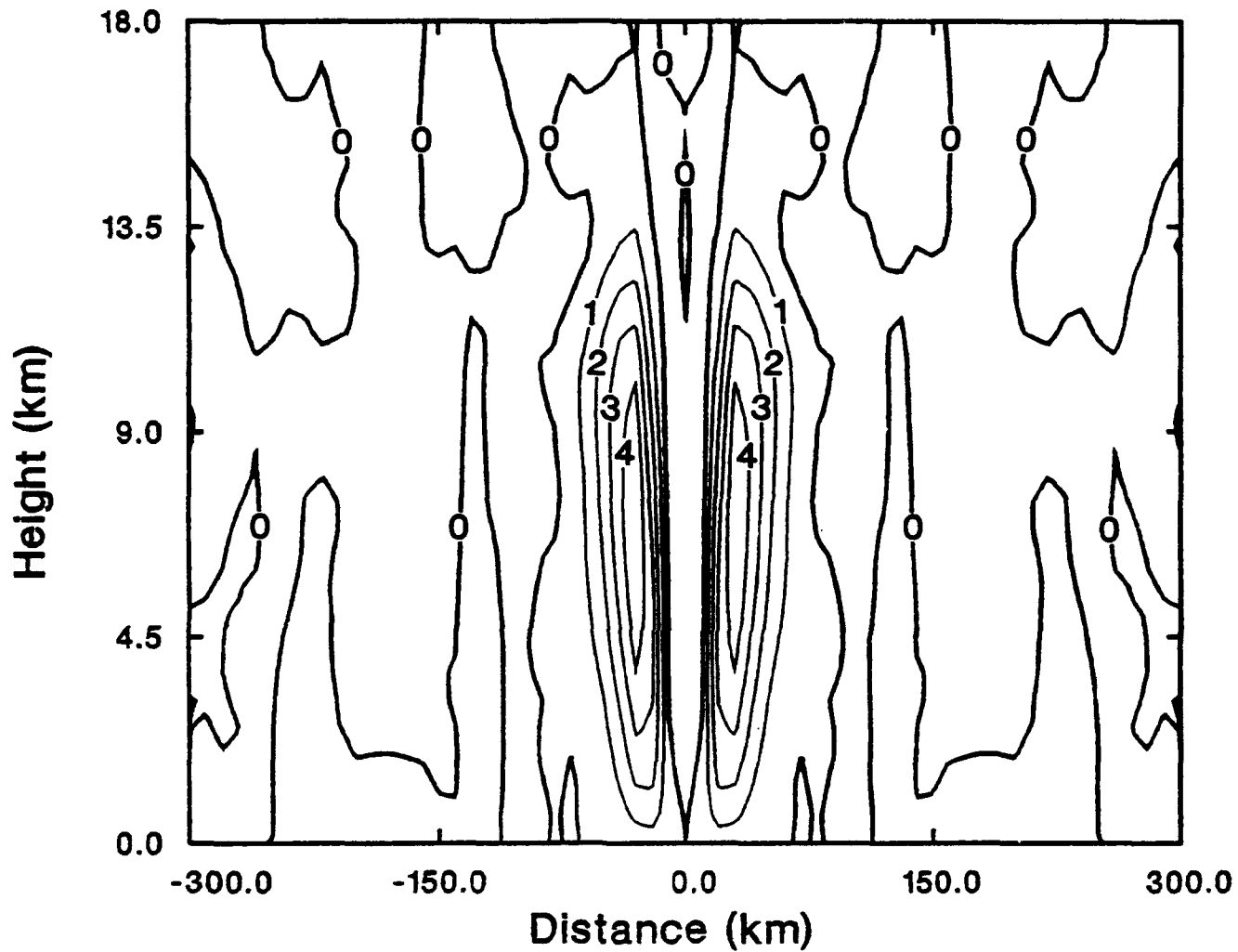


FIG. 5. East-west vertical cross-sections of the vertical velocity ( $\text{m s}^{-1}$ ) taken through the center of the grid for EXP1 at 84 h. Contour interval is  $1 \text{ m s}^{-1}$ .

with the eye wall convection slanted outward with height as has been found by Rosenthal (1977).

The radial wind component at 48 h is shown in Fig. 6a. Inflow of over  $10 \text{ m s}^{-1}$  dominates below 1 km near the eye wall indicating the large convergence in this region. A secondary maximum in low-level convergence is found at about 100 km from the center of the storm in conjunction with the spiral bands. In general,  $5 \text{ m s}^{-1}$  inflow exists throughout the lowest kilometer. Outflow is found at 10-13 km with speeds in excess of  $10 \text{ m s}^{-1}$ . By 84 h, a much stronger radial circulation has developed (Fig. 6b). The near-surface inflow is now over  $20 \text{ m s}^{-1}$  with inflow over  $5 \text{ m s}^{-1}$  up to nearly 4 km. A strong outflow of over  $25 \text{ m s}^{-1}$  exists at about 12 km.

It was shown earlier that the central pressure of the model storm increased somewhat after about 48 h of simulation. This coincides with the formation of the spiral bands of convection. These bands acted as a dynamic part of the system, occasionally contracting inward toward the eye with noticeable changes on the central pressure and maximum wind speed. Willoughby et al. (1982) noted that concentric eye walls have been observed in intense, symmetric hurricanes. Furthermore, the outermost concentric ring of convection typically contracts inward, thereby weakening the innermost ring of convection until the outer ring replaces the inner ring as the eye wall. During the period of the contraction of the outer ring, the storms were observed to weaken in intensity, with rapid intensification following the replacement of the eye wall by the outer ring. Other observational studies (Fortner 1958, Jordan and Schatzle 1961, Jordan 1966, Holliday 1977 and Willoughby 1992) show that the eye of the storm is somewhat larger after the replacement of the inner eye wall by the outer eye wall.

Shapiro and Willoughby (1982) demonstrated that a heat source, such as from

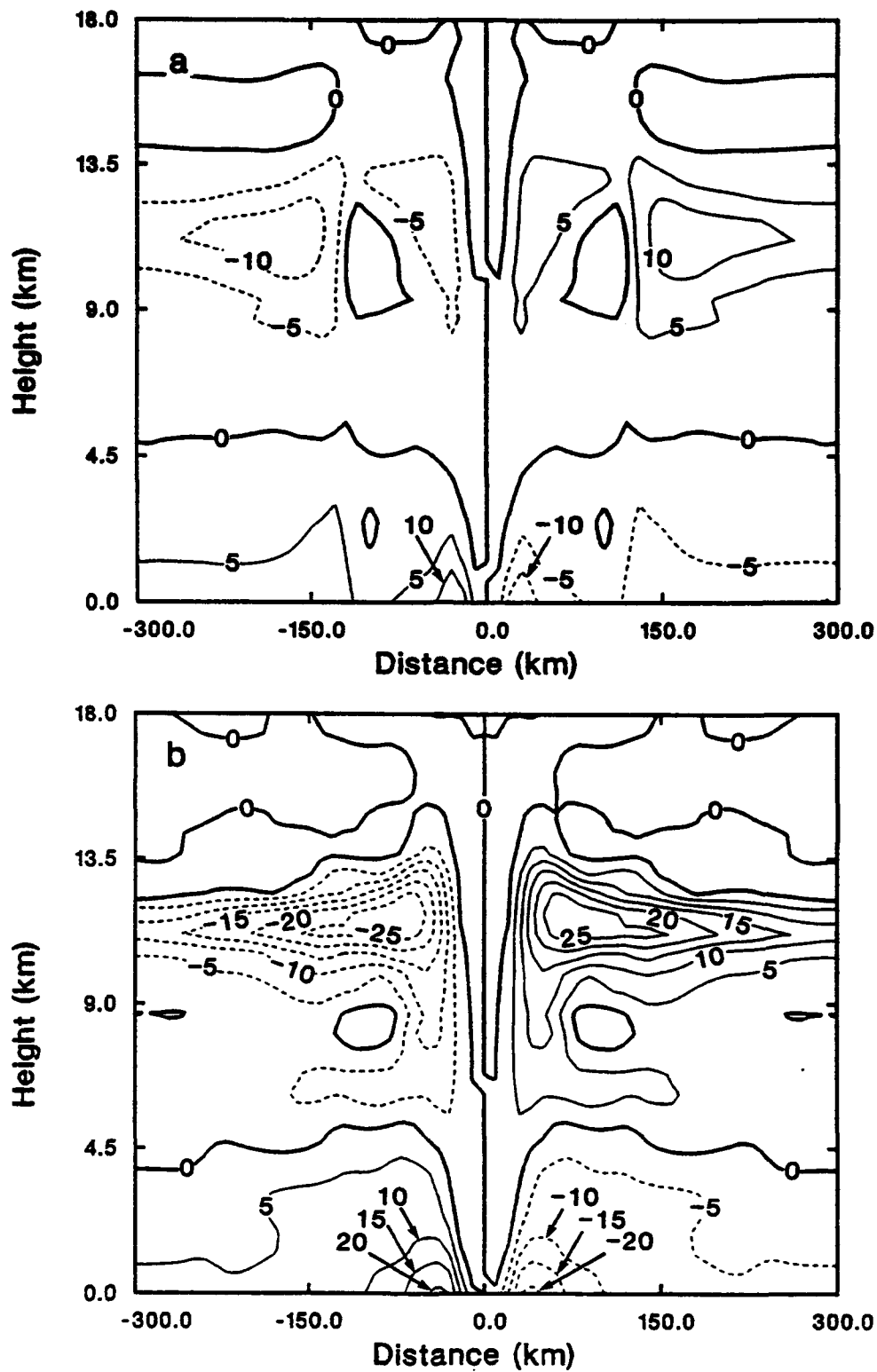


FIG. 6. East-west vertical cross-sections of the radial wind ( $\text{m s}^{-1}$ ) taken through the center of the grid for EXP1 at (a) 48 h, and (b) 84 h. Contour interval is  $5 \text{ m s}^{-1}$ .

convection, near a maximum in tangential wind leads to larger heat falls inside the radius of maximum winds than outside. This leads to a propagation inward of the tangential wind maximum and the associated heat source. The contraction of the wind maximum often leads to a destruction of an inner wind maximum and an eventual replacement by the outer wind maximum.

Several occurrences of concentric eye walls were present in EXP1 after 48 h of the simulation. One of the most significant occurred during the period from 48 h to 60 h. Model generated radar reflectivities for the 3300 m height at 48 h, 50 h, 52 h, 54 h, 56 h and 57 h are given in Fig. 7. At 48 h, a ring of convection is found around the eye with the newly formed spiral bands over 100 km from the center of the storm. The maximum reflectivity in the eye wall is found 20 - 30 km from the eye. Over the next 6 hours, the spiral bands slowly converge in toward the eye, forming a nearly closed ring of convection around the eye at a radius of about 70 km by 54 h. By this time, the radar reflectivities are larger in the outer eye wall than in the inner eye wall. At 56 h, it appears that the outer and inner eye walls are merging into one. Individual cloud elements make up a relatively disorderly pattern of convection from 20-60 km from the eye. One hour later, at 57 h, the concentric rings have merged into one eye wall, with the maximum reflectivities now about 35-40 km from the eye.

The central pressure and maximum wind speeds for the time period of 48 h to 60 h are shown in Fig. 8 with a higher temporal resolution than was used in Fig. 2a. From 48 h to 50.5 h, the period in which the spiral band was still at least 80 km from the eye, the pressure continued to fall and the wind speed continued to rise. From 50.5 h to 54.25 h, the time period over which the outer eye wall contracted from 80 km to 60 km, the central pressure rose 6.5 mb and the maximum wind decreased  $8.5 \text{ m s}^{-1}$ . Only after 54.25 h, when the outer and

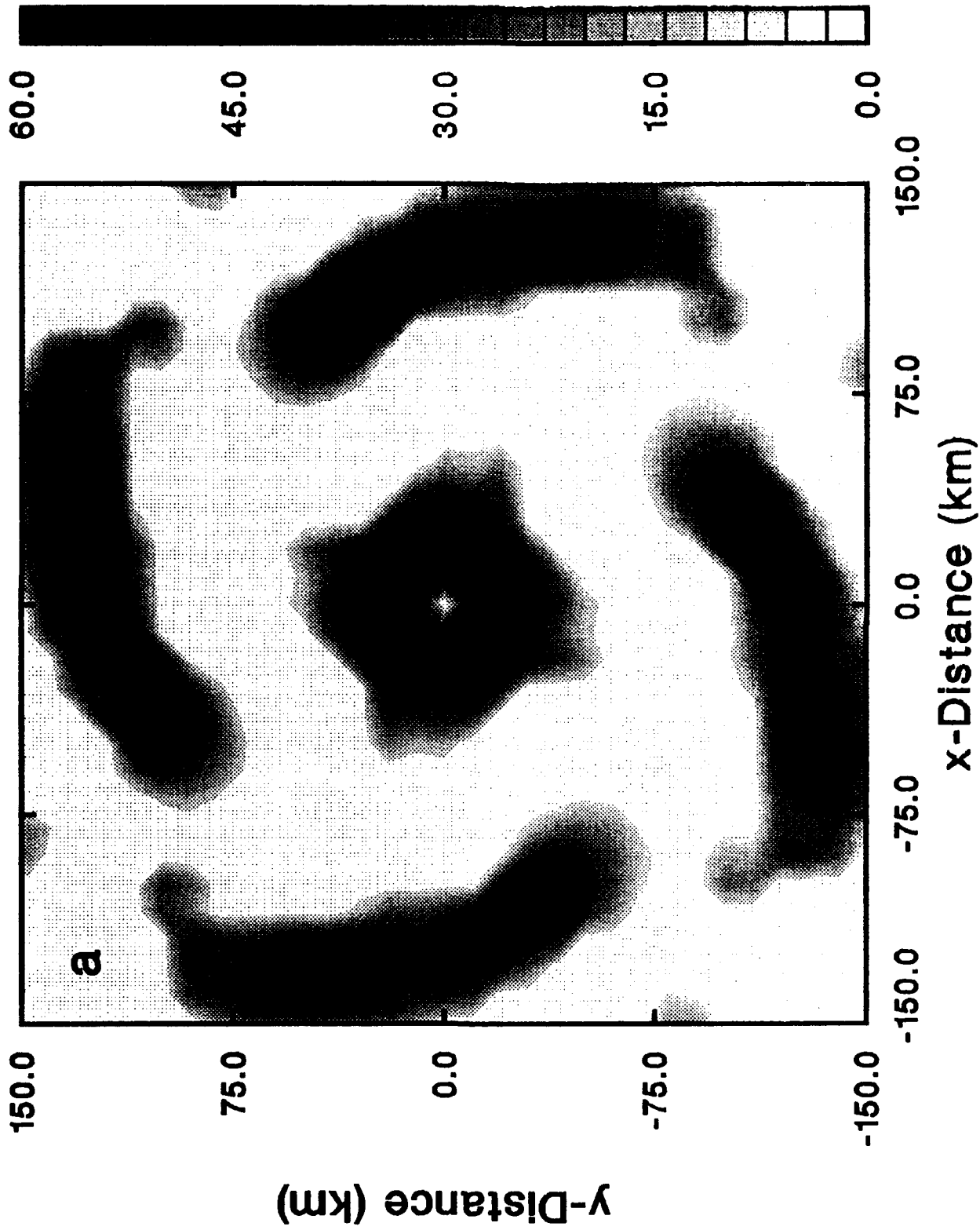


FIG. 7. Model generated radar reflectivities at 3300 m for EXP1 over central 21 x 21 grid points at (a) 48 h, (b) 50 h, (c) 52 h, (d) 54 h, (e) 56 h, and (f) 57 h.

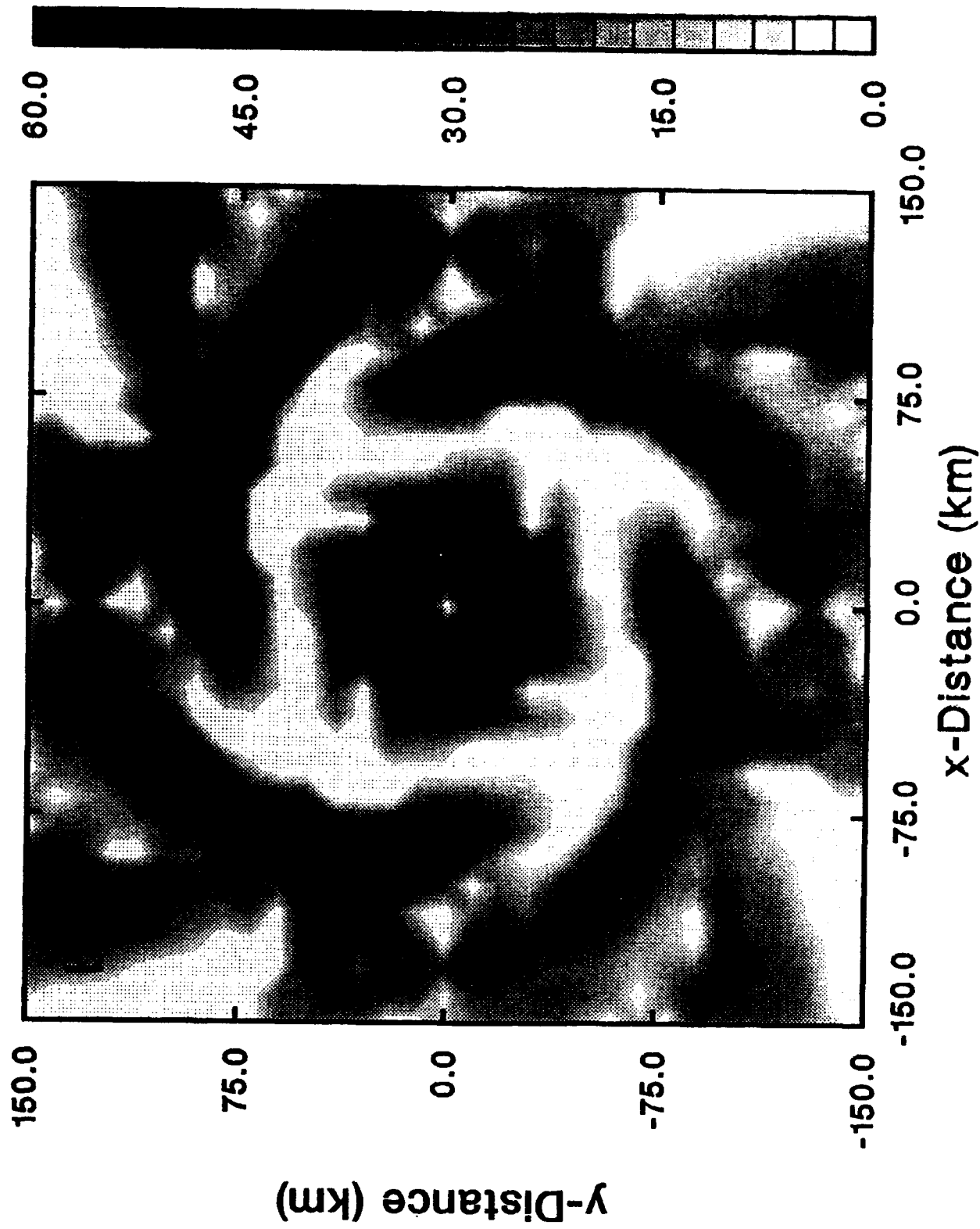


FIG. 7, continued.

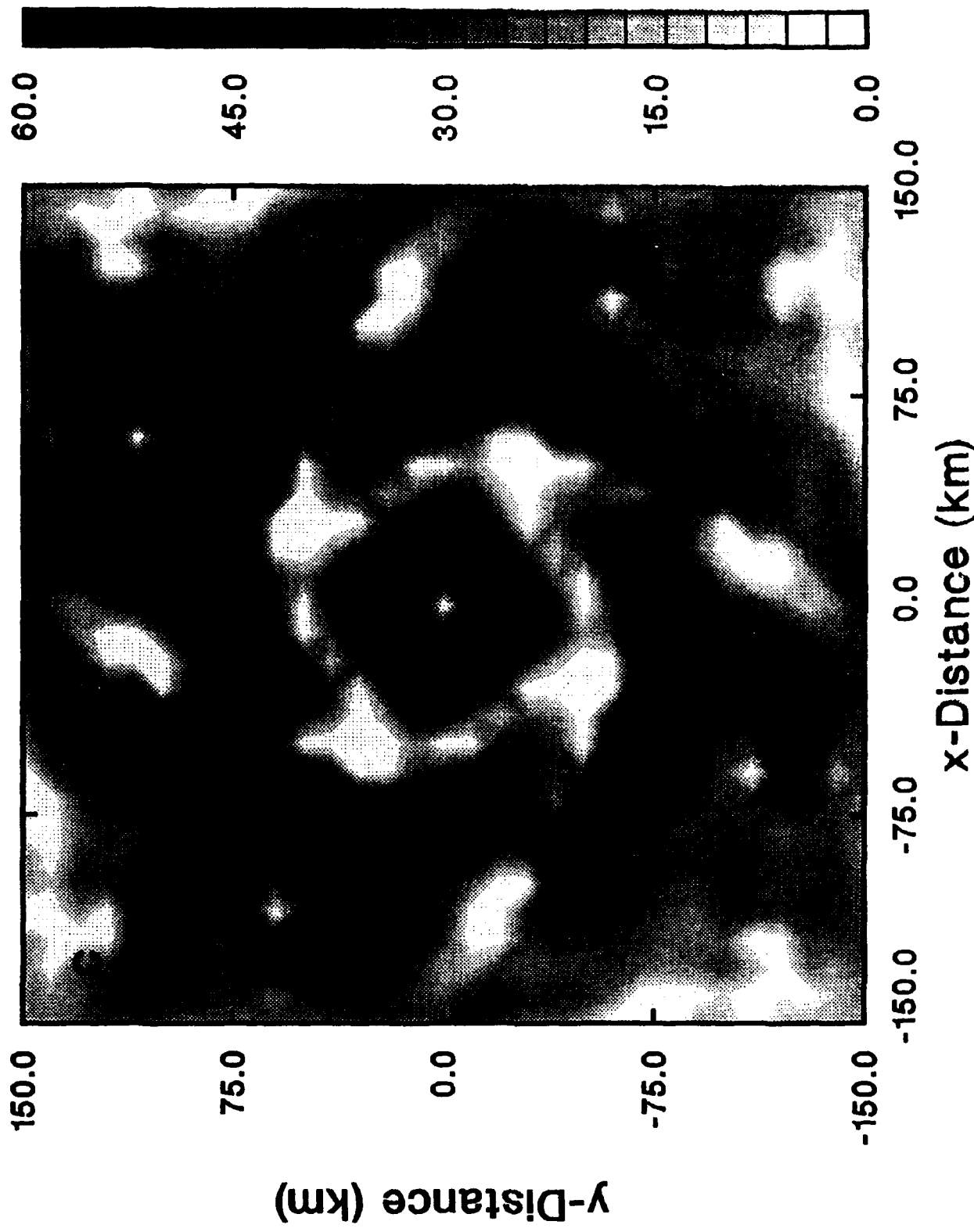


FIG. 7, continued.

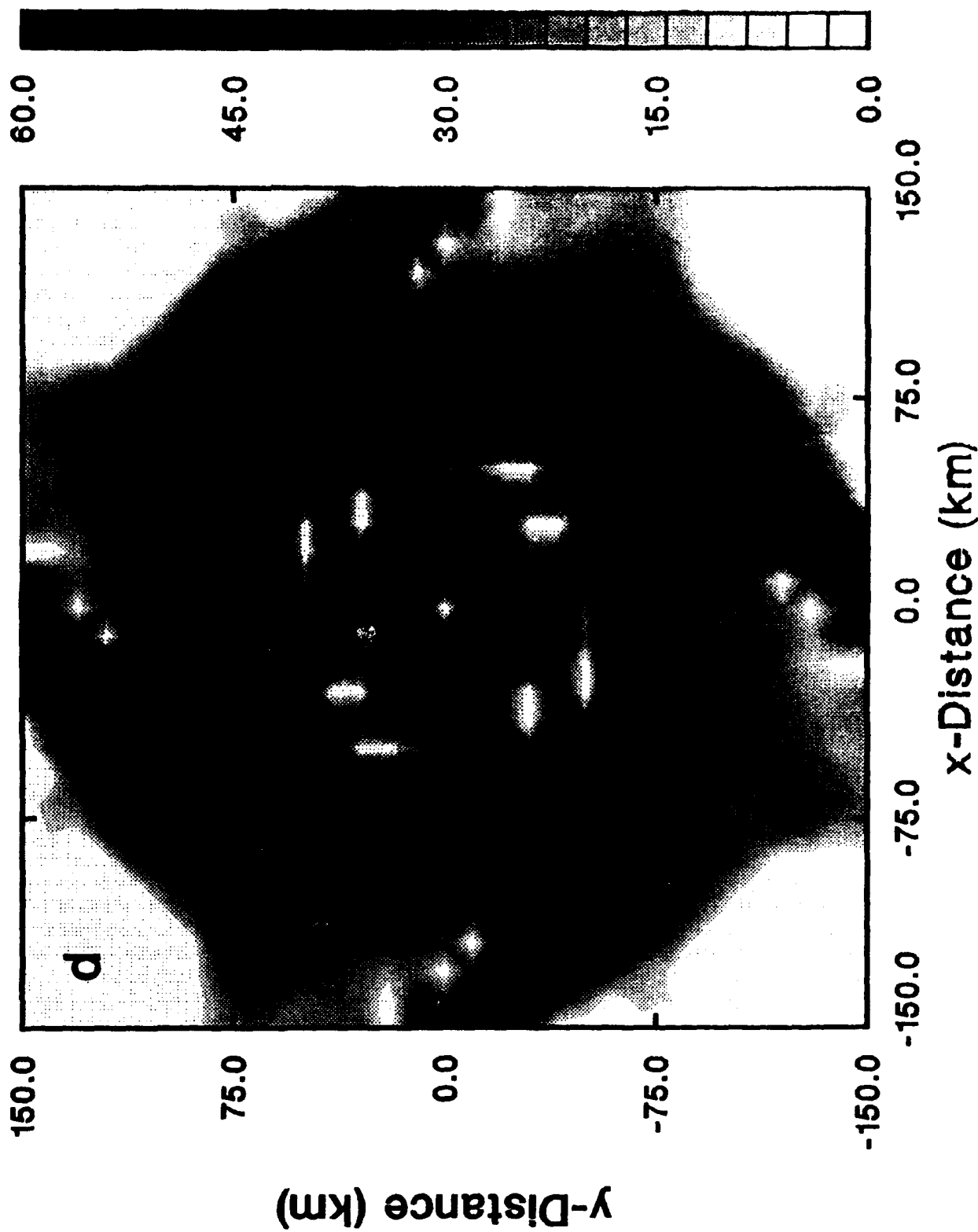


FIG. 7, continued.

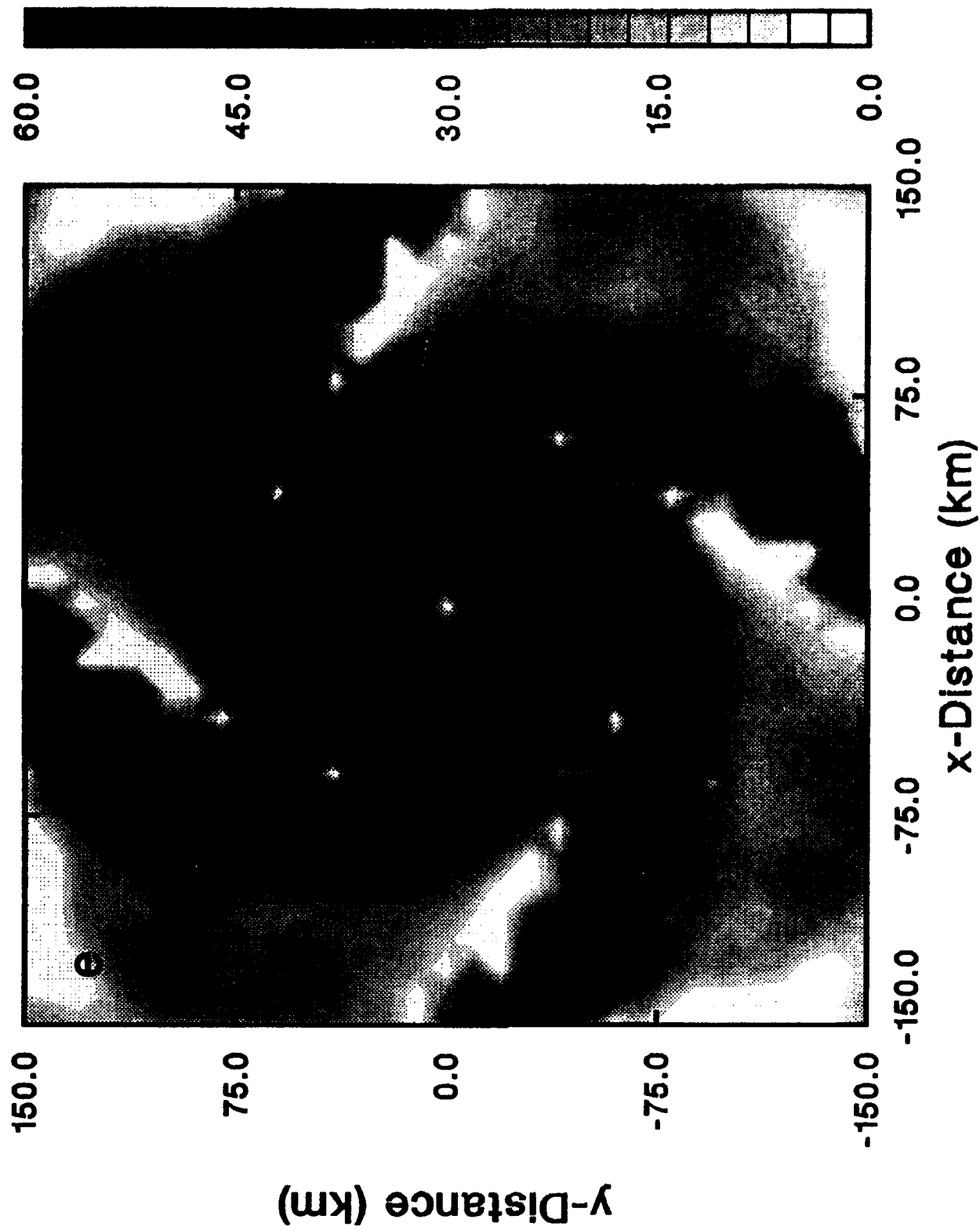


FIG. 7, continued.

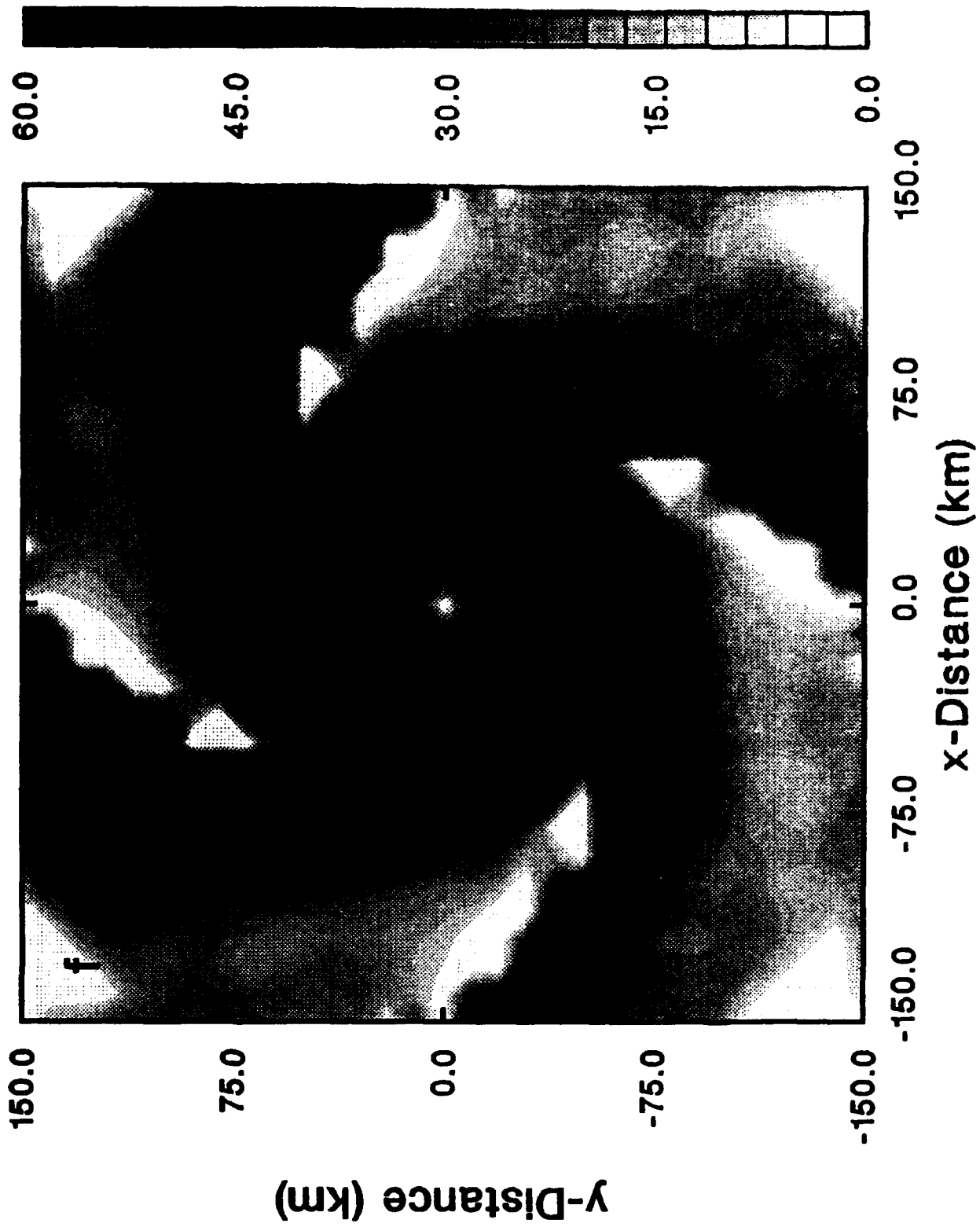


FIG. 7, continued.

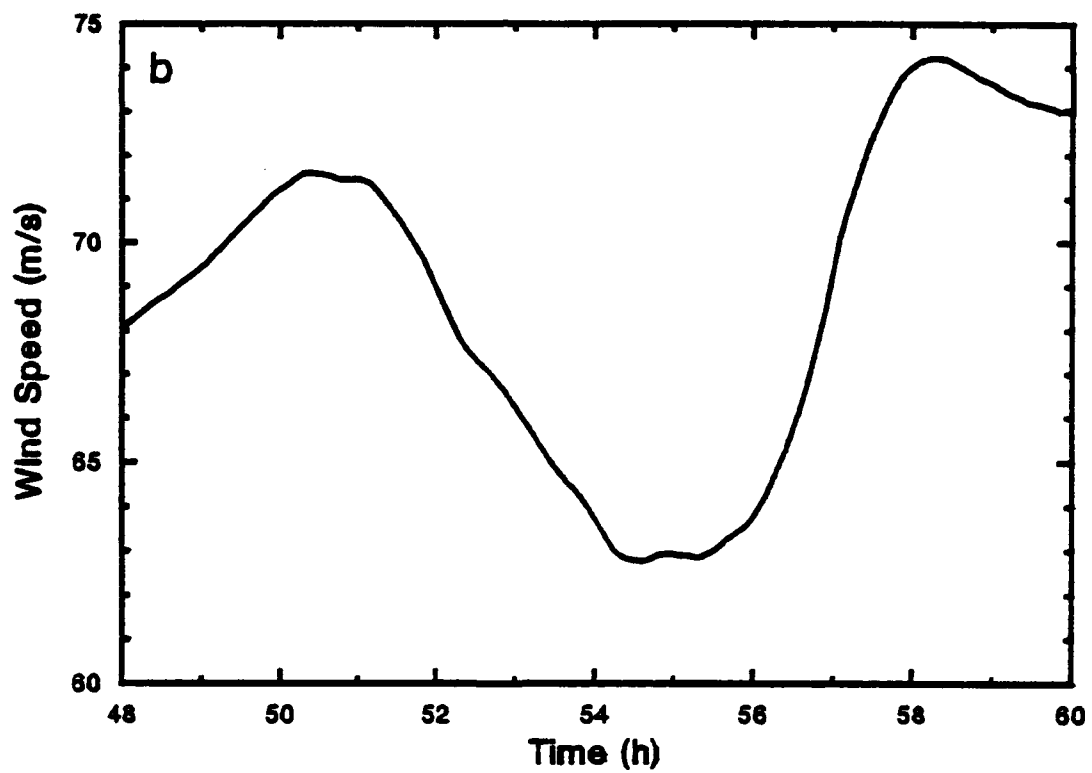
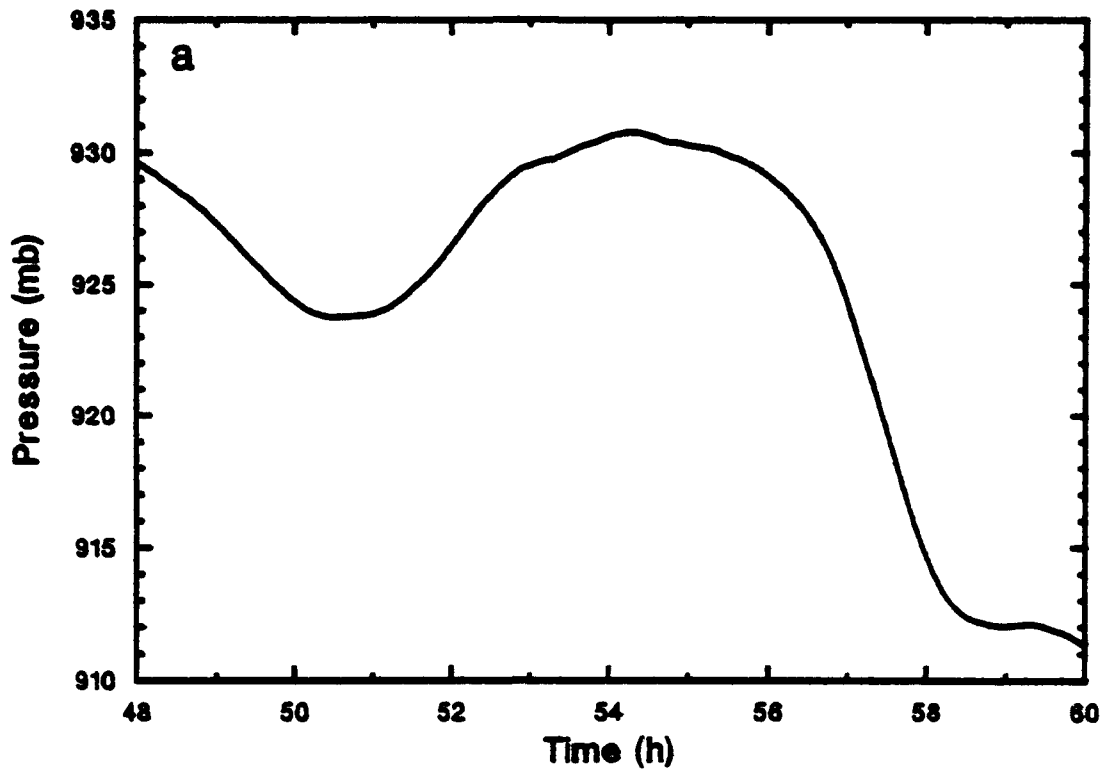


FIG. 8. (a) Central pressure (mb) forecast for EXP1 from 48-60 h. Values plotted every time step (30 s). (b) As in (a) except for maximum wind speed.

inner eye walls began to merge, did the central pressure begin to fall again with a corresponding increase in the maximum winds. Rapid intensification occurred during the one hour time period from 57 h to 58 h with the central pressure falling 9.6 mb from 924.3 mb to 914.7 mb and the maximum winds increasing from 69.3  $\text{m s}^{-1}$  to 74.0  $\text{m s}^{-1}$ . This intensification was short-lived, however, when the spiral bands started contracting inward toward the eye again by 60 h. As noted above, the radius of the eye increased from about 25 km to 40 km during the merging of the two concentric eye walls.

An examination of the overall deepening of the model storm highlights the overall effects of spiral bands on the storm development. It was noted above that the contraction of the spiral bands into an outer concentric ring that contracted inward resulted in a temporary weakening of the system. A re-examination of Fig. 6 shows that overall inflow and outflow of the storm is controlled significantly by the presence of the outer spiral bands at 48 h. However, at 84 h, when the system has just undergone a significant deepening of over 20 mb during the previous 12 h, there is noticeable decrease in spiral band convection (Fig. 7). The cross-sections of the radial components at 48 h and 84 h (Fig. 6) illustrate the effect that the spiral bands have on the storm circulation. At 48 h, the inflow is impeded into the eye by the convergence near 100 km radius. In addition, the strong outflow aloft appears to be associated most closely with the outer band of convection rather than the inner eye wall. It appears that the proximity of the outer band of convection is acting to retard the development and/or maintenance of the inner eye wall. However, at 84 h, without the presence of a significant outer eye wall, the low-level inflow is considerably stronger and the upper-level outflow is tied to the eye wall convection and proceeds undisturbed out to the edge of the forecast grid.

*c. Experiment 2: Coupled Simulation*

The second experiment (EXP2) performed with COAMPS is an 84 h coupled simulation of hurricane Gilbert using both the atmospheric and oceanic models. The atmospheric model was set up exactly as in EXP1. The ocean model also used a 61 x 61 Cartesian grid so that the grid points for the atmosphere and ocean were coincident. The ocean model used 20 vertical levels, with the spacing set at 5 m for the uppermost layer and each successively lower layer being 1 m more in depth. Therefore, the total ocean depth was 290 m. The large time step for the ocean model was set to 1200 s and the small time step was 30 s. The coupling was achieved by integrating the atmospheric model first for 40 time steps, i.e., for one ocean time step. The average surface fluxes of heat, momentum and moisture, and the precipitation over these 40 time steps were then used as the upper boundary conditions for the ocean subgrid scale mixing processes.

The atmosphere was initialized with a Rankine vortex exactly as described above for EXP1. The ocean model was assumed to be at rest initially, and the GDEM profiles of temperature and salinity (Fig. 9) that were used to obtain the SST in EXP1 were used in EXP2 to define the homogeneous vertical thermodynamic structure of the ocean. Therefore, the starting values for the atmospheric forecast in EXP2 were exactly those used in EXP1. However, in EXP2, the SST (i.e., the temperature of the top layer of the ocean) was allowed to vary, with the changes being due to the influence of the surface energy exchanges and precipitation.

The COAMPS forecasts for the central pressure and the maximum wind speed for EXP1 and EXP2 are presented in Fig. 10. As in EXP1, the coupled simulation requires about 24 h for the initial spin-up before the hurricane starts to deepen. Through the first 60 h of the simulations, EXP2 tends to be somewhat weaker, with a central pressure difference between the two simulations of generally 5-10 mb

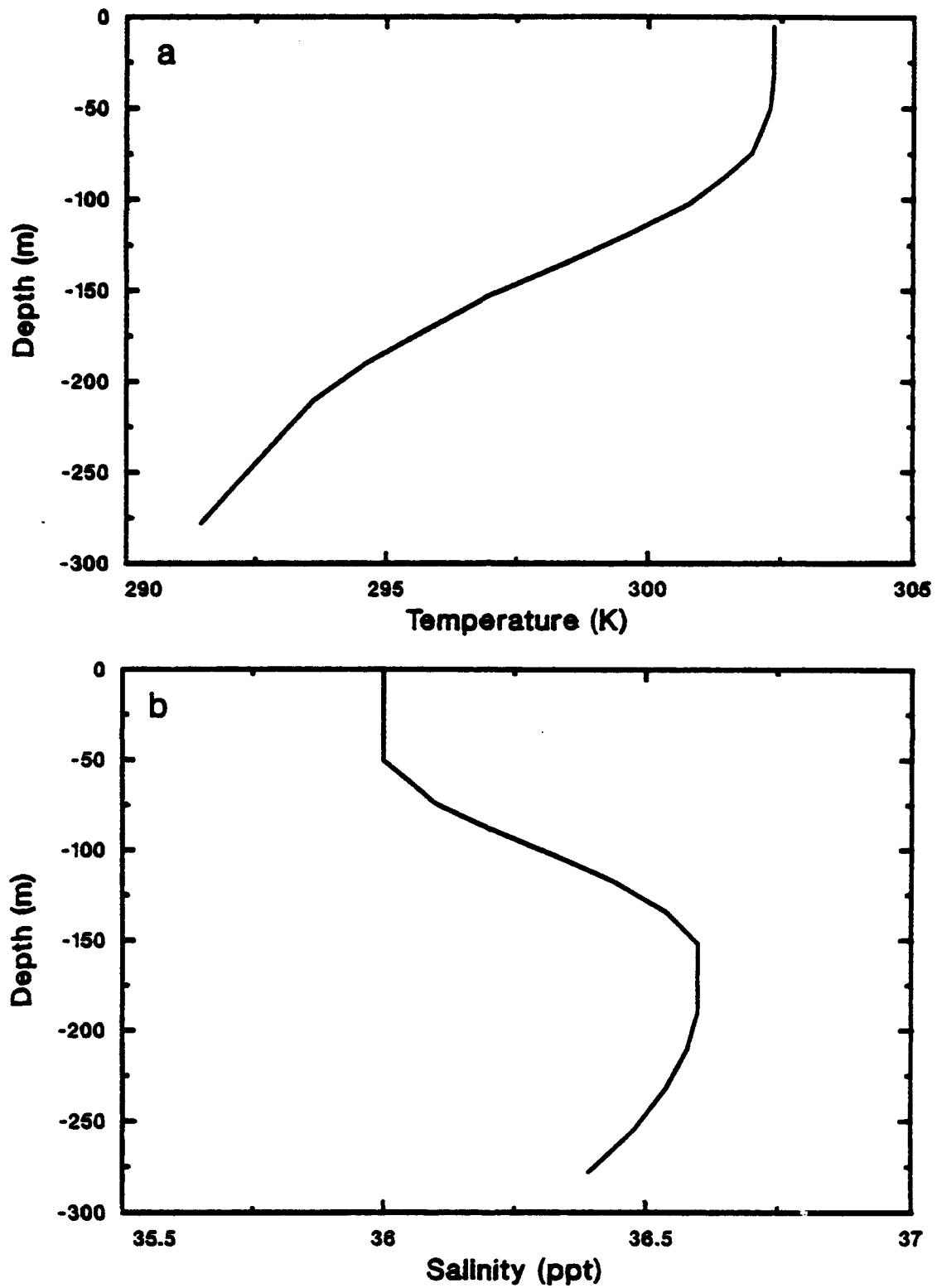


FIG. 9. (a) Initial ocean temperature (K) profile for EXP2. (b) As in (a) except for salinity (ppt).

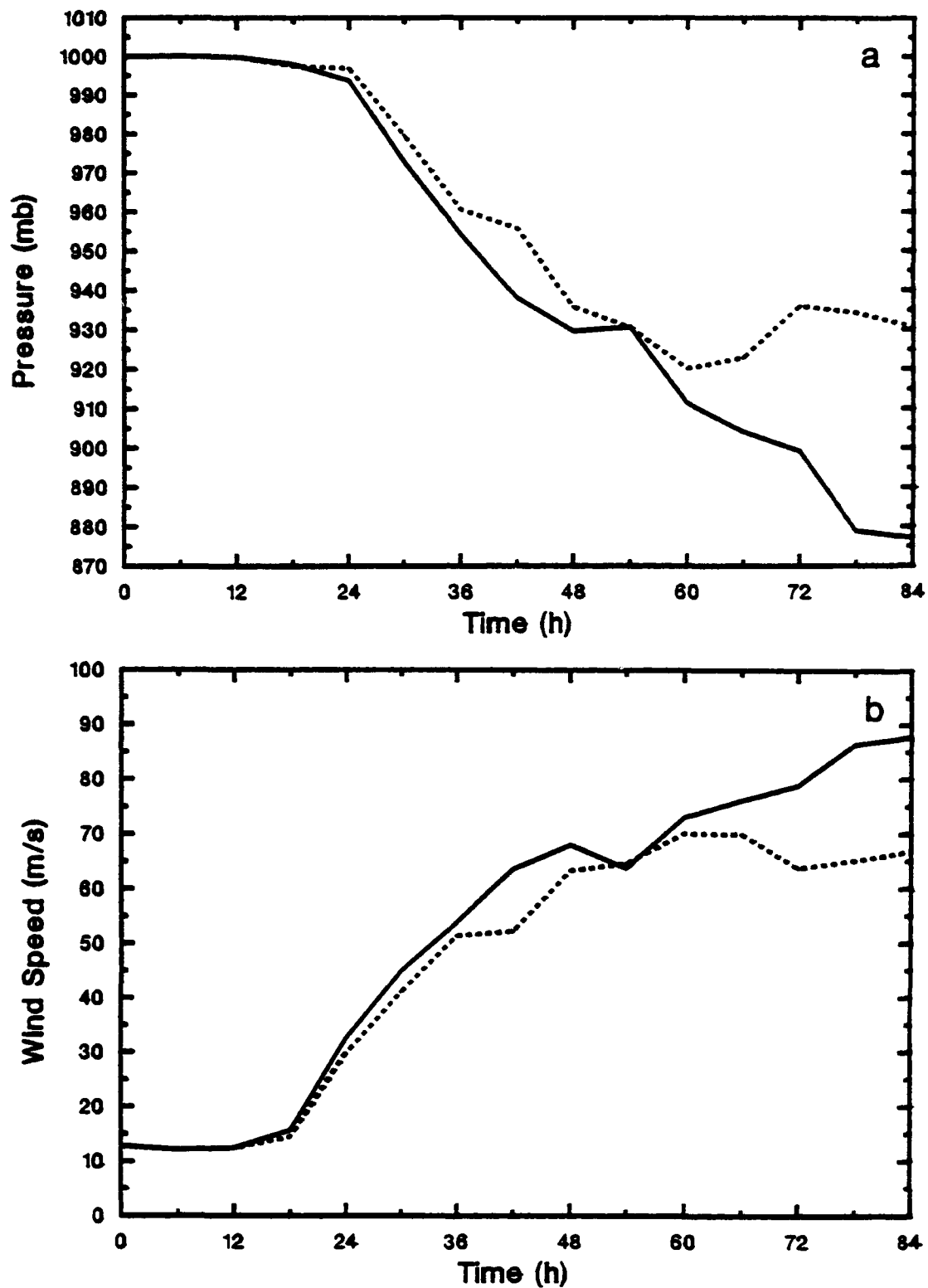


FIG. 10. (a) COAMPS central pressure (mb) forecast for EXP1 (solid) and EXP2 (dash). (b) As in (a) except for maximum wind speed ( $\text{m s}^{-1}$ ).

and a maximum wind speed difference of  $2-10 \text{ m s}^{-1}$  from 24 h to 60 h. After 60 h, more significant differences are found. While in the fixed SST experiment the central pressure dropped from 912 mb to 874 mb after 60 h, in EXP2 the central pressure rose from 920 mb to 936 mb at 72 h before it intensified somewhat to 930 mb by 84 h. At 84 h, the difference in central pressure between EXP1 and EXP2 is 53.5 mb. Similar tendencies are found in the maximum wind speeds with a difference of  $21 \text{ m s}^{-1}$  at 84 h.

The reason for the behavior of EXP2 relative to EXP1 can be seen by looking at the SST change near the center of the storm (at 10 km radius) in EXP2 (Fig. 11). During the first 42 h, the SST exhibited cooling of less than  $0.5^\circ\text{C}$ . After 42 h, the cooling increased dramatically, with SST changes of  $-5.7^\circ\text{C}$  by 60 h and  $-8.0^\circ\text{C}$  at 84 h. At outer radii, the SST cooling was generally no less than  $-0.5^\circ\text{C}$ . From these SST changes, it is understandable that there are relatively small differences between the strength of the hurricane in EXP1 and EXP2 during the first 42 h. However, since the SST dropped over  $5^\circ\text{C}$  from 42 h to 60 h with no significant weakening occurring in the strength of the hurricane in EXP2 until after 60 h, it appears that there is a time lag on the order of 12 h between strong surface cooling near the eye wall and corresponding changes in the storm intensity. This result is similar to that found by Anthes and Chang (1978).

The distribution of the SST changes for EXP2 over the entire domain at 84 h is given in Fig. 12. The maximum change of  $8.3^\circ\text{C}$  is found about 20 km from the storm center. Cooling of up to  $3^\circ\text{C}$  extends to a radius of about 80 km while much of the remainder of the domain exhibits an SST reduction of generally about  $0.5^\circ\text{C}$ . Some enhanced cooling (of up to  $1.2^\circ\text{C}$ ) is noted under the location of the spiral bands. This can be traced to the cooling of the near-surface air temperature from the evaporation of raindrops, resulting in a slight increase in the surface sensible

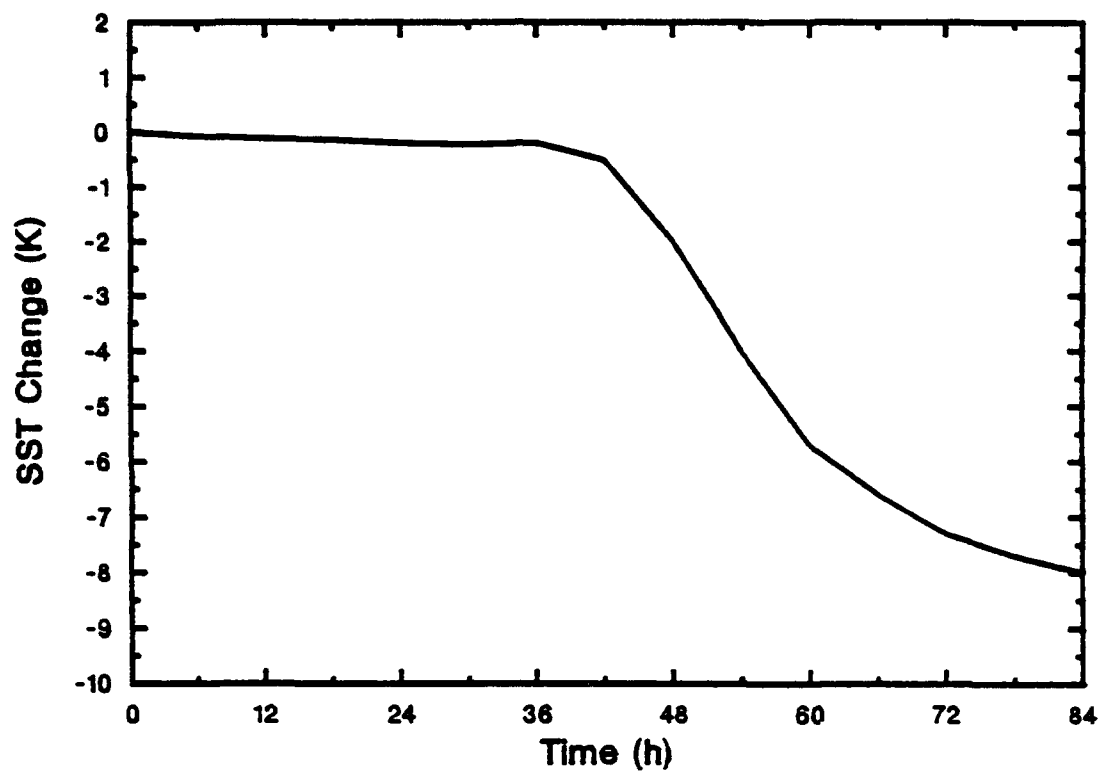


FIG. 11. SST change (K) from 0-84 h 10 km from center of the storm in EXP2.

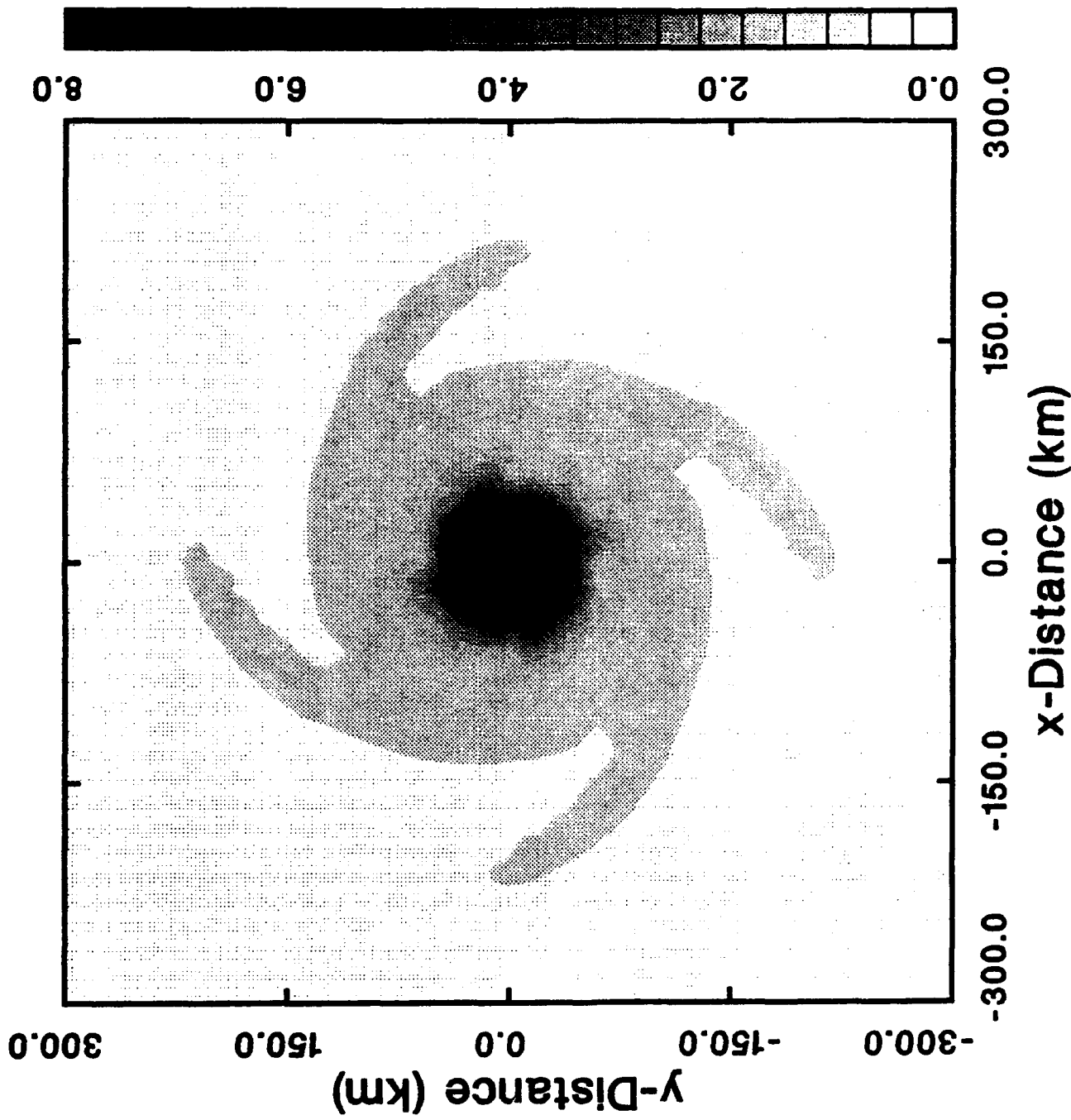


FIG. 12. SST change (K) at 84 h for the full forecast domain in EXP2.

heat flux (not shown).

Cross-sections illustrating the time evolution of the ocean temperature change are given in Fig. 13. At 48 h, the maximum cooling of about  $4^{\circ}\text{C}$  is found at a depth of 62 m, near the initial position of the thermocline. The cooling proceeds so that at 84 h, the maximum cooling of  $-9.5^{\circ}\text{C}$  is also found at a depth of 62 m with nearly all changes of more than  $2.0^{\circ}\text{C}$  confined to within 50 km of the center of the storm. At the surface, the maximum cooling of  $-8.3^{\circ}\text{C}$  is found 20 km from the storm center with  $-7.3^{\circ}\text{C}$  cooling directly under the eye of the hurricane.

The ocean current speeds and direction induced by the hurricane at 84 h are shown in Fig. 14. Maximum speeds of  $3.1\text{ m s}^{-1}$  are found 30 km from the eye, directly under the surface maximum winds. A strong pattern of divergence exists within the cyclonic circulation within a 50 km radius of the eye. This divergence leads to upwelling in the ocean, with maximum vertical velocities as high as  $0.32\text{ cm s}^{-1}$ . This is about twice as large as the value found by Chang and Anthes (1979) for a storm moving at  $5\text{ m s}^{-1}$ . Rather than occurring directly under the eye, the strongest vertical velocity occurred at a radius of 10-20 km with weaker upward motion under the eye (not shown).

The salinity of the ocean at 84 h in the uppermost layer of the ocean is given in Fig. 15. Inside a radius of about 50 km, the salinity has increased from an initial value of 36.0 ppt to 36.6 ppt. This is a result of the combination of vertical mixing and upwelling bringing larger sub-surface values to the surface and large latent heat fluxes ( $> 3000\text{ W m}^{-2}$ ) inside the radius of maximum winds resulting in a loss of fresh water from the top ocean model layer. Another area of change is found under the spiral bands where the salinity decreased from 36.0 ppt to 35.1 ppt over the 84 h of the simulation. It was shown earlier that these areas also exhibited a decrease in SST. The decrease in salinity here is due to the imbalance between the relatively

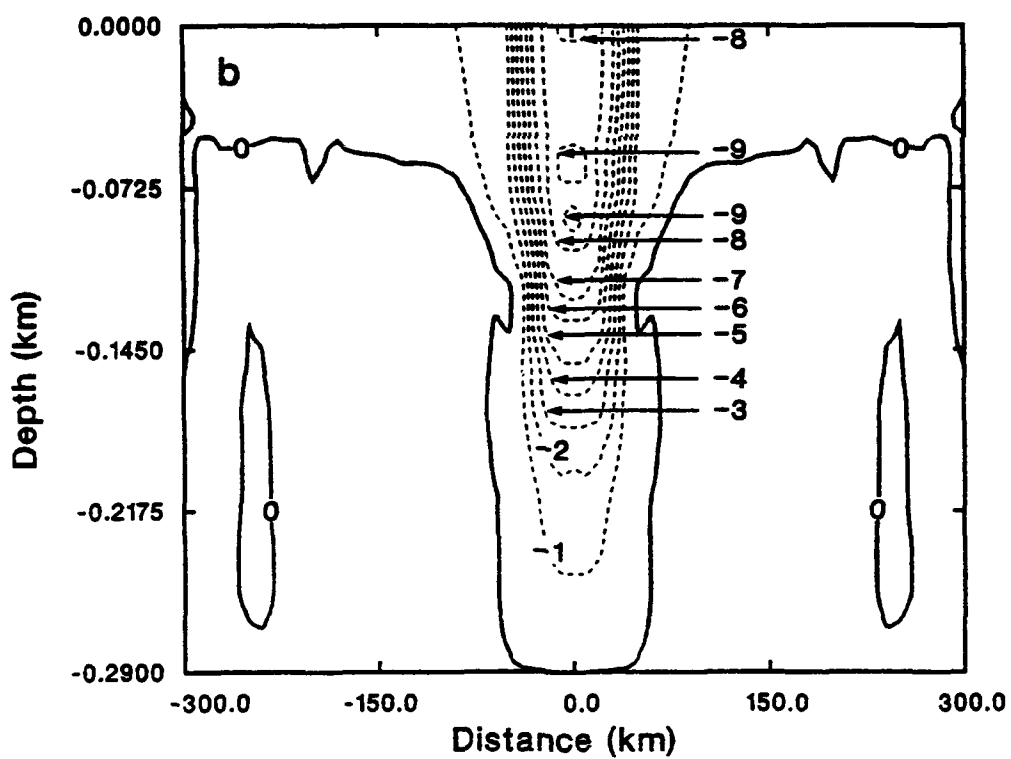
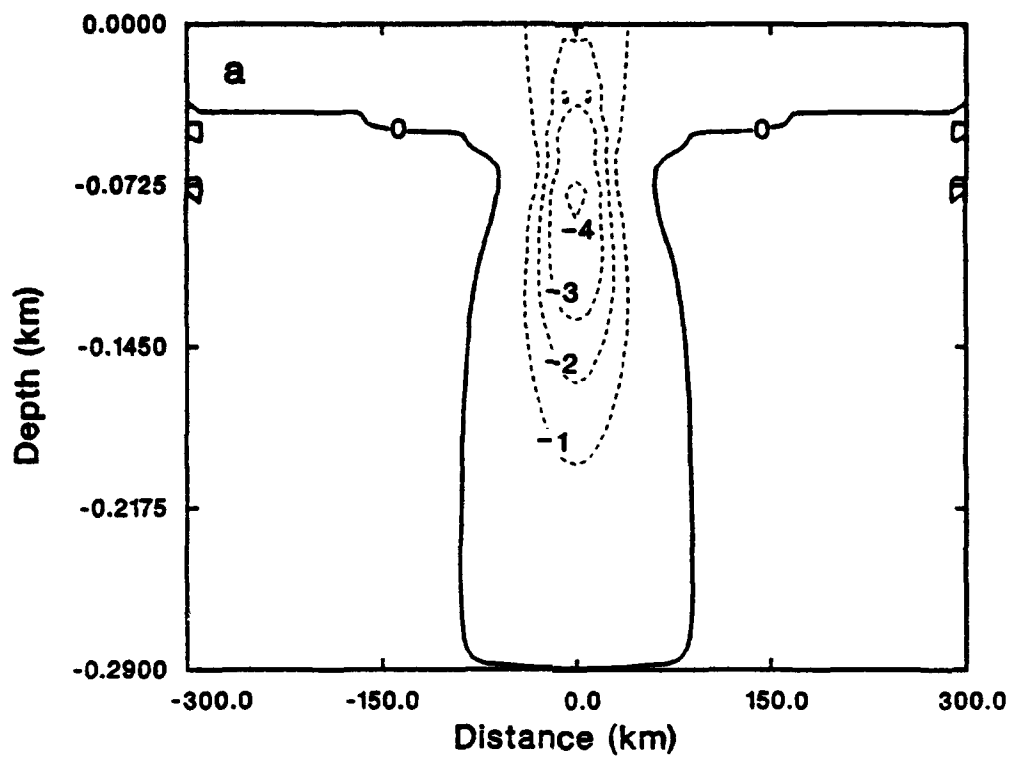


FIG. 13. East-west vertical cross-sections of the ocean temperature change (K) for EXP2 at (a) 48 h and (b) 84 h. Contour interval is 1 K.

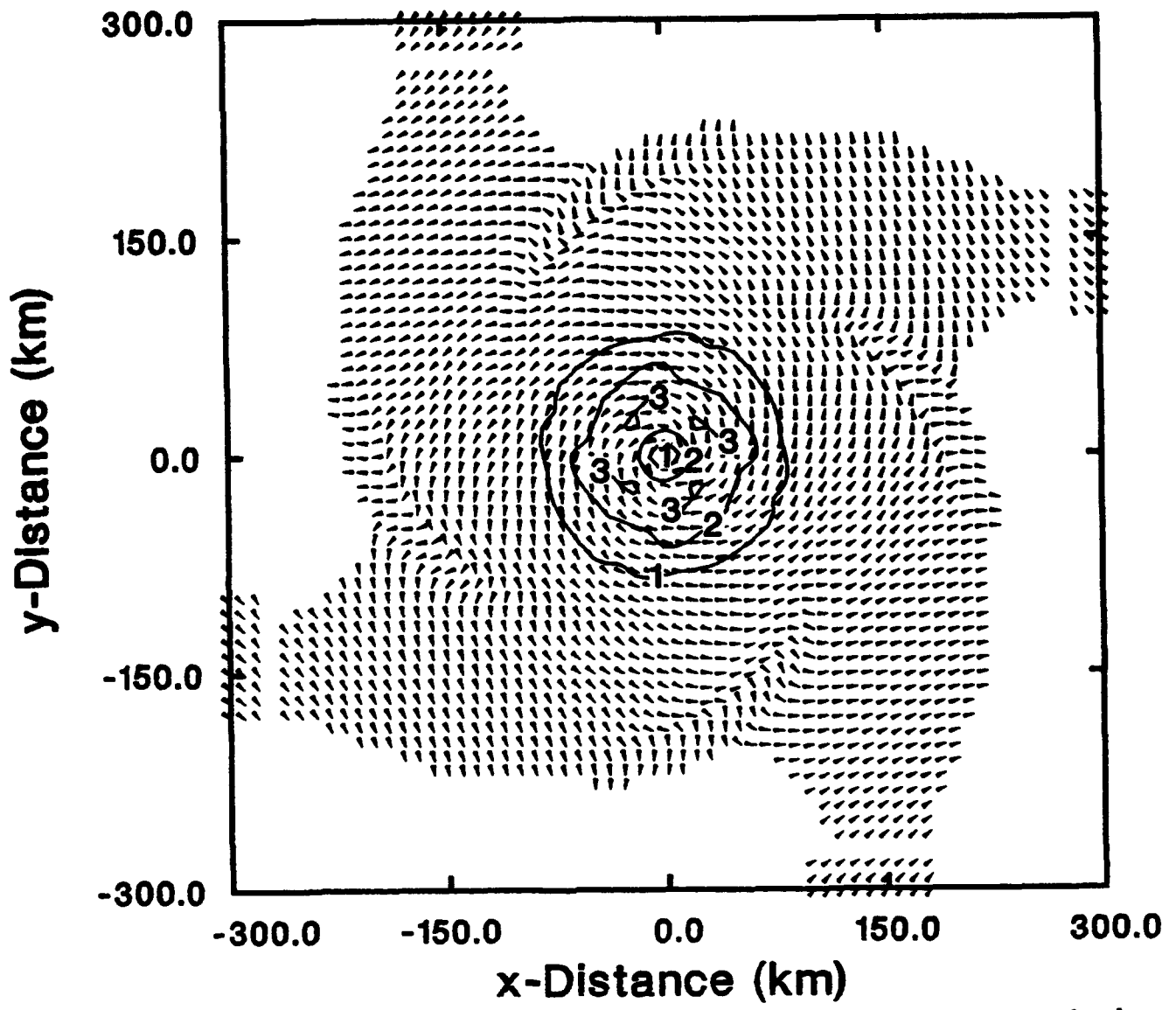


FIG. 14. 84 h EXP2 forecast of ocean current speed and direction at 2.5 m depth. Contour interval is  $1 \text{ m s}^{-1}$ .

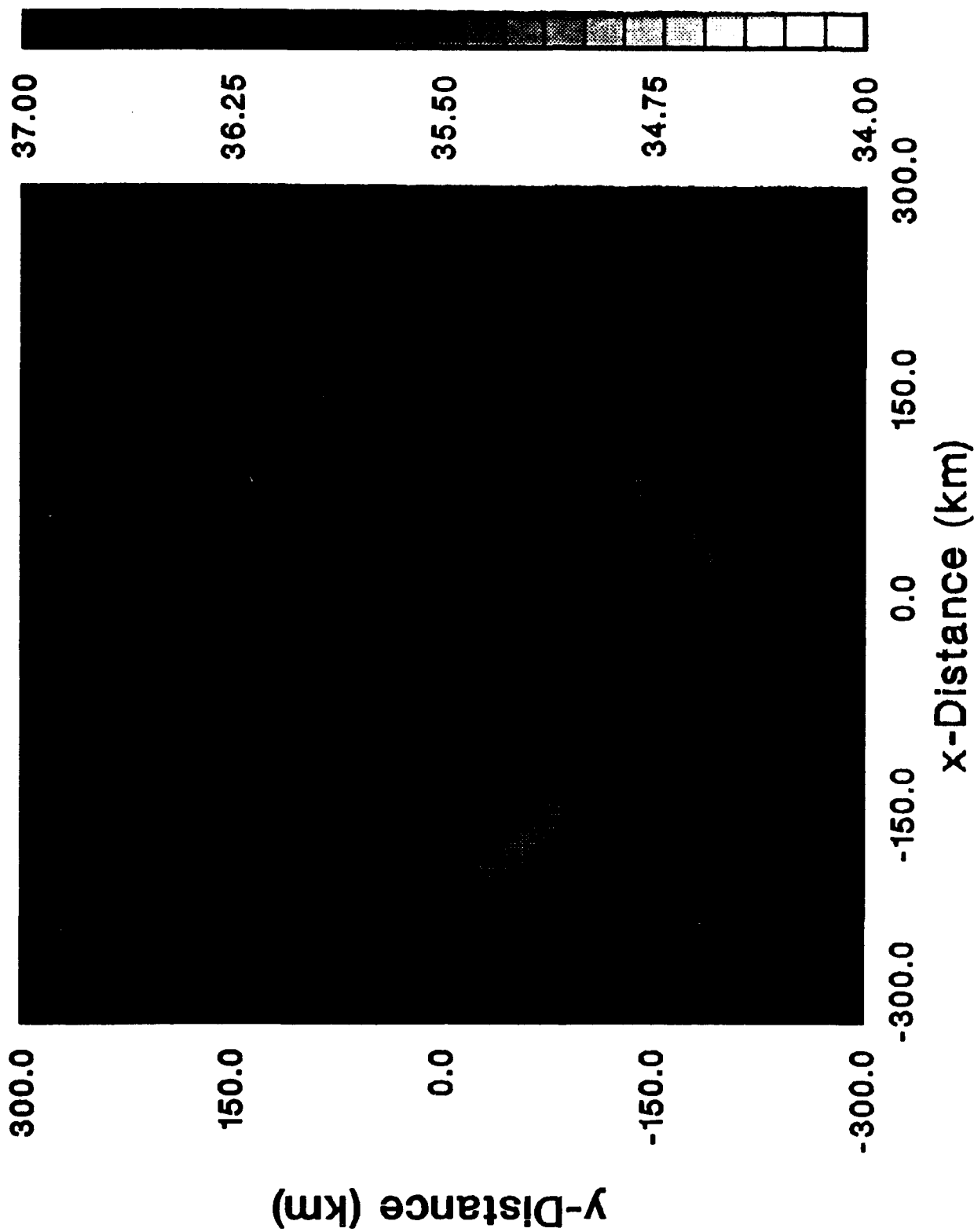
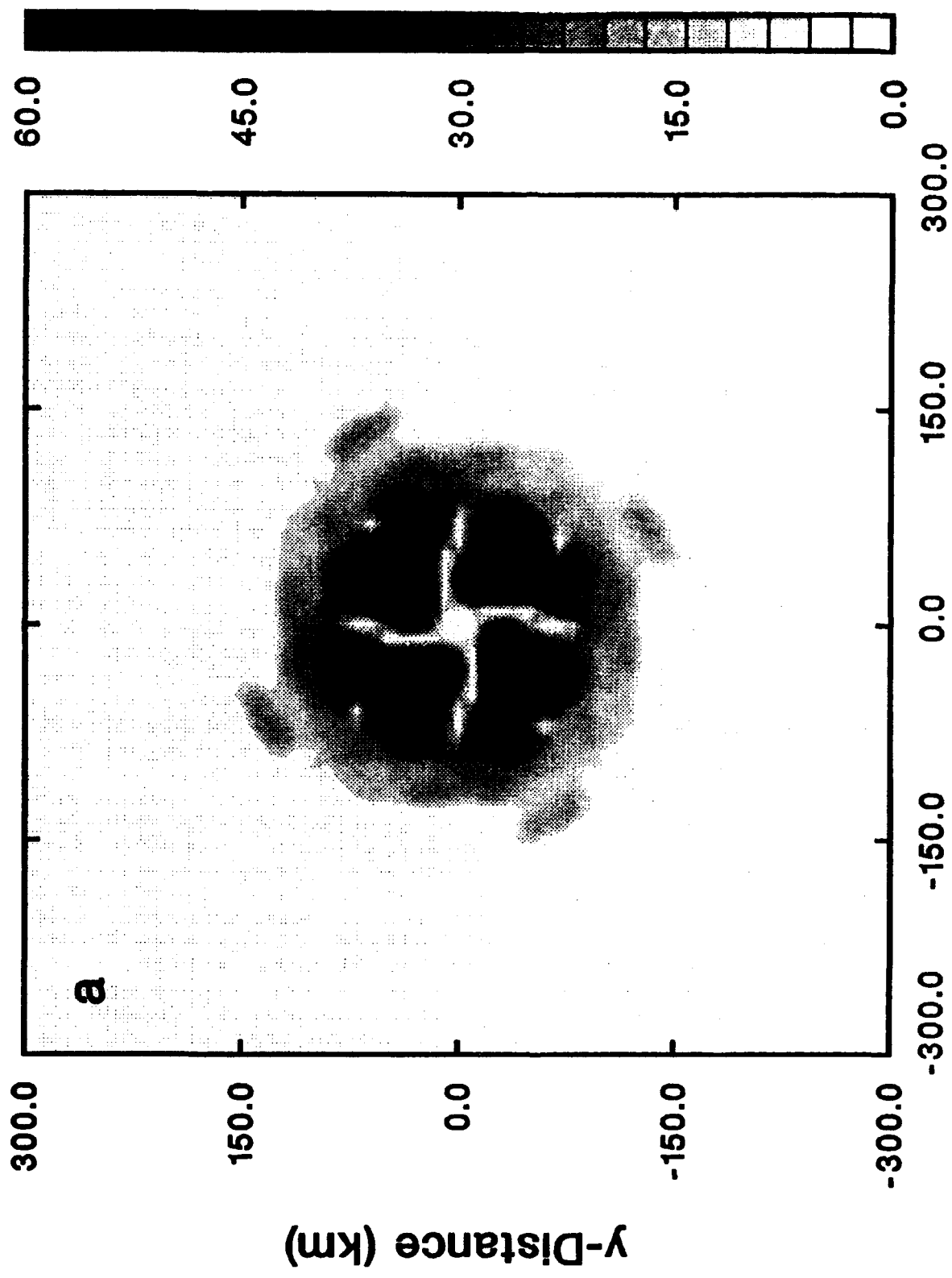


FIG. 15. 84 h EXP2 forecast of salinity (ppt) at 2.5 m depth.

weak latent heat flux in this area ( $250 \text{ W m}^{-2}$ ) and the total precipitation over 84 h.

The SST changes of over  $8^\circ\text{C}$  reported here are somewhat larger than the  $5\text{-}6^\circ\text{C}$  reduction actually observed for Hurricane Gilbert (Shay et al. 1991). This can be partially explained by the fact that in EXP2, the model storm remained stationary for all 84 h of the simulation and therefore, all the mixing and upwelling responsible for the SST reduction remained concentrated over the same area. In reality, Gilbert moved westward to west-northwestward at a speed of about  $7 \text{ m s}^{-1}$  and the SST cooling processes were isolated for a given area for a much shorter period of time. These findings indicate that SST cooling may have little effect on hurricane strength for storms with a movement of as little as  $1\text{-}2 \text{ m s}^{-1}$ . Since the storm is moving it will continuously be entering areas of undisturbed SST, unless of course, the storm has looped back over a previous position or another storm's track. Also, since there appears to be a time lag of perhaps 12 h between the strong SST cooling and a response to the hurricane strength, a forward speed of  $1\text{-}2 \text{ m s}^{-1}$  will enable the eye wall of the storm to move away from the cooled area before it can have an impact on the eye wall.

An examination of model-generated radar reflectivities for EXP2 (Fig. 16) compared to those described earlier for EXP1 (Fig. 4) illustrate the differences in the structure of the hurricane between the two simulations. In both EXP1 and EXP2, similar patterns are observed up to 48 h. The convection, initially at radii from 50-100 km, collapses inward to form an eye wall with maximum reflectivities within 20-40 km of the center of the storm. Spiral bands are evident in both simulations by 48 h, somewhat stronger in EXP1, presumably since the SST has decreased as much as  $0.5^\circ\text{C}$  in EXP2 over much of the domain. After 48 h, significant differences are noted with the eye wall structure. First, at 60 h in



**x-Distance (km)**  
 FIG. 16. As in Fig. 4 except for EXP2.

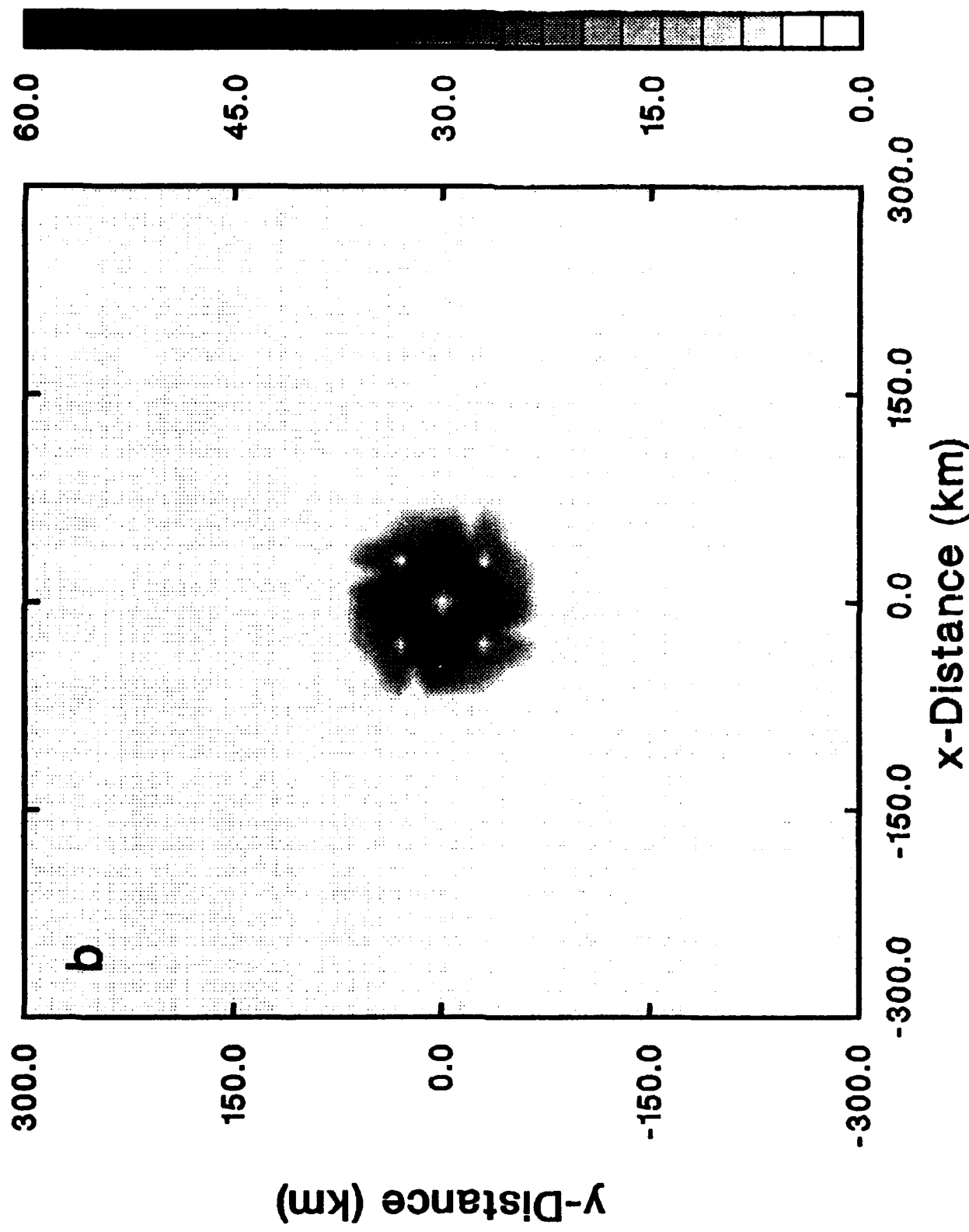


FIG. 16, continued.

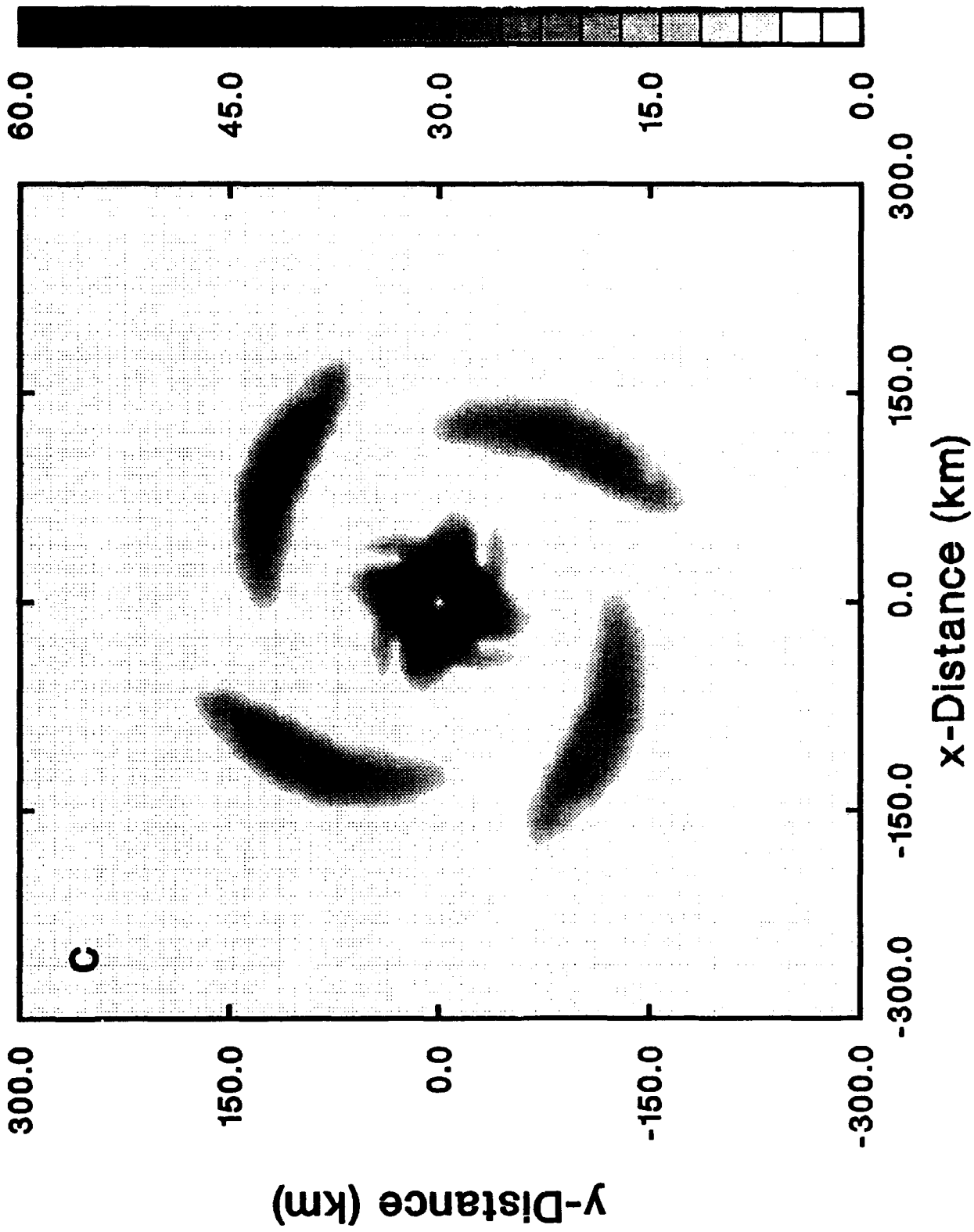


FIG. 16, continued.

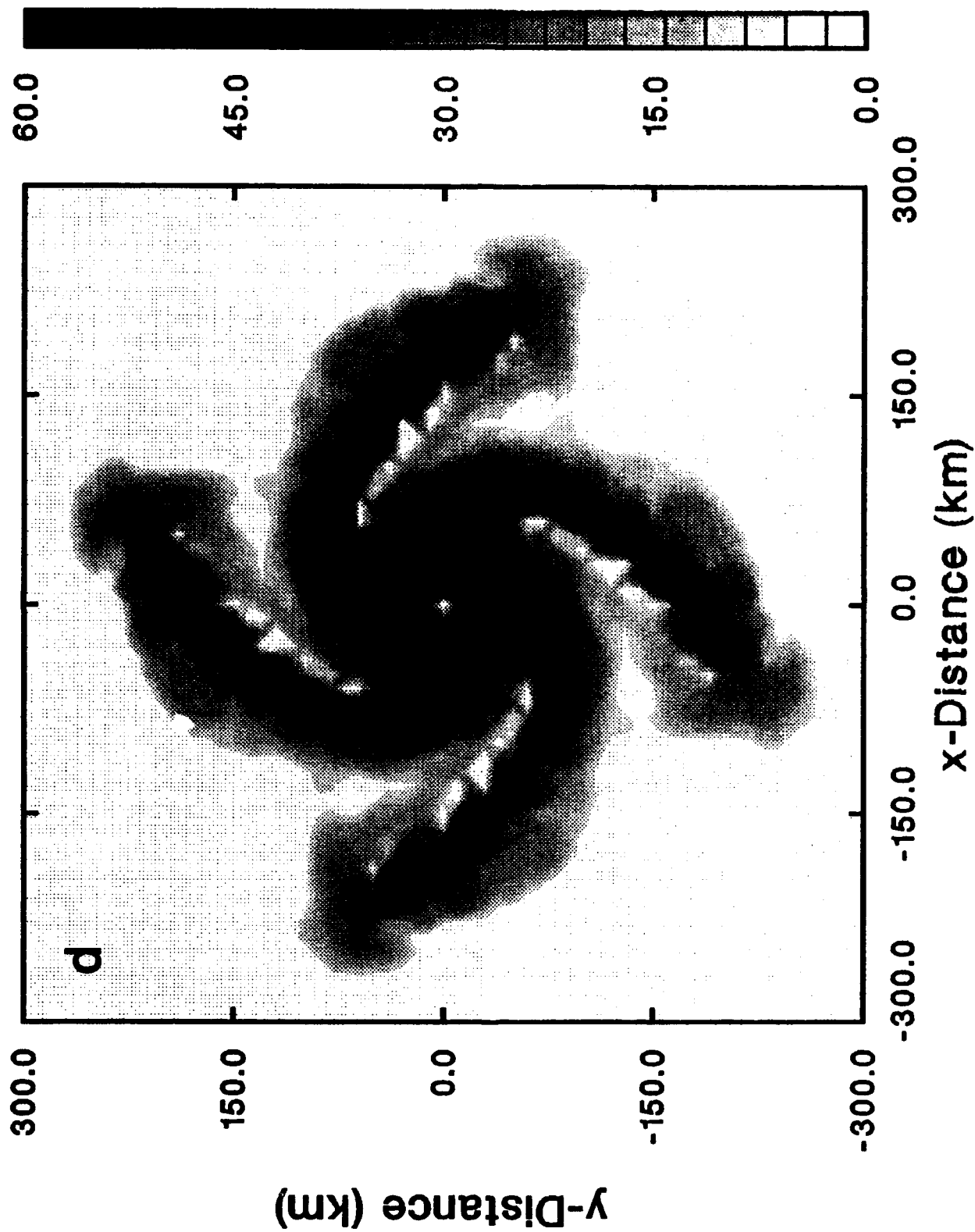


FIG. 16, continued.

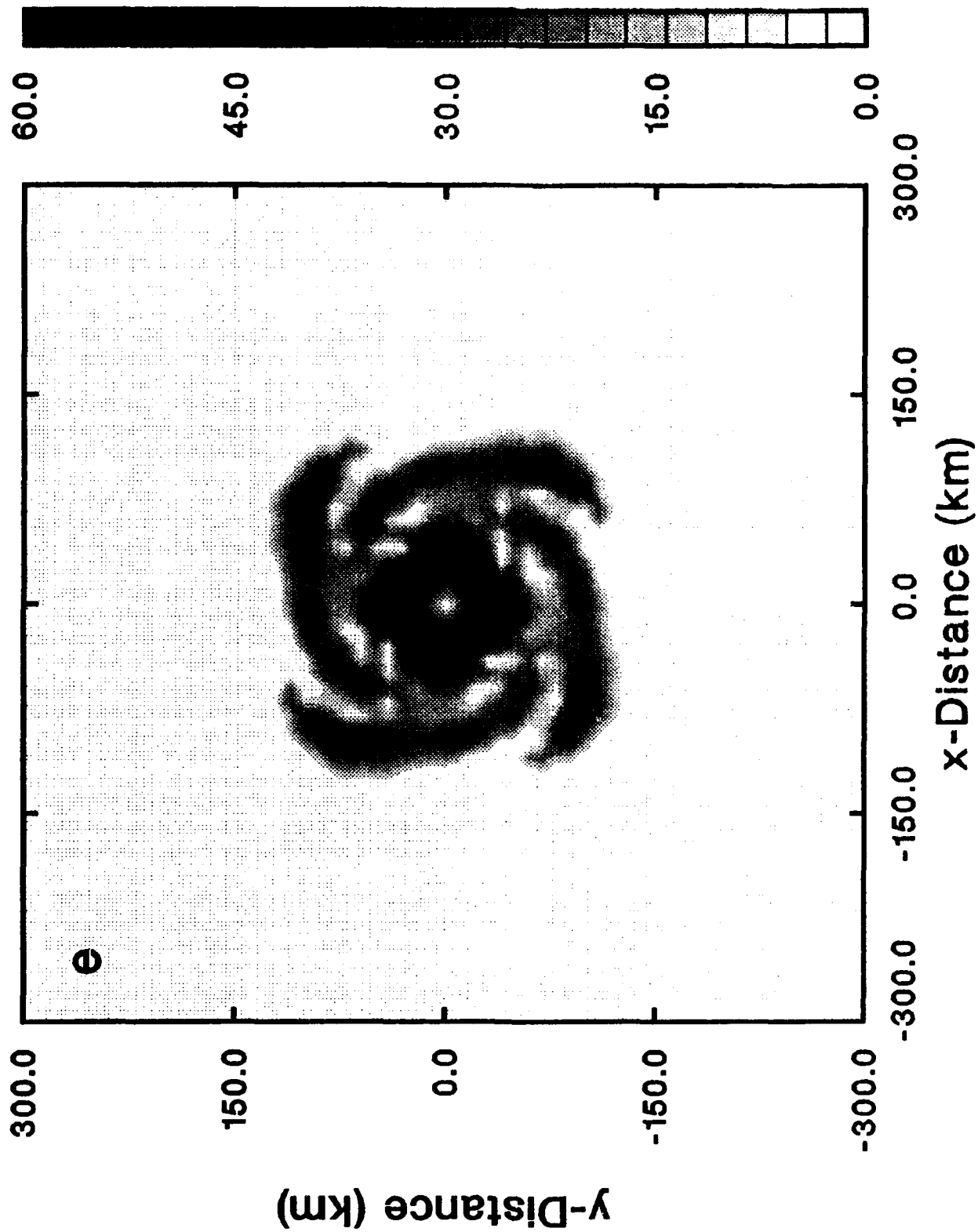


FIG. 16, continued.

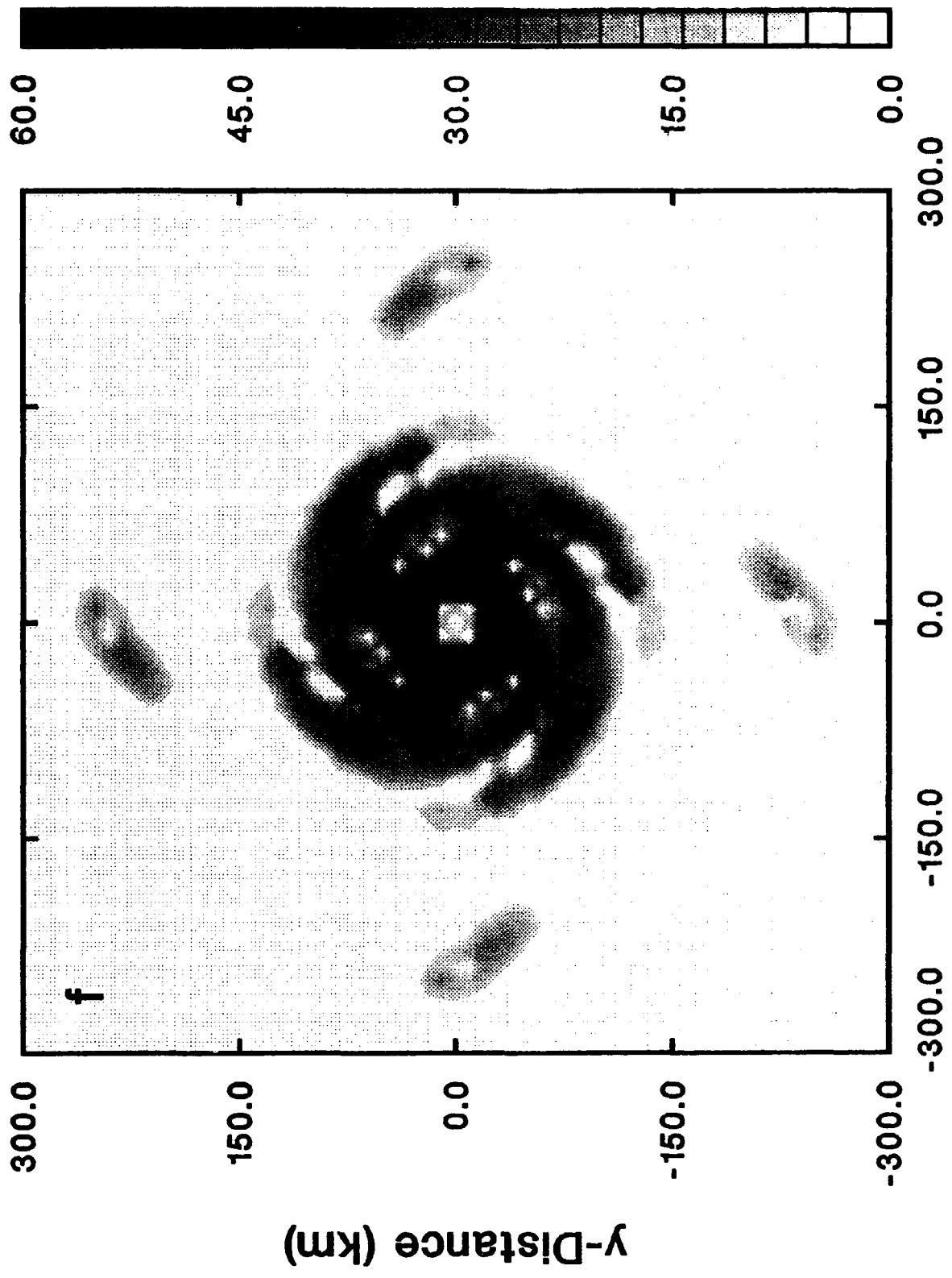


FIG. 16, continued.

EXP2, it is evident that the eye wall is starting to expand in response to the SST cooling. Also, the strength of the echo at radii from 10-20 km is weaker in EXP2. At 72 h and 84 h, the echo-free region associated with the eye is noticeably larger in EXP2. At 84 h, at the time of the maximum SST reduction, EXP2 exhibits an eye wall that is thinner and weaker than that in EXP1. In spite of the strong SST cooling near the center of the circulation, the overall structure of EXP2, outside a radius of approximately 50 km, remains the same with the spiral bands continuing to feed convective cells inward toward the eye wall. The significant change due to the SST cooling is with the strength and position of the eye wall.

The differences in the EXP1 and EXP2 tangential velocities at 48 and 84 h can be seen by examining Fig. 17. At 48 h, both EXP1 and EXP2 exhibit maximum tangential velocities of  $62 \text{ m s}^{-1}$  at a radius of 20 km. The tangential wind profiles are nearly constant with height up to 5 km with the winds decreasing above this level. By 84 h, the most significant differences are found in the eye wall region. Besides EXP2 exhibiting a maximum tangential wind of  $67 \text{ m s}^{-1}$  as opposed to  $85 \text{ m s}^{-1}$  in EXP1, the radius of the maximum wind in EXP2 is 10 km larger than in EXP1. Also, the gradient of the tangential wind from the maximum to the eye is significantly weaker in EXP2. At radii beyond about 50 km, only small differences exist in the tangential wind profiles. This indicates that while the intensities (based on the maximum wind speed) of the EXP1 and EXP2 storms are different, their strengths (based on winds outside the radius of maximum winds) appear to be quite similar. This suggests that modification of the SST by a tropical cyclone may have little or no effect on the subsequent track of the storm due to any forced changes in structure since the SST changes will only affect the intensity and not the overall strength of the storm (Holland 1984, DeMaria 1985).

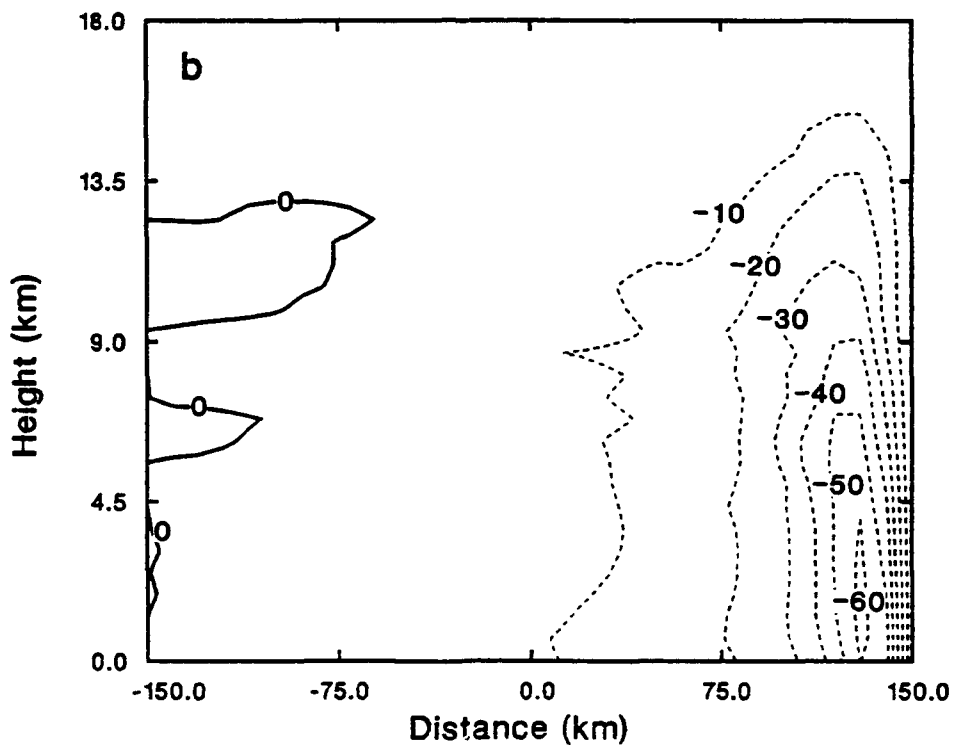
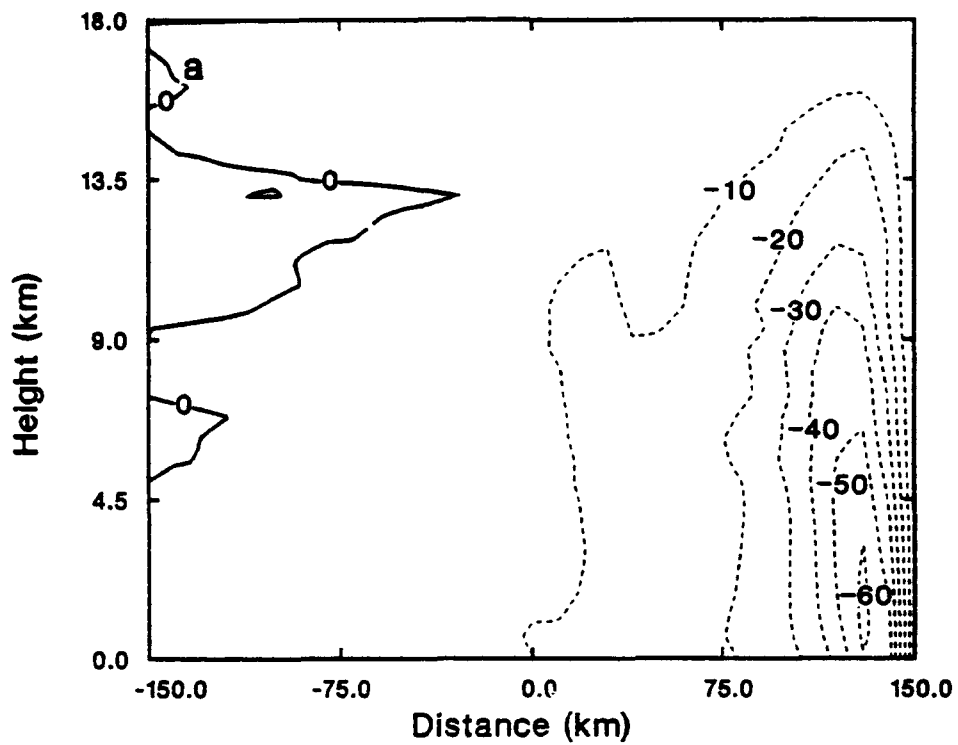


FIG. 17. East-west vertical cross-sections of tangential velocity ( $\text{m s}^{-1}$ ) taken from the left boundary to the center of the grid for (a) EXP1 at 48 h, (b) EXP2 at 48 h, (c) EXP1 at 84 h, and (d) EXP2 at 84 h. Contour interval is  $10 \text{ m s}^{-1}$ .

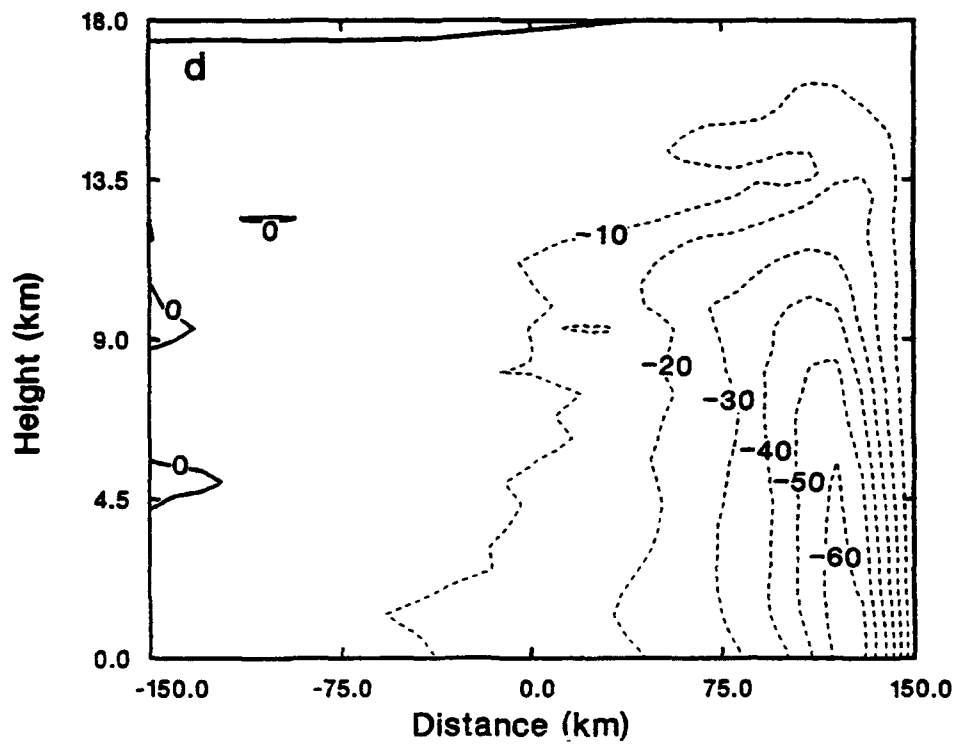
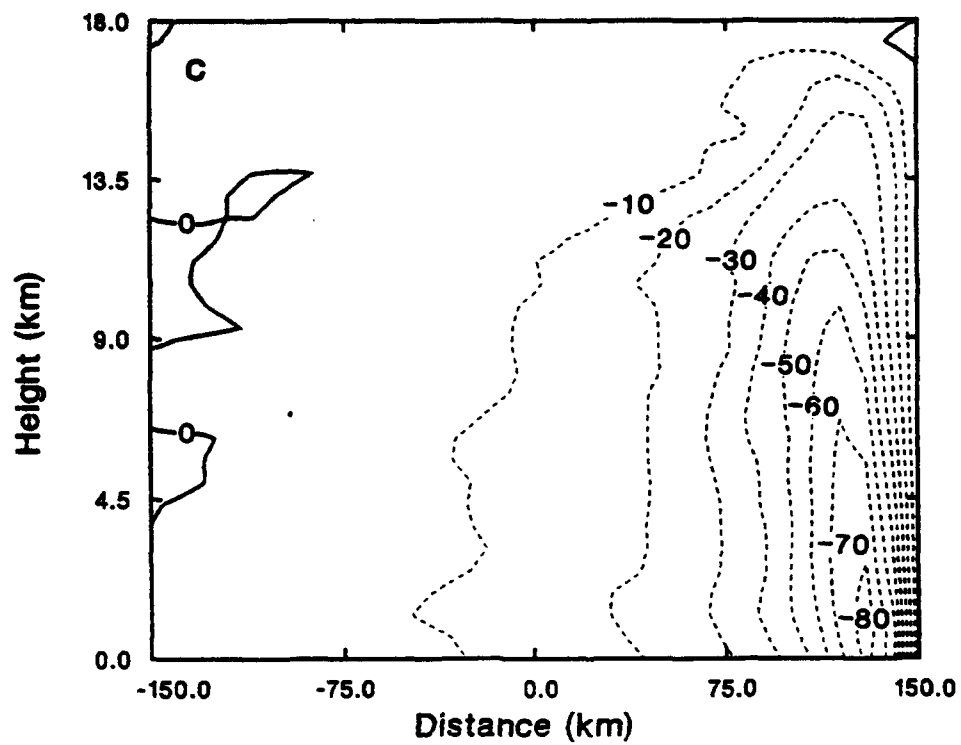


FIG. 17, continued.

## 5. Conclusion

A nonhydrostatic, compressible atmospheric model has been coupled to a hydrostatic ocean model. This coupled ocean/atmosphere mesoscale prediction system (COAMPS) is flexible in that it is written in standard FORTRAN 77 code and the number of grid points and the resolution of the grid can be set by the user for all three dimensions. The models in COAMPS can be run simultaneously for fully coupled simulations or either one can be run on a stand-alone basis for an atmospheric or oceanic simulation. Coupling of the fluxes across the air-water interface is accomplished by averaging the atmospheric fluxes for all time steps within one ocean time step. The coupling includes exchanges of heat, momentum and moisture plus the effects of precipitation on ocean salinity. COAMPS currently does not include radiation, the effects of the precipitation temperature on the ocean temperature, the evaporation of ocean spray, or the effect of ocean waves on the surface drag.

The atmospheric model has been designed for mesoscale and large-scale eddy simulations. An explicit moist physics routine allows for the prediction of water vapor, cloud water, raindrops, ice crystals and snowflakes. A 1-1/2 order subgrid scale closure model is used to predict the turbulent kinetic energy. A time-splitting technique is used for efficiency in handling the sound and gravity waves.

The ocean model uses a time-splitting scheme to separate the barotropic and baroclinic terms. Predictive equations for  $u$ -,  $v$ -, temperature, salinity and the height of the free surface are included. The model uses a Richardson number based diagnostic equation for the subgrid scale mixing terms.

Two idealized case studies of Hurricane Gilbert have been performed using COAMPS. In the first simulation, only the atmospheric model was used, assuming a steady-state (fixed) SST. In the second simulation, both the atmospheric and

ocean models were used, allowing the ocean, and therefore, the SST, to respond to the surface fluxes. In both simulations, the hurricane remained in the center of the grid because of the absence of a mean flow and use of an f-plane. The initial thermodynamic state for the atmosphere in both simulations was based on an individual sounding representative of the environment near Gilbert. A Rankine vortex was used to initialize the hurricane circulation. A climatological temperature and salinity profile was used to initialize the ocean.

For the fixed SST simulation, the model generated hurricane showed strong resemblance to many features observed in hurricanes. The central pressure fell to 874 mb, with a deepening rate similar to that found in Hurricane Gilbert. The model storm developed an eye wall with a radius of 20-30 km which was characterized by upward motion with maximum values of up to  $6 \text{ m s}^{-1}$ . Subsidence in the eye was as strong as  $-1 \text{ m s}^{-1}$ . After an initial spin-up period, the model storm developed spiral bands, consisting of convective cells which propagated in toward the eye wall. The spiral bands would occasionally close off into an outer eye wall which would contract in while the inner eye wall weakened. During this stage, the storm would remain at the same intensity or weaken slowly. Eventually, the two eye walls would merge, and in one instance, this was associated with a central pressure drop of nearly 10 mb in one hour.

In the coupled simulation, the intensity of the hurricane was hindered by strong cooling of the SST forced by the hurricane circulation. Differences between the non-coupled and coupled simulations were less than 10 mb for the first 42 h of the simulations while the largest SST anomaly was no more than  $0.5^\circ\text{C}$ . The lowest pressure reached in the coupled simulation however, was 914 mb, which occurred at about 60 h into the simulation, or about 12 h after the SST began to cool rapidly near the center of the storm. After 60 h, the coupled simulation

exhibited a weakening of approximately 15 mb. After 84 h of integration, a SST anomaly of 8°C was found in the circular area bounded by the radius of maximum winds. The central pressure of the non-coupled and the coupled cases differed by 54 mb. Some enhanced cooling, of up to 0.75°C, was found to occur under the spiral bands that formed outside the eye wall. Under these bands, the near-surface air temperature was found to be lower than the surrounding air due to evaporation of raindrops. This led to enhanced surface sensible heat fluxes and stronger SST cooling. Finally, it was found that although the SST anomaly of 8°C altered the intensity of the system near the eye wall, it had little or no effect on the outer storm strength.

The following conclusions are made based on these simulations. First, the feedback of ocean cooling on the hurricane should be minimal in real situations in which the storm has a translation speed of at least 1-2 m s<sup>-1</sup>. This is because of the approximate 12 hour time-lag of response of the atmosphere to the SST changes, and that during this 12 hour period the storm will move to an area with an undisturbed SST. Second, any changes that are made to the tropical cyclone due to an induced SST cooling will be most evident near the inner eye wall, but not in the outer storm strength. This would imply that the induced SST anomaly may not affect the track of the system.

The results presented here represent only a fraction of the type of studies that will be possible using a coupled mesoscale prediction system. First, we anticipate an expansion of the work presented here to include moving storms, as well as effects of radiation and landfall. Second, we are working toward expanding COAMPS to include topography in both the atmosphere and ocean, radiation parameterization and modifications to allow us to use COAMPS in real-data simulations. Third, we are currently validating COAMPS ability to simulate other features such as

rotating convective clouds, topographically induced flows, lake-effect snowstorms and the structure of the planetary boundary layer in coastal areas.

*Acknowledgements.* The author wishes to express his appreciation to Dr. Steve Burk, Dr. Simon Chang, Dr. James Doyle, Ms. Tracy Haack, Dr. John Hovermale, Dr. Hung-Chi Kuo and Dr. Tom Rosmond for their discussions, suggestions and reviews of the development of COAMPS and this paper. The author also acknowledges the computer support ably provided by Mr. Allan Caughey and the effort made by Mr. Steve Bishop in editing the text and mounting and labeling the figures. The support of the sponsor, Office of Naval Research, program element 0602435N, is gratefully acknowledged.

## References

- Anthes, R. A., and S. W. Chang, 1978: Response of the hurricane boundary layer to changes of the sea surface temperature in a numerical model. *J. Atmos. Sci.*, **35**, 1241-1255.
- Arakawa, A., and V. R. Lamb, 1974: *Computational design of the UCLA general circulation model*. Methods in Computational Physics, Vol. 17, Academic Press, 173-265.
- Black, M. L., and H. E. Willoughby, 1992: The concentric eyewall cycle of Hurricane Gilbert. *Mon. Wea. Rev.*, **120**, 947-957.
- Brink, K. H., 1989: Observations of the response of thermocline currents to a hurricane. *J. Phys. Oceanogr.*, **19**, 1017-1022.
- Brooks, D. A., 1983: The wake of Hurricane Allen in the western Gulf of Mexico. *J. Phys. Oceanogr.*, **13**, 117-129.
- Carpenter, K. M., 1979: An experimental forecast using a non-hydrostatic model. *Quart. J. R. Met. Soc.*, **105**, 629-655.
- Chang, S. W., 1985: Deep ocean response to hurricanes as revealed by an ocean model with free surface. Part I: Axisymmetric case. *J. Phys. Oceanogr.*, **15**, 1847-1858.

- Chang, S. W., and R. A. Anthes, 1979: The mutual response of the tropical cyclone and the ocean. *J. Phys. Oceanogr.*, **9**, 128-135.
- Chorin, A. J., 1967: A numerical method for solving incompressible viscous flow problems. *J. Comput. Phys.*, **2**, 12-16.
- Clancey, R. M., and K. D. Pollak, 1983: A real-time synoptic ocean thermal analysis/forecast system. *Prog. Oceanogr.*, **12**, 383-424.
- Clark, T. L., 1977: A small scale dynamic model using a terrain-following coordinate transformation. *J. Comp. Phys.*, **24**, 186-215.
- Clark, T. L., 1979: Numerical simulations with a three-dimensional cloud model: Lateral boundary condition experiments and multicellular severe storm simulations. *J. Atmos. Sci.*, **36**, 2191-2215.
- Deardorff, J. W., 1980: Stratocumulus-capped mixed layers derived from a three-dimensional model. *Bound.-Layer Meteor.*, **18**, 495-527.
- DeMaria, M. 1985: Tropical cyclone motion in a nondivergent barotropic model. *Mon. Wea. Rev.*, **113**, 1199-1210.
- Droegemeier, K. K., and R. B. Wilhelmson, 1987: Numerical simulation of thunderstorm outflow dynamics. Part I: Outflow sensitivity experiments and turbulence dynamics. *J. Atmos. Sci.*, **44**, 1180-1210.

- Durrán, D. R., and J. B. Klemp, 1983: A compressible model for the simulation of moist mountain waves. *Mon. Wea. Rev.*, **111**, 2341-2361.
- Fisher, E. L., 1958: Hurricane and the sea-surface temperature field. *J. Meteor.*, **15**, 328-333.
- Fortner, L. E., 1958: Typhoon Sarah, 1956. *Bull. Amer. Meteor. Soc.*, **39**, 633-639.
- Gill, A. E., 1982: *Atmosphere-ocean dynamics*. Academic Press, 662 pp.
- Hodur, R. M., 1987: Evaluation of a regional model with an update cycle. *Mon. Wea. Rev.*, **115**, 2707-2718.
- Hogan, T. F., and T. E. Rosmond, 1991: The description of navy operational global atmospheric prediction system's spectral forecast model. *Mon. Wea. Rev.*, **119**, 1786-1815.
- Holland, G. J., 1984: Tropical cyclone motion: A comparison of theory and observation. *J. Atmos. Sci.*, **41**, 68-75.
- Holliday, C. R., 1977: Double intensification of Typhoon Gloria, 1974. *Mon. Wea. Rev.*, **105**, 523-528.

- Hopkins, C., 1982: Ocean response to hurricane forcing. M. S. thesis, Naval Post-graduate School, 89 pp.
- Jordan, C. L., 1966: The thermal structure of the core of tropical cyclones. *Geophysics*, **6**, 281-297.
- , and F. J. Schatzle, 1961: The "double-eye" of Hurricane Donna. *Mon. Wea. Rev.*, **89**, 354-356.
- Klemp, J., and R. Wilhelmson, 1978: The simulation of three-dimensional convective storm dynamics. *J. Atmos. Sci.*, **35**, 1070-1096.
- Leiper, D. F., 1967: Observed ocean conditions and Hurricane Hilda, 1964. *J. Atmos. Sci.*, **24**, 182-196.
- Louis, J. F., M. Tiedtke and J. F. Geleyn, 1982: A short history of the operational PBL-parameterization at ECMWF. *Workshop on Planetary Boundary Parameterization*, ECMWF, Reading, 59-79. [Available from The European Centre for Medium-Range Weather Forecasts, Shinfield Park, Reading RG2 9Ax, U. K.]
- Mellor, G., and Yamada, 1974: A hierarchy of turbulence closure models for planetary boundary layers. *J. Atmos. Sci.*, **31**, 1791-1806.
- Miller, M. J., 1974: On the use of pressure as vertical co-ordinate in modelling convection. *Quart. J. R. Met. Soc.*, **100**, 155-162.

- \_\_\_\_\_, and R. P. Pearce, 1974: A three-dimensional primitive equation model of cumulonimbus convection. *Quart. J. R. Met. Soc.*, **100**, 133-154.
- \_\_\_\_\_, and A. J. Thorpe, 1981: Radiation conditions for the lateral boundaries of limited-area numerical models. *Quart. J. R. Met. Soc.*, **107**, 615-628.
- Ogura, Y., and J. Charney, 1962: A numerical model of thermal convection in the atmosphere. *Proc. of the International Symposium on N. W. P.*, Tokyo, Japan, Nov. 7-13 1960, pp. 431-451.
- \_\_\_\_\_, and N. W. Phillips, 1962: Scale analysis of deep and shallow convection in the atmosphere. *J. Atmos. Sci.*, **19**, 173-179.
- Orlanski, I., 1976: A simple boundary condition for unbounded hyperbolic flows. *J. Comput. Phys.*, **21**, 251-269.
- Price, J. F., 1981: Upper ocean response to a hurricane. *J. Phys. Oceanogr.*, **11**, 153-175.
- Pudov, V. D., A. A. Varfolomeev and K. N. Fedorov, 1978: Vertical structure of the wake of a typhoon in the upper ocean. *Okeanologiya*, **18**, 142-146.
- Robert, A. J., 1966: The investigation of a low order spectral form of the primitive meteorological equations. *J. Meteor. Soc. Japan*, **44**, 237-245.

- Rosenthal, S. L., 1977: Numerical simulation of a tropical cyclone development with latent heat release by the resolvable scales. I: Model description and preliminary results. *J. Atmos. Sci.*, **35**, 258-271.
- Rutledge, S. A., and P. V. Hobbs, 1983: The mesoscale and microscale structure of organization of clouds and precipitation in midlatitude cyclones. VIII: A model for the "seeder-feeder" process in warm-frontal rainbands. *J. Atmos. Sci.*, **40**, 1185-1206.
- Sanford, T. B., P. G. Black, J. Haustein, J. W. Fenney, G. Z. Forristall and J. F. Price, 1987: Ocean response to hurricanes. Part 1: Observations. *J. Phys. Oceanogr.*, **17**, 2065-2083., 1987:
- Schlesinger, R. E., 1975: A three-dimensional numerical model of an isolated deep convective cloud: preliminary results. *J. Atmos. Sci.*, **32**, 934-957.
- Schumann U., 1987: Influence of mesoscale orography on idealized cold fronts. *J. Atmos. Sci.*, **44**, 3423-3441.
- Shapiro, L. J., and H. E. Willoughby, 1982: The response of balanced hurricanes to local sources of heat and momentum. *J. Atmos. Sci.*, **39**, 378-394.
- Shay, L. K., P. G. Black, J. D. Hawkins, R. L. Elsberry, and A. J. Mariano, 1991: Sea surface temperature response to Hurricane Gilbert. *Preprint, 19th Conf. on Hurricanes and Tropical Meteorology*, Miami, FL, Amer. Meteor. Soc., 574-578.

- \_\_\_\_\_, and R. L. Elsberry, 1987: Near-inertial ocean current response to Hurricane Frederic. *J. Phys. Oceanogr.*, **17**, 1249-1269.
- Skamarock, W. C., and J. B. Klemp, 1992: The stability of time-split numerical methods for the hydrostatic and the nonhydrostatic elastic equations. *Mon. Wea. Rev.*, **120**, 2109-2127.
- Smagorinsky, J., 1963: General circulation experiments with the primitive equations: 1. The basic experiment. *Mon. Wea. Rev.*, **91**, 99-164.
- Tapp, M. C., and P. W. White, 1976: A nonhydrostatic mesoscale model. *Quart. J. R. Met. Soc.*, **102**, 277-296.
- Teague, W. J., M. J. Carron, and P. J. Hogan, 1990: A comparison between the generalized environmental model and Levitus climatologies. *J. Geophys. Res.*, **95**, 7167-7183.
- Tripoli, G. J., 1992a: A nonhydrostatic mesoscale model designed to simulate scale interaction. *Mon. Wea. Rev.*, **120**, 1342-1359.
- \_\_\_\_\_, 1992b: An explicit three-dimensional nonhydrostatic numerical simulation of a tropical cyclone. (Submitted for publication to: *Mon. Wea. Rev.*).
- \_\_\_\_\_, and W. R. Cotton, 1982: The Colorado State University three-dimensional cloud/mesoscale model - 1982. Part I: General theoretical framework and sensitivity experiments. *J. Rech. Atmos.*, **16**, 185-220.

- Willoughby, H. E., J. Clos, and M. Shoreibah, 1982: Concentric eyewalls, secondary wind maxima, and the evolution of the hurricane vortex. *J. Atmos. Sci.*, **39**, 395-411.
- , J. M. Masters, and C. W. Landsea, 1989: A record minimum sea level pressure observed in Hurricane Gilbert. *Mon. Wea. Rev.*, **117**, 2824-2828.
- Wyngaard J. C., 1982: *Atmospheric Turbulence and Air Pollution Modelling; A Course held in The Hague, 21-25 September 1986*, D. Reidel Publishing Company, 358 pp.
- Xue, M., and A. J. Thorpe, 1991: A mesoscale model using the nonhydrostatic pressure-based sigma-coordinate equations: Model experiments with dry mountain flows. *Mon. Wea. Rev.*, **119**, 1168-1185.

## DISTRIBUTION LIST

OFFICE OF NAVAL RESEARCH  
ATTN A WEINSTEIN CODE 1122  
OCEAN SCIENCES DIVISION  
ARLINGTON VA 22217-5660

NOAA-HRD  
ATTN PETER BLACK  
4301 RICKENBACKER CAUSEWAY  
MIAMI FL 33149

DEFENSE TECH INFO CENTER  
CODE DTIC-FD DOC PROC DIV  
BLDG 5 CAMERON STATION  
ALEXANDRIA VA 22304-6145

2

NAVRSCHLAB  
ATTN DR RAS MADALA CODE 7225  
WASHINGTON DC 20375-5320

COMMANDING OFFICER  
ATTN DR E HARTWIG  
NAVRSCHLAB  
WASHINGTON DC 20375-5320

NAVRSCHLAB  
ATTN SIMON CHANG CODE 7225  
WASHINGTON DC 20375-5320

COMMANDING OFFICER  
ATTN CODE 5227 DOCS SEC  
NAVRSCHLAB  
WASHINGTON DC 20375-5320

12

NAVRSCHLAB  
ATTN DR TAK FUNG CODE 7225  
WASHINGTON DC 20375-5320

COMMANDING OFFICER  
ATTN CODE 1221 CLASSIF MGT  
NAVRSCHLAB  
WASHINGTON DC 20375-5320

NAVRSCHLAB  
ATTN DR PAT GALLACHER  
CODE 7331  
JCSSC MS 39529-5004

NAVRSCHLAB  
ATTN LIBRARY  
JCSSC MS 39529-5004

LIANG XU  
NCSU DEPT OF MEAS  
BOX 2808  
RALEIGH NC 27695

NAVRSCHLAB  
ATTN DR MOSELY CODE 7300  
JCSSC MS 39529-5004

OL-AA PL GPAP  
ATTN DON CHISHOLM  
29 RANDOLPH RD  
HANSCOM AFB MA 01731-3010

COMMANDING OFFICER  
FLENUMOCEANCEN  
7 GRACE HOPPER AVE  
MONTEREY CA 93943-5501

OFFICE OF NAVAL RESEARCH  
ATTN R H FEDEN CODE 124A  
800 N QUINCY ST BCT #1  
ARLINGTON VA 22217-5000

NAVPGSCOL  
ATTN CODE MR  
MONTEREY CA 93943-5000

3

NAVRSCHLAB  
ATTN CDR P RANELLI CODE 7001  
4555 OVERLOOK AVE SW  
WASHINGTON DC 20375-5320

COMSPAWARSYSCOM  
ATTN PMW 165  
WASHINGTON DC 20363-5100

OFFICE OF NAVAL RESEARCH  
ATTN DR S SANGATHE CODE 453  
800 N QUINCY ST ROOM 428  
ARLINGTON VA 22217-5000

RSMAS/UNIV OF MIAMI  
ATTN NICK SHAY MPO  
4600 RICKENBACKER CAUSEWAY  
MIAMI FL 33149

BATTLEFIELD ENVIRONMENTAL  
DIRECTORATE  
ATTN JIM HARRIS AMSRL BE W  
WHITE SANDS MR NM 88002-5501